Journal
of Road Engineering Association
of Asia and Australasia

REAAA

JREAAA 1/2025

Journal of Road Engineering Association of Asia and Australasia

Journal homepage: www.reaaa.net
JREEA – 1/2025: i

Message from the Chief Editor

Welcome to the inaugural issue of the Journal of Road Engineering Association of Asia and Australasia (JREAAA). This edition marks a key milestone as REAAA launches a platform to share the latest research and insights in road engineering across our region.

JREAAA is dedicated to advancing safer, more efficient, and sustainable transport infrastructure by fostering collaboration and promoting best practices among professionals in Asia and Australasia.

We are proud to present eight papers from REAAA members in this issue, reflecting the breadth of expertise in our community. Thank you to our authors, reviewers, and editorial team for their valuable contributions.

Your support and feedback are essential to our success. On behalf of the editorial team, thank you once again.

Sincerely,
Chief Editor, JREAAA

About the Journal

The Journal of Road Engineering Association of Asia and Australasia (JREAAA) is a peer-reviewed e-journal published by the Road Engineering Association of Asia and Australasia (REAAA). JREAAA provides an open academic forum for the publication and exchange of cutting-edge research findings in road engineering, serving academicians, researchers, practitioners, and policymakers across the Asia-Pacific and Australasia regions.

The journal's primary objective is to promote and advance the science and practice of road engineering and its related professions. By publishing high-quality research articles, case studies, and technical reviews, JREAAA supports continuous learning, professional development, and the elevation of road engineering standards. The journal is also dedicated to encouraging the sharing of innovative ideas and best practices, ultimately contributing to the development of safer, more efficient, and sustainable road infrastructure throughout the region.

Journal of Road Engineering Association of Asia and Australasia
Journal homepage: www.reaaa.net
JREAA – 1(1) 2025:1-5

OPEN ACCESS

Field assessment of rutting performance in asphalt modified with natural rubber and synthetic polymer

Zainiah Mohd Zin[1,]* & Khairi Hafiz Yahya[1]
*Corresponding author: zainiahmz@jkr.gov.my

[1]*Centre of Excellence for Engineering and Technology, Public Works Department Malaysia, 78000, Alor Gajah, Melaka, Malaysia*

ABSTRACT

At high temperatures, asphalt pavement structures are more susceptible to permanent deformation. However, this susceptibility can be mitigated by incorporating natural rubber and synthetic polymers into modified asphalt binder. This study aimed to assess the rutting resistance of asphalt mixtures by evaluating physical tests, mechanical performance, and field rutting measurements conducted after two years of pavement construction. The physical tests were carried out using both penetration and softening point methods. The mechanical performance of the modified asphalt mixture was assessed through volumetric testing and the Marshall stability test. Field rutting measurements were evaluated using a straight edge. Cup lump rubber (CLR) and natural rubber latex (NRL) were used as natural rubber, while polyolefin and aramid fibre (PAF) and low-density polyethene (LDPE) were synthetic polymers. In this study, 5% CLR and 3% NRL, each based on the weight of the binder, were blended with the 60/70 asphalt binder.

Meanwhile, 0.05% PAF and 6% LDPE, based on the weight of the asphalt mixture, were added to the aggregates through dry mixing before being combined with the asphalt binder. The investigations revealed that the physical tests indicated that natural rubber improved the stiffness of the asphalt binder. The modified asphalt mixture demonstrated better Marshall stability than the control 60/70 asphalt binder. The field rutting measurements determined that the CLR asphalt mixture exhibited better rutting resistance at high temperatures in a tropical climate.

ARTICLE INFO

Article History:
Received 16 Aug 2024
Received in revised form
16 Dec 2024
Accepted
01 Apr 2025
Available online
01 May 2025

Keywords:
Cup lump rubber modified asphalt
Natural rubber latex modified asphalt
Polyolefin and aramid fiber-modified asphalt
Low density polyethylene modified asphalt
Rutting
Field assessment

1. Introduction

Countries worldwide have faced challenges maintaining existing road networks due to increasing traffic volumes, axle loads, and tyre pressures. In Malaysia, the majority of the major road network was paved with hot mix asphalt (HMA). The nature of HMA rendered it susceptible to permanent deformation from temperature and loading effects. The issue of ageing in asphalt mixtures has been debated among researchers for many years, as ageing and moisture reduce the service life of asphalt mixtures, leading to failures such as alligator cracking, ravelling, potholes, and rutting (Kakar et al., 2015). Over the past few decades, the asphalt industry has shifted its focus to exploring the potential of bio-polymers and synthetic polymers to enhance the rutting resistance of asphalt binders (Behnood & Modiri Gharehveran, 2019; Poovaneshvaran et al., 2023). The choice of polymer type depended on expected performance, cost, climatic conditions, and availability.

The significant decline in the global market price of natural rubber (NR) over the last decade led researchers to expand its use as an asphalt pavement modifier (Ansari et al., 2021). As an elastomeric material, natural rubber (NR) enhances the stiffness of asphalt binder, improving its resistance to permanent deformation. Furthermore, natural rubber, unlike other polymeric materials made from crude oil, is renewable and has a lower embodied energy (Sani et al., 2023). Rutting, a plastic deformation in pavement layers due to accumulating vertical strains from repetitive traffic loads, was a particular focus of this study.

The applications of natural rubber latex (NRL) as a bio-polymer were also investigated by researchers (Abdulrahman et al., 2021) to improve the rheological properties of asphalt binders under various temperatures and loading conditions. Wen et al. (2017) and Ziari et al. (2018) found that asphalt binders modified with NRL at different percentages exhibited improved rutting resistance compared to those made with base asphalt binder. Cup lump rubber (CLR) was seen as a long-term solution for increasing domestic consumption in asphalt applications. CLR improved stiffness, elasticity, and viscosity, enhancing binder properties and resulting in better rutting resistance at high temperatures (Ghafar et al., 2024; Zin et al., 2023).

Synthetic polymers derived from petroleum can be categorized into thermoplastics, elastomers, and synthetic fibres. Fibers, used as reinforcing materials, provided additional tensile strength to the composite, increasing the amount of strain energy absorbed during fatigue and fracture. Some fibres, having high tensile strength relative to asphalt mixtures, were found to improve bituminous mixes' cohesive and tensile strength (Alfalah et al., 2020). Polyolefin and aramid fibre (PAF) were studied for their effectiveness in asphalt mixes, with most studies reporting benefits in rutting performance (Khan et al., 2024). However, the impact of PAF at the manufacturer-recommended dosage had not been fully explored, prompting this study to investigate its performance in rutting resistance through field assessment. Low-density polyethylene (LDPE), a type of synthetic polymer, has been increasingly investigated as an asphalt modifier due to its environmental and economic advantages (Venkatesan et al., 2022).

This study examined the performance of asphalt mixtures modified with natural rubber and waste plastics. An analysis was conducted to evaluate these mixtures' performance and engineering properties in terms of rutting resistance.

2. Materials

2.1. Asphalt Binder

Figure 1 was used to illustrate the raw materials employed as additives in asphalt: CLR, NRL, PAF, and LDPE. In this study, 5% CLR and 3% NRL, each based on the weight of the binder, were blended with the 60/70 asphalt binder. The natural rubber-modified asphalt binder was then combined with the aggregates. The properties of CLR and NRL are summarized in Table 1 and Table 2. Meanwhile, 0.05% PAF and 6% LDPE, based on the weight of the asphalt mixture, were mixed with the aggregates through dry mixing before being combined with the 60/70 asphalt binder. Table 3 and Table 4 summarise the PAF and LDPE properties. The recommended dosage of 0.05% PAF was investigated by several studies (Alfalah et al., 2020; Khan et al., 2024; Muftah et al., 2017). Researchers quantified the benefit that the addition of 6% LDFE extended the pavement service life (Hassani et al., 2005; Ma et al., 2021; Mashaan et al., 2021).

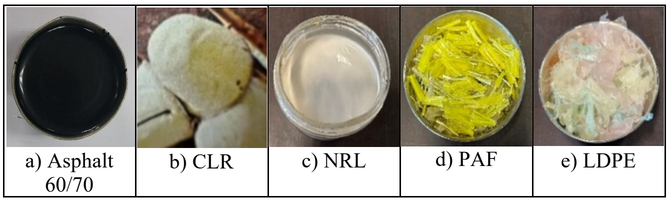

Figure 1: Raw materials.

Table 1: Properties of CLR.

Parameters	Description
Form	Solid
Colour	Milky white
pH	5.50
Specific gravity	0.93
Length, (mm)	<20

Table 2: Properties of NRL.

Parameters	Description
Form	Liquid
Colour	Milky white
pH	5.45
Total solids content	65.28
Viscosity @ 26ºC	195

Table 3: Properties of PAF.

Parameters	Description
Form	Monofilament
Colour	Yellow
Length, (mm)	19.00
Specific gravity polyolefin	0.19
Specific gravity aramid	1.44

Table 4: Properties of LDPE.

Parameters	Description
Form	Solid
Colour	Multicolour
Specific gravity	0.94
Solubility	Insoluble in water
Length, (mm)	2.36 – 4.60

2.2. Aggregates

Crushed granite aggregates of different sizes were employed in this study to prepare the asphalt mixture samples. The dense-aggregate gradation used followed the specifications outlined by the Malaysian Public Works Department (PWD). Table 5 illustrates the aggregate gradation for the 60/70 asphalt mixture and the polymer-modified asphalt mixture.

Table 5: Aggregates gradation.

B.S Sieve Size	Passing 60/70 (%)	Passing CLR (%)	Passing NRL (%)	Passing PAF (%)	Passing LDPE (%)
20 mm	100	100	100	100	100
14 mm	96.4	97	98.7	96.9	97
10 mm	83.1	81	84	82.9	81
5 mm	58.6	55.1	59.2	57.9	55.1
3.35 mm	46.2	45.2	45.4	45.8	45.2
1.18 mm	25.9	24.4	24.4	25.1	24.4
0.425 mm	14.7	13.8	13.9	14.5	13.8
0.15 mm	8.1	7.5	7.2	7.6	7.5
0.075 mm	4.1	4.6	4.8	3.7	4.6
Pan	-	-	-	-	-

3. Methods

3.1. Penetration Test

The penetration test was conducted to assess the penetration grade and determine the consistency of the asphalt binder. Higher penetration values indicated a softer binder. The penetration grade was measured using a penetrometer, where a standard needle was applied to the sample under specific conditions. The temperature, load, and time test conditions were 25 °C, 100 g, and 5 seconds, respectively. The procedure followed for the test was based on ASTM D5 standards.

3.2. Softening Point Test

The softening point test was carried out to measure the softening point of the asphalt binder using a ring and ball apparatus submerged in distilled water. As a viscoelastic material, the asphalt binder does not have sharply defined melting points; instead, it gradually becomes softer and less viscous as the temperature increases. Therefore, the softening points were determined using an arbitrary yet precisely defined method. Two horizontal disks of asphalt binder, cast in shouldered brass rings, were heated at a controlled rate of 5 °C per minute in a liquid bath, each supporting a steel ball. The softening point was reported as the average temperature at which both disks softened sufficiently to allow each ball, enveloped in asphalt binder, to fall a distance of 25 mm. The test was carried out according to ASTM D36.

3.3. Volumetric Test

The amount of voids in an asphalt mixture is likely the most critical factor influencing the performance of asphalt pavement throughout its lifespan. The contents of asphalt binder and aggregates primarily control the voids in an asphalt mixture. The volumetric tests performed in this study include density measurement. The compacted specimen was weighted in air and water, and the bulk density was subsequently determined using the appropriate equation. The calculation of volumetric properties began with determining the maximum theoretical density. The difference between this theoretical density and the actual bulk density was then expressed as a percentage of the total volume to determine the percentage of air voids in the mixture (VTM). The volumetric variables were specified based on the guidelines provided by the Public Works Department of Malaysia, as outlined in JKR/SPJ/2008-S4.

3.4. Marshall Stability Test

The Marshall stability test was performed on compacted asphalt mixture specimens following ASTM D 1559. The Marshall test was conducted using cylindrical compacted specimens with a diameter of 100 mm and an approximate height of 63.5 mm. A water bath was set to a temperature of 60°C, and all specimens were immersed in it for 30 to 40 minutes. After the specimen had been conditioned on the Marshall stability machine, a load was applied at a constant rate of 50 mm/min until failure occurred. The flow and stability were monitored during the loading process. When the stability gauge reading reached its peak and started to decrease, the Marshall stability value was recorded as the deformation at the point of failure. The test was conducted following ASTM D1559-76 standards.

3.5. Field Rutting Measurement

Field measurements were conducted to evaluate the effectiveness of a modified asphalt mixture compared to conventional 60/70 asphalt. The study was carried out on various sections of roads in Peninsular Malaysia, specifically: modified asphalt with CLR on Federal Route 2, from section 199.50 to 200.50; NRL modified asphalt on Federal Route 5, from section 468 to 471; PAF modified asphalt on Federal Route FT29, from section 46 to 48; and LDPE modified asphalt on State Route B88, from section 0.1 to 0.5. These pavement cross-sections are shown in Figure 2. The pavement structure has been designed at 80 kN, equivalent standard axle load (ESAL), based on the specifications outlined by the Malaysian Public Works Department (PWD), according to ATJ5/85.

The field performance was monitored within a specific 200-meter segment. This segment was chosen to exclude areas such as intersections, culverts, bridges, and curves to ensure the evaluation process was not affected by potential disruptions. Permanent markings were placed on the study segment to ensure each monitoring session was conducted within the same area. Monitoring concentrated on assessing rutting on the road surface to compare the performance of the modified asphalt mixture pavement with the 60/70 asphalt mixture as the control section. Surface assessment for rutting consists of measuring the depth of transverse unevenness along the vehicle wheel paths. Using a straight edge, surface unevenness can be evaluated by measuring rutting depth, which reflects deformation in the asphalt pavement. The test was conducted according to ASTM E1703.

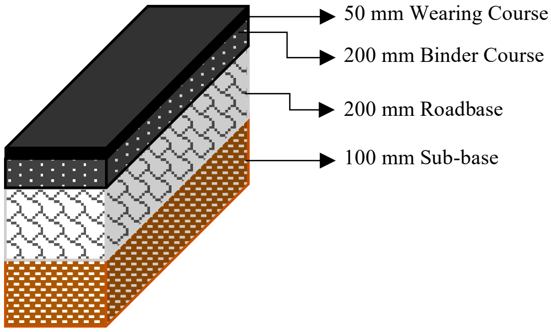

Figure 2: Cross-sections of pavement structures.

4. Result and Discussion

4.1. Physical Properties of the Asphalt Binder

The asphalt binder is a viscoelastic material that can gradually become softer and less viscous at elevated temperatures. Thus, it is crucial to use a modified binder, which can withstand higher temperatures than an unmodified binder. Pavement temperatures in Malaysia can reach as high as 60°C during hot weather (Poovaneshvaran et al., 2020). Figure 3 illustrates the relationship between the physical properties of the asphalt binder. Physical parameters were assessed through penetration and softening point tests. Figure 3 shows that the penetration value of the CLR and NRL-modified asphalt binders demonstrated better performance than the 60/70 asphalt binders. Adding CLR and NRL to the 60/70 asphalt binder increases stiffness due to the hardening effect.

Figure 3 illustrates that CLR and NRL-modified asphalt binders exhibit higher softening point values. Employing CLR and NRL-modified asphalt binders can help prevent performance issues in pavements during temperature increases, as these binders are less affected by temperature changes, thereby improving pavement performance. The rubber content in the asphalt binder was linked to a higher asphaltene ratio, which was believed to increase the binder's stiffness and lessen its sensitivity to temperature fluctuations. It can be concluded that NR-modified asphalt binders are appropriate for road construction in tropical climates. All the asphalt binders comply with the standards necessary for conventional paving applications.

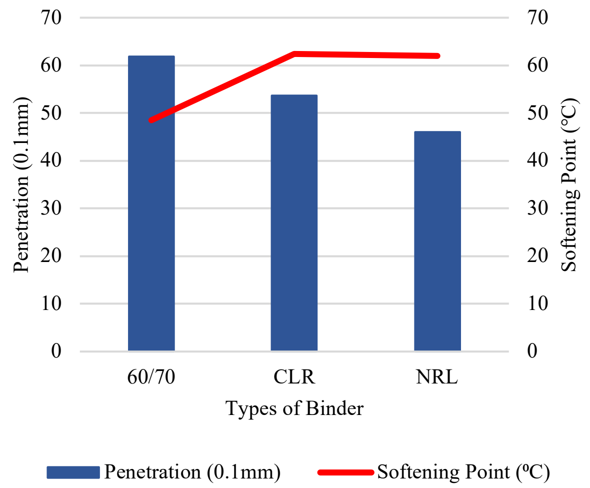

Figure 3: Laboratory penetration and softening point result.

4.2. Volumetric Properties of Polymer Modified Asphalt

Density is an essential parameter for ensuring quality control during the construction of asphalt mixtures. Figure 4 displays the density of the compacted mixtures using asphalt binders 60/70, CLR, NRL, PAF, and LDPE. The results indicate that the CLR asphalt mixture exhibits the highest density compared to the synthetic asphalt. This was caused by the density and concentration of CLR in the asphalt binder, which was used to lubricate the aggregate particles. Density must be accurately controlled to ensure that voids are within the acceptable range of specifications.

Voids in the mixture (VTM) are essential parameters in hot mix asphalt (HMA) design. The VTM value is crucial for durability because higher voids can lead to increased air and moisture exposure, which impacts the bond between aggregate and binder. Figure 4 shows how VTM varies among different asphalt mixtures. The results in Figure 4 indicate that VTM slightly increases in bio-polymer-modified asphalt compared to synthetic polymer-modified asphalt. This illustrates that synthetic polymer-modified asphalt produces a more homogeneous asphalt aggregate structure with fewer, smaller, and more uniformly distributed voids, resulting in reduced stress concentration at critical solid-air interfaces.

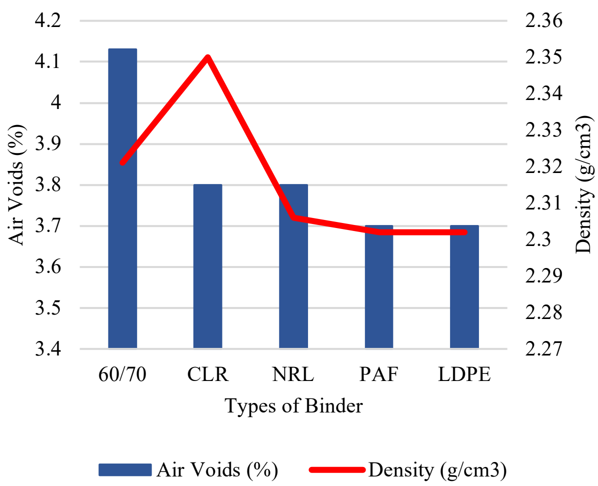

Figure 4: Air voids and density asphalt mixtures.

Figure 5: Stability and optimum binder content of asphalt mixtures.

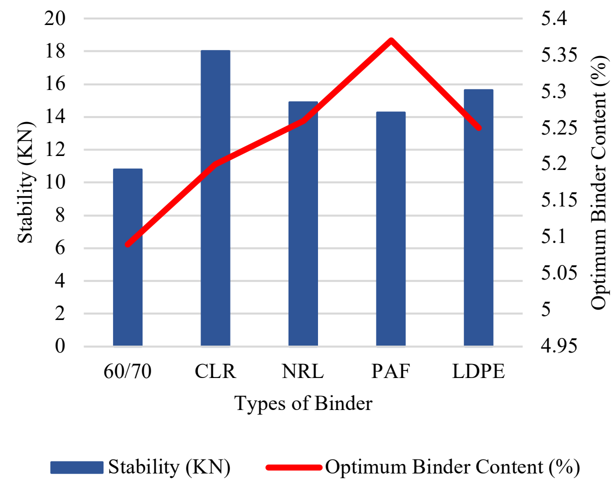

4.3. Impact of Polymer on Marshall Stability

The primary purpose of the stability test is to determine the strength of the bituminous mixture. Figure 5 illustrates the stability values of asphalt mixtures containing 60/70, CLR, NRL, PAF, and LDPE about the optimum binder content (OBC). The stability results indicate that polymer-modified asphalt exhibits higher values compared to the 60/70 asphalt mixture. However, the stability value of the CLR-modified asphalt mixture is the highest despite having the lowest OBC among polymer-modified asphalt. This indicates that incorporating synthetic and natural rubber processes resulted in a more homogeneous and interconnected binder microstructure. This deduced that absorption and evaporation effects due to the incorporation of polymers make the binders less sensitive to shear stress.

Figure 5 shows that the optimum binder content in the modified asphalt mixtures was higher than in the 60/70 asphalt mixture. The PAF-modified asphalt mixture had the highest result among the modified asphalts, at 5.37%. This is due to the porous texture that forms cavities in polymer-modified asphalt, which increases the binder content needed (Azahar et al., 2021; Shaffie et al., 2016).

4.4. Effects of Aging on Rutting Resistance

In the field, pavement layers are exposed to the atmosphere, allowing the binder to come into contact with oxygen. The reaction of asphalt binder with oxygen alters its composition, making the material more susceptible to wear and moisture damage. The compositional changes in the asphalt binder lead to increased hardening, which in turn results in greater stiffness. Figure 6 shows the field rutting results collected 24 months after the completion of road construction. It demonstrates the impact of ageing on the rutting resistance of conventional asphalt 60/70 and natural rubber and synthetically modified asphalt mixtures. CLR-modified asphalt shows the highest rutting resistance compared to all other asphalt binders. In contrast, the LDPE asphalt mixture exhibits the weakest rutting performance in the field assessment on pavement structures designed for 80 kN.

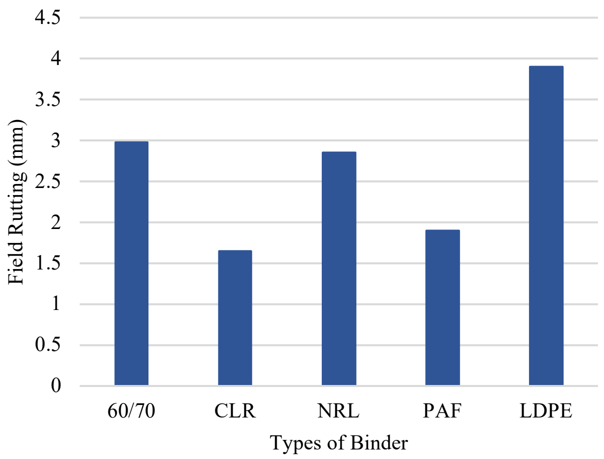

Figure 6: Field rutting result.

5. Conclusions

The effects of natural rubber and synthetic polymer on asphalt mixtures were assessed through the physical properties of the asphalt binder, volumetric properties of the asphalt mixture, Marshall stability, and the impact of ageing on rutting performance evaluated in the field 24 months after construction. The analysis of the results leads to the following conclusions:

- The results show that incorporating CLR and NRL into the modified binders raised the softening point. Since asphalt binder is a viscoelastic material, assessing its softening point is crucial for choosing the appropriate modified binder for local climate and weather conditions. The CLR asphalt binder exhibited the highest softening point at 62.4°C, while the NRL-modified asphalt binder had a softening point of 62°C.
- The penetration test results show that the NRL-modified asphalt binder is harder than others.
- The volumetric properties of asphalt mixtures demonstrate that those incorporating natural rubber and synthetic polymers satisfy the standards for conventional paving applications.
- The Marshall stability test confirms that all modified asphalt mixtures demonstrate increased resistance to shear stress and permanent deformation.
- Field rutting results obtained 24 months after road construction showed that CLR-modified asphalt mixtures had the lowest level of rutting. These mixtures performed better than all other asphalt mixtures. This suggests that CLR-modified asphalt can be used as a modifier in asphalt. It would provide superior resistance to both environmental factors and traffic loading.

6. References

Abdulrahman, S., Hainin, M. R., Idham Mohd Satar, M. K., Hassan, N. A., & Usman, A. (2021). Mechanical performance and global warming potential of unaged warm cup lump modified asphalt. *Journal of Cleaner Production*, *297*, 126653.

Alfalah, A., Offenbacker, D., Ali, A., Decarlo, C., Lein, W., Mehta, Y., & Elshaer, M. (2020). Assessment of the Impact of Fiber Types on the Performance of Fiber-Reinforced Hot Mix Asphalt. *Transportation Research Record*, *2674*(4), 337–347.

Ansari, A. H., Jakarni, F. M., Muniandy, R., Hassim, S., & Elahi, Z. (2021). Natural rubber as a renewable and sustainable bio-modifier for pavement applications: A review. *Journal of Cleaner Production*, *289*, 125727.

Azahar, N. M., Hassan, N. A., Jaya, R. P., Hainin, M. R., Yusoff, N. I. M., Kamaruddin, N. H. M., Yunus, N. Z. M., Hassan, S. A., & Yaacob, H. (2021). Properties of cup lump rubber modified asphalt binder. *Road Materials and Pavement Design*, *22*(6), 1329–1349.

Behnood, A., & Modiri Gharehveran, M. (2019). Morphology, rheology, and physical properties of polymer-modified asphalt binders. *European Polymer Journal*, *112*, 766–791.

Ghafar, S. A., Warid, M. N. M., Hassan, N. A., Jattak, Z. A., & Radwan, A. A. M. (2024). Mechanical performance of cold mix asphalt containing cup lump rubber as a sustainable bio-modifier. *Journal of Traffic and Transportation Engineering*, *11*(3), 424–440.

Hassani, A., Ganjidoust, H., & Maghanaki, A. A. (2005). Use of plastic waste (polyethylene terephthalate) in asphalt concrete mixture as aggregate replacement. *Waste Management & Research: The Journal for a Sustainable Circular Economy*, *23*(4), 322–327.

Kakar, M. R., Hamzah, M. O., & Valentin, J. (2015). A review on moisture damages of hot and warm mix asphalt and related investigations. *Journal of Cleaner Production, 99*, 39–58.

Khan, A. R., Ali, A., Mehta, Y., & Lein, W. (2024). Laboratory performance characterization of polyolefin/ aramid fibers and synthetic aramid fibers reinforced asphalt mixtures. *Construction and Building Materials*, *419*, 135576.

Ma, Y., Zhou, H., Jiang, X., Polaczyk, P., Xiao, R., Zhang, M., & Huang, B. (2021). The utilization of waste plastics in asphalt pavements: A review. *Cleaner Materials*, *2*, 100031.

Mashaan, N., Chegenizadeh, A., & Nikraz, H. (2021). Laboratory Properties of Waste PET Plastic-Modified Asphalt Mixes. *Recycling*, *6*(3), 49.

Muftah, A., Bahadori, A., Bayomy, F., & Kassem, E. (2017). Fiber-Reinforced Hot-Mix Asphalt: Idaho Case Study. *Transportation Research Record: Journal of the Transportation Research Board*, *2633*(1), 98–107.

Poovaneshvaran, S., Mohd Hasan, M. R., Jamshidi, A., Mohd Ghazali, M. F. H., Yang, X., & Putra Jaya, R. (2023). The Characterisation of Fracture Resistance of Asphalt Mixtures Containing Rubber Modifiers and a Wax-Based Additive. *Advances in Materials Science and Engineering*, *2023,* 3517521.

Poovaneshvaran, S., Mohd Hasan, M. R., & Putra Jaya, R. (2020). Impacts of recycled crumb rubber powder and natural rubber latex on the modified asphalt rheological behaviour, bonding, and resistance to shear. *Construction and Building Materials*, *234,* 117357.

Sani, A., Mohd Hasan, M. R., Shariff, K. A., Mukhtar, N., Akhtar, M. N., Uwanuakwa, I. D., Dai, Q., & Wong, T. L. X. (2023). Analytical study of silane-based and wax-based additives on the interfacial bonding characteristics between natural rubber modified binder and different aggregate types. *Journal of Road Engineering*, *3*(2),171–185.

Shaffie, E., Ahmad, J., Arshad, A. K., Kamarun, D., & Awang, H. (2016). Investigation on rutting performance of nanopolyacrylate and natural rubber latex polymer modified asphalt binder mixes. *Jurnal Teknologi*, *78*,7-3.

Venkatesan, R., Santhamoorthy, M., Alagumalai, K., Haldhar, R., Raorane, C. J., Raj, V., & Kim, S.-C. (2022). Novel Approach in Biodegradation of Synthetic Thermoplastic Polymers: An Overview. *Polymers*, *14*(20), 4271.

Wen, Y., Wang, Y., Zhao, K., & Sumalee, A. (2017). The use of natural rubber latex as a renewable and sustainable modifier of asphalt binder. *International Journal of Pavement Engineering*, *18*(6), 547–559.

Ziari, H., Naghavi, M., & Imaninasab, R. (2018). Performance evaluation of rubberized asphalt mixes containing WMA additives. *International Journal of Pavement Engineering*, *19*(7), 623–629.

Zin, Z. M., Hasan, M. R. M., Rashid, A. A., Ahmad, M. M., & Wong, T. L. X. (2024). The effect of wax-based surfactant on the physical properties of cup lump rubber modified asphalt binder. *In AIP Conference Proceedings, 2750* (1), 070020.

Journal of Road Engineering Association of Asia and Australasia

Journal homepage: www.reaaa.net
JREAA – 1(1) 2025: 6-13

OPEN ACCESS

Evaluation of Warm Mix Asphalt (WMA) Materials and Trial Paving Planning

Jyh-Dong Lin[1], Shih-Huang Chen[2], Li-Ling Huang[3,*], Meng-Hsin Kuo[4], Mao-Yuan Huang[5]& Chun-Hung Kuo[6]
*Corresponding author: irenahf@gmail.com

[1,2,3,4,5,6] *Department of Civil Engineering, National Central University, No. 300, Zhongda Road, Zhongli District, Taoyuan City, Taiwan.*

ABSTRACT

With the intensification of global climate change, integrating carbon reduction concepts into pavement maintenance has become crucial for achieving sustainable development and the 2050 net-zero emission target. Warm Mix Asphalt (WMA) technology has been widely adopted for its energy-saving and carbon reduction benefits, offering significant potential for improving durability performance in pavement maintenance. This study introduces WMA into Taiwan's provincial highway maintenance, aiming to reduce energy consumption and greenhouse gas emissions while achieving energy saving and carbon reduction goals. Laboratory experiments established optimal parameters, including an asphalt content of 4.4%, foaming water content of 1.0%–2.3%, mixing temperatures of 125°C–140°C, and compaction temperatures of 120°C–130°C, confirming WMA meets construction specifications. Subsequent plant trials and field applications on Provincial Highway No. 2 will assess durability performance using tests such as TSR, Hamburg wheel track, IRI, crack rate, and rut depth evaluations. Energy consumption analyses will also quantify WMA's energy-saving and carbon-reduction effects. This first application of WMA on a provincial highway in Taiwan demonstrates its potential to enhance pavement durability and sustainability, providing a practical approach to achieving net-zero emissions.

ARTICLE INFO

Article History:
Received 20 Sep 2024
Received in revised form
13 Dec 2024
Accepted
01 Apr 2025
Available online
01 May 2025

Keywords:
Keyword Warm Mix Asphalt (WMA)
Keyword Sustainable Development
Keyword Energy Saving
Keyword Carbon Reduction
Keyword Durability Performance

1. Introduction

1.1. Research Background

With the intensification of global warming, the greenhouse effect has exacerbated temperature increases more significantly than in any previous period, leading to increasingly severe impacts on the earth's ecology due to climate change. Countries actively promote various carbon reduction measures to mitigate global warming and prevent temperatures from exceeding critical limits that could trigger extreme weather and climate conditions. These measures aim to reduce greenhouse gas emissions to achieve the goal of net-zero emissions by 2050.

The key to greenhouse gas emissions lies in industrial activities. Economic development has spurred frequent operations in industrial processes, transportation, and construction, leading to the massive release of greenhouse gases such as carbon dioxide and methane into the atmosphere, indirectly contributing to temperature increases.

Pavement maintenance is a continuous process, making integrating carbon reduction concepts crucial. Asphalt concrete is the primary material used in road paving. In recent years, warm mix asphalt (WMA) technology has been widely adopted internationally. Compared to traditional hot mix asphalt (HMA), WMA exhibits similar strength, durability, and performance characteristics. WMA production temperatures can be reduced by 20–40°C, depending on the specific technology used, lowering energy consumption and effectively reducing greenhouse gas emissions. This contributes to the benefits of net-zero emissions, reduces negative environmental impacts, and enhances the sustainability of road construction.【1】

However, there has been no research in Taiwan on applying WMA on provincial highways. This study aims to explore the material performance of WMA and plan-related trial paving operations and follow-up testing, hoping to provide valuable references for future road construction in Taiwan.

2. Literature Review

2.1. Warm Mix Asphalt Material Characteristics

WMA technology is mainly divided into three types: chemical additives, organic additives, and foaming technology【2】【3】.

2.1.1. Chemical Additives

Chemical additive technology involves adding specific chemicals to asphalt concrete to reduce viscosity, enabling good workability at lower temperatures. This technology typically reduces the construction temperature by approximately 20-30°C, reducing energy consumption and greenhouse gas emissions. Chemical additives are suitable for various asphalt concrete mix designs and have been shown in past research to achieve material performance comparable to HMA, with the added benefit of reducing carbon emissions.

2.1.2. Organic Additives

Organic additive technology involves adding organic materials such as Sasobit and Evotherm to reduce the viscosity and working temperature of asphalt, while also improving the workability and durability of the asphalt mixture. Previous studies have shown that organic additive technology can effectively enhance the low-temperature crack resistance and high-temperature stability of asphalt concrete while reducing construction temperatures without compromising material performance.

2.1.3. Foaming Technology

Foaming technology uses water or water-based solutions at high temperatures to mix with asphalt, forming instantaneously expanded foam that reduces the viscosity of the asphalt, allowing for good flowability and workability at lower temperatures. This technology is simple to implement and easy to operate in construction, effectively reducing the consumption of construction resources. Foaming technology applies to various types of asphalt, particularly those with high viscosity. Past research has shown that foaming technology can significantly improve the workability of asphalt concrete while maintaining excellent mechanical properties and durability.

2.2. Domestic and International Applications of Warm Mix Asphalt

Internationally, the application of Warm Mix Asphalt (WMA) technology is well-developed, demonstrating significant benefits in environmental protection, construction efficiency, and road quality improvement. Rodrigo Polo-Mendoza et al. explored the sustainable design of incorporating recycled concrete aggregate (RCA) into WMA mixes, highlighting its ability to reduce energy consumption and greenhouse gas emissions. However, excessive RCA usage may increase asphalt content, necessitating careful design to optimize performance【4】. In Chile, Valdés-Vidal et al. evaluated the performance of WMA and Reclaimed Warm Mix Asphalt (RWMA) on highways. Their findings revealed that WMA exhibited similar performance to Hot Mix Asphalt (HMA) in elasticity, moisture sensitivity, and fatigue behaviour while reducing energy consumption and emissions【5】.

Ning Liu et al. conducted a comprehensive evaluation of WMA, demonstrating its ability to reduce fuel usage, production costs, and harmful emissions while improving the working environment. The study emphasized the importance of selecting appropriate additives and methods to optimize WMA performance【6】. Similarly, Gautam Prakash assessed various WMA technologies, including organic and chemical additives and foaming techniques. The research highlighted the benefits of WMA in extending the paving season, reducing harmful emissions, and improving durability through enhanced fatigue and rutting resistance【7】.

Other studies have also demonstrated WMA's advantages in diverse applications. Abdalrhman Milad et al. compared the environmental and economic benefits of WMA and HMA, showing that WMA reduces production temperatures, energy consumption by 20-75%, and emissions while enhancing construction efficiency【8】. Paolino Caputo et al. focused on the role of additives in improving WMA workability and durability, finding that technologies such as Sasobit and Evotherm significantly lower mixing and compaction temperatures, thereby reducing energy usage and emissions【9】. Taqia Rahman et al. examined WMA applications in airport runways, showing that additives like Sasobit improved rutting resistance and reduced construction cooling times, effectively shortening project durations【10】.

In contrast, domestic research and application of WMA technology in Taiwan remain limited, though studies have shown its potential for broader adoption. Junming Qiu's research demonstrated that WMA with chemical and organic additives provides good performance at lower temperatures, comparable to or better than HMA in terms of coating, compaction, and rutting resistance【11】. Chuide Qiu confirmed the energy-saving and carbon-reducing benefits of WMA in experimental applications, suggesting its suitability for extending pavement service life【12】. Similarly, Xianzou Chen investigated additive-based WMA technologies, achieving temperature reductions of up to 35°C during mixing and compaction while maintaining performance comparable to HMA【13】. Lastly, Maoyuan Huang studied warm mix rubber asphalt concrete, confirming its effectiveness in reducing energy consumption and emissions, while enhancing noise reduction, skid resistance, and durability【14】.

This study builds on these findings to explore WMA material characteristics further and implement trial paving projects on Taiwan's provincial highways. This research aims to provide practical insights for future road construction and sustainable development by validating WMA's energy-saving, carbon reduction, and durability performance.

3. Warm Mix Asphalt (WMA) Mix Design and Material Characteristic Testing

3.1. Research Methods and Processes

This study references the results of WMA applications both domestically and internationally, followed by WMA mix design and laboratory testing to confirm that WMA material characteristics meet Taiwan's relevant standards. Subsequent field trials and performance tracking are planned to verify the effectiveness of WMA in field applications. The detailed research methods and processes are as follows:

- Conduct a literature review on the results of WMA applications domestically and internationally.
- Test the material characteristics of WMA to ensure compliance with Taiwan's relevant standards.
- Perform mix design.
- Conduct foam expansion ratio and half-life tests on WMA.
- Evaluate compaction performance using the Superpave Gyratory Compactor (SGC).
- Conduct coating tests.
- Perform Marshall tests.
- Plan WMA field trial paving and performance tracking.

3.2. WMA Mix Design

3.2.1 Selected WMA Technology

Based on the literature reviewed in Section 2.1, the study considered several factors in selecting the WMA technology. Using chemical additives was deemed less feasible due to difficulties verifying the additives used in the asphalt mixing plant. Additionally, organic additives were not selected due to their higher carbon content. Therefore, the foaming method was chosen for this study to improve the low-temperature workability of WMA, ensuring good mixing capabilities.

3.2.2 Material Testing

- Asphalt Binder

The study selected AC-20 as the asphalt binder. Several tests were conducted on the asphalt binder, including density, penetration, and viscosity. The results, shown in Tables 1 to 3, meet the requirements specified in Chapter 02741 of the construction specifications for AC-20 asphalt binder【15】.

Table 1: Asphalt Binder Density Test.

Test Item	Test Value
Relative Density (Specific Gravity, 25℃)	1.034
Density (Unit Weight, kg/m³, 25℃)	1031

Table 2: Asphalt Binder Penetration Test.

Test Item	Test Value	Standard Value
Penetration (0.1mm, 25℃, 100g, 5s)	63	60~70

Table 3: Asphalt Binder Viscosity Test.

Test Item	Test Temperature (℃)	Test Value	Standard Value
Viscosity (poizes)	60	2054	2000±400
Kinematic viscosity (cSt)	135	458	≧210

- Asphalt Foaming Test

The WMA foaming technology involves adding water to hot asphalt, temporarily altering its physical properties. When the hot asphalt comes into contact with water, it turns into steam, creating thousands of tiny asphalt bubbles. This expansion reduces the viscosity of the asphalt, making it easier to mix with aggregates.

The performance of foamed asphalt is evaluated by measuring the expansion ratio and half-life of the foam. According to Chapter 02727 of the Ministry of Interior's Construction Specifications【15】, the expansion ratio should be at least 8 times, and the half-life should be no less than 6 seconds.

- Expansion Ratio: The ratio of the maximum volume of foamed asphalt to its original volume.
- Half-Life: The time required for the foamed asphalt's maximum volume to decay to half its size.

The study conducted expansion ratio and half-life tests on asphalt binder with water content ranging from 1.0% to 4.5%. The results, as shown in Figure 1, indicate that the optimal foaming water content should be between 1.0% and 2.3%. Subsequently, a water content of 1.0% was selected for WMA mixing, and further laboratory tests were conducted.

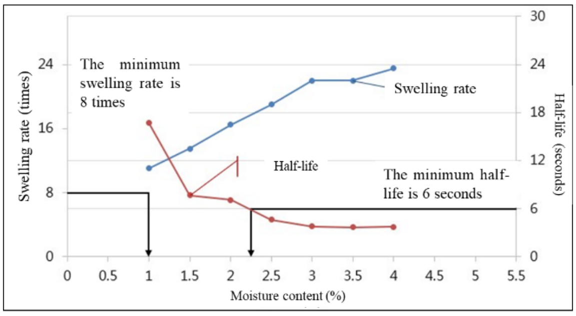

Figure 1: Asphalt Foaming Expansion Ratio and Half-Life Test.

- Aggregates

Tests were conducted on coarse and fine aggregates to measure their bulk-specific gravity and water absorption, as shown in Table 4. Additionally, the aggregates underwent various quality tests, including Los Angeles abrasion, soundness, sand equivalent, fractured particle content, flat and elongated particle content, and Atterberg limits, with the results shown in Table 5. All test results met the specifications outlined in Chapter 02741 of the construction standards for aggregates【15】.

Table 4: Aggregate Specific Gravity Test.

Sample Name	Test Item	Test Value
Coarse Aggregate Retained on 2.36mm Sieve	Bulk Specific Gravity: 23℃/23℃ (Oven-dry Method)	2.616
	Bulk Specific Gravity: 23℃/23℃ (Saturated Surface-Dry Method)	2.646
	Apparent Specific Gravity: 23℃/23℃	2.698
	Water Absorption, %	1.16
Fine Aggregate Passing 2.36mm Sieve	Bulk Specific Gravity: 23℃/23℃ (Oven-dry Method)	2.61
	Bulk Specific Gravity: 23℃/23℃ (Saturated Surface-Dry Method)	2.655
	Apparent Specific Gravity: 23℃/23℃	2.734
	Water Absorption, %	1.75

Table 5: Aggregate Quality Tests.

Item	Test Value	Standard Value
(1) Coarse Aggregate Los Angeles Abrasion Loss (%) (Grade A, 500 Revolutions)	21	≤40
(2) Soundness Loss Rate (%)		
- Fine Aggregate	1	≤15
- Coarse Aggregate	0.4	≤12
(3) Sand Equivalent (%)	73	≥50
(4) Crushed Particle Content of Coarse Aggregate Retained on No.8 Sieve (%)	93	≥90
(5) Flat Particle Content of Coarse Aggregate Retained on No.4 Sieve (%)	2	≤10
(6) Elongated Particle Content of Fine Aggregate Passing No.4 Sieve (%)	0	≤10
(7) Flat and Elongated Particle Content of Coarse Aggregate Retained on No.4 Sieve (%)	8	≤10
(8) Filler		
- Plasticity Index (PI)	NP	≤4

3.2.3 Mix Design Testing

- Design Proportions

This paving project includes both WMA and HMA sections. The selected mix design follows the nominal maximum aggregate size of 1 inch【15】, as shown in Table 6 and Figure 2.

Table 6: Mix Design Proportions.

Sieve Size (mm)	Passing Percentage (%)	Standard Value
37.5 (1-1/2 in.)	100	100
25.0 (1 in.)	95	90～100
19.0 (3/4 in.)	85	—
12.5 (1/2 in.)	68	56～80
9.5 (3/8 in.)	60	—
4.75 (No.4)	45	29～59
2.36 (No.8)	31	19～45
1.18 (No.16)	23	—
0.60 (No.30)	18	—
0.30 (No.50)	13	5～17
0.15 (No.100)	9	—
0.075 (No.200)	4.5	1～7

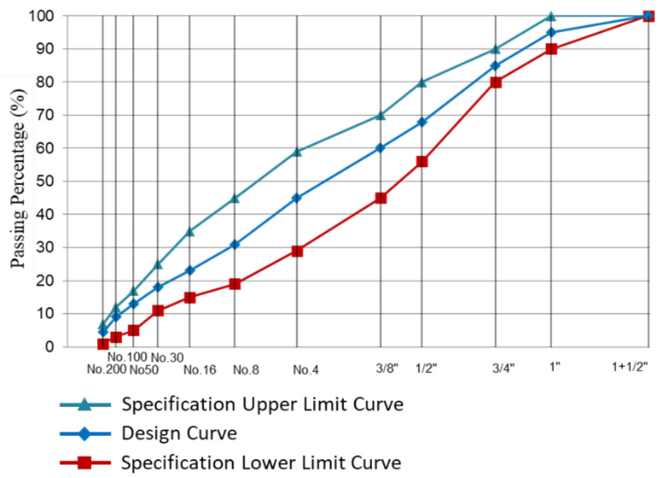

Figure 2: Mix Design Gradation Curve.

- HMA Mix Design

Based on the proportions in Table 6, the study designed HMA with asphalt content levels of 3.5%, 4%, 4.5%, 5%, and 5.5%, followed by Marshall tests. The results are shown in Table 7, with the specifications in Tables 8 and 9【15】. Analysis of the results indicated that the optimal asphalt content is 4.4%, completing the HMA mix design.

Table 7: Marshall Test Results.

Asphalt Content (%)	3.5	4	4.5	5	5.5
Test Item	Test 1	Test 2	Test 3	Test 4	Test 5
Oven-Dried Specific Gravity of Mixed Aggregate (G_sb)	2.616	2.616	2.616	2.616	2.616
Theoretical Maximum Specific Gravity (G_mm)	2.52	2.502	2.483	2.465	2.447
Bulk Specific Gravity of Specimen (Average, G_mb)	2.35	2.367	2.389	2.403	2.412
Effective Specific Gravity of Mixed Aggregate (G_se)	2.659	2.659	2.659	2.659	2.659
Absorption Rate of Asphalt by Aggregate (%) (P_ba)	0.64	0.64	0.64	0.64	0.64
Effective Asphalt Content (%) (P_be)	2.88	3.39	3.89	4.39	4.9
VMA (%)	13.3	13.1	12.8	12.7	12.4
Air Voids (%) (V_a)	6.8	5.4	3.8	2.1	1.4
VFA (%)	49.2	59.1	70.3	80.1	88.8
Stability Value (kgf, Average)	2654	2798	3509	2816	2661
Flow Value (0.25mm, Average)	16	17	19	21	23

Table 8: Asphalt Concrete Specification Table.

Design Standard	Modified
Number of Blows	112
Stability Value (kgf)	≧1838
Flow Value (0.25mm)	12～21
Air Voids (%)	3~5
Retained Strength Index (%)	≧75
Voids in Mineral Aggregate (VMA, %)	See Table 4
Voids Filled with Asphalt (VFA, %)	65～75

Table 9: V.M.A. Specification Table

Nominal Maximum Size mm(in)	Air Voids (%)		
	3.0	4.0	5.0
	V.M.A. (%, Minimum)		
9.5 (3/8 .)	14.0	15.0	16.0
12.5 (1/2.)	13.0	14.0	15.0
19.0 (3/4 .)	12.0	13.0	14.0
25.0 (1.0 .)	11.0	12.0	13.0

- WMA Mix Design

Considering that Taiwan currently lacks specific WMA mix design standards, the asphalt content was selected based on the HMA mix design result of 4.4%. The foaming water content was set at 1%, and two sets of WMA mixing and compaction temperatures were established to confirm the appropriate construction temperature settings, as shown in Table 10.

Table 10: WMA Working Temperature Settings.

Group	Mixing Temperature (℃)	Compaction Temperature (℃)
Group 1	135~140	130
Group 2	125~130	120

➢ Coating Test

Since WMA is mixed at lower temperatures than HMA, the degree of asphalt coating on the aggregate must be verified. The AASHTO T195 method confirmed the coating degree, calculated according to AASHTO R35 as shown in Formula 1. The coating percentage should be at least 95%. The test results are shown in Table 11, and all meet the specification requirements.

$$\text{Percent of coated particles} = \frac{\text{no. of completely coated particles} * 100}{\text{Total no. of particles}} \quad (1)$$

Table 11: WMA Coating Test.

Group	Coating Rate	AASHTO R35
Group 1	99%	> 95%
Group 2	98%	> 95%

➢ WMA Mix Verification with Superpave

The SGC compactor was used to assess the compaction performance of WMA, verifying the compaction performance at different temperatures according to Superpave. The test results are shown in Table 12 and Figure 3, and all conform to Superpave standards.

Table 12: WMA Mix Verification with Superpave.

Compaction Count	Group 1	Group 2	Superpave
	Gmb% of Gmm		
N9	88.4	87.5	≦ 89.0
N125	94.8	94.1	96
N205	96.1	95.3	≦ 98.0

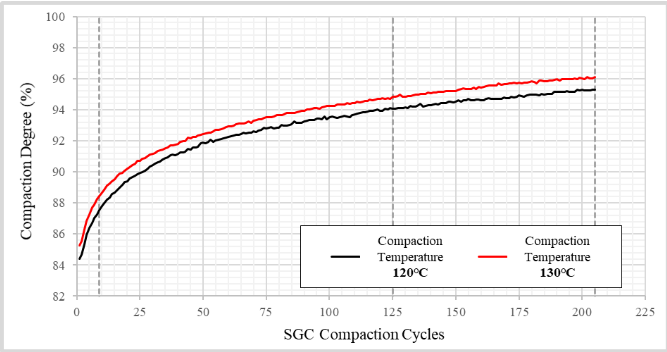

Figure 3: WMA Mix Superpave Compaction Curve.

➢ SGC Compaction Performance Evaluation Test【17】

The primary difference between WMA and HMA is the working temperature. This study analyzed the working temperature of WMA using the SGC rotational compactor method, as described below:

STEP1:Initially, the compaction temperature T is set, and the number of gyrations at 92% of theoretical maximum density (N92)T is determined using the gyratory compactor. The temperature is then reduced by 30℃ to test the number of gyrations (N92)T-30, evaluating the compaction ratio according to Formula 2.

$$\text{Ratio} = \frac{(N92)T-30}{(N92)T} \tag{2}$$

Ratio = Compaction ratio

(N92)T = Number of gyrations at 92% theoretical maximum density at compaction temperature T

(N92)T-30 = Number of gyrations at 92% theoretical maximum density at compaction temperature T-30℃

Table 13: Working Temperature Settings.

Group	Set Compaction Temperature T(℃)	Set Compaction Temperature T-30(℃)
Group 1	130	100
Group 2	120	90

STEP2:Tests were conducted at the two temperature settings outlined in Table 10. The results for Group 1 and Group 2 are shown in Tables 14 and 15 and Figures 4 and 5, respectively. Both sets of results meet the required standards.

Table 14: Group 1 SGC Rotational Compaction Test

Group	Sample ID	Number of Gyrations Corresponding to 92% Gmm		Ratio	AASHTO R35
Group 1 (130℃)	130-1	38	41	1.16	≦ 1.25
	130-2	43			
Group 1 (100℃)	100-1	48	47		
	100-2	46			

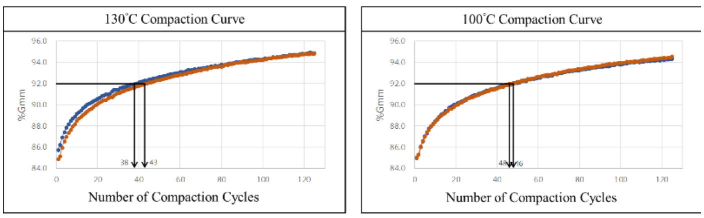

Figure 4: Group 1 SGC Rotational Compaction Curve.

Table 15: Group 2 SGC Rotational Compaction Test

Group	Sample ID	Number of Gyrations Corresponding to 92% Gmm		Ratio	AASHTO R35
Group 2 (120℃)	120-1	47	48	1.09	≦ 1.25
	120-2	49			
Group 2 (90℃)	90-1	49	53		
	90-2	56			

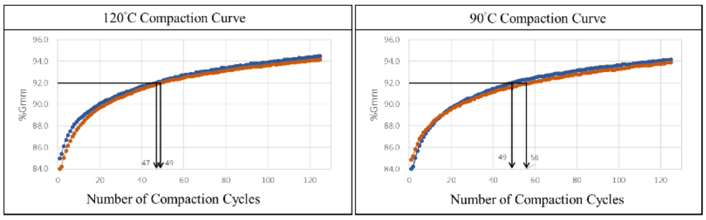

Figure 5: Group 2 SGC Rotational Compaction Curve.

The results from the coating test, Superpave verification, and SGC compaction performance evaluation indicate that both temperature settings in this study meet the relevant standards. However, considering that no current studies or projects are implementing WMA paving, the more conservative Group 1 temperature setting was selected for further work.

4. Construction Planning and Performance Tracking

4.1. WMA Trial Paving Plan

After confirming the material properties of WMA, this study proceeded with planning the subsequent trial mixing operations at the mixing plant and the field trial paving, along with arranging the relevant tests.

4.1.1 Mixing Plant Trial Plan

The initial plan involved conducting trial mixing operations at the mixing plant to ensure that the WMA produced meets the required specifications. The trial mixing plan at the mixing plant included the following:

- Asphalt Mixing Equipment: The equipment used for WMA mixing is the same as that used for HMA, with the addition of asphalt foaming equipment. Before mixing, the production equipment should be checked to ensure proper foaming of the asphalt during mixing.
- Mixing Temperature: Based on the findings in Chapter 3, a conservative mixing temperature of 140°C was set to ensure the viscosity and fluidity of the asphalt binder. Temperature measurements were accurately taken during production.
- Production Process: According to the expansion ratio and half-life tests shown in Figure 1, trial mixing was conducted at the mixing plant with water contents of 1.0%, 1.5%, and 2.0%, as shown in the process flow diagram in Figure 6.
- WMA Quality Control: After the trial mixing, tests were conducted on the mixed samples with different water contents to ensure that the results met the relevant standards:
  - ➢ Foamed asphalt expansion ratio and half-life tests.
  - ➢ Coating test for the mixed material.
  - ➢ Samples from each water content were subjected to SGC compaction, Marshall, TSR, and Hamburg wheel-track tests.

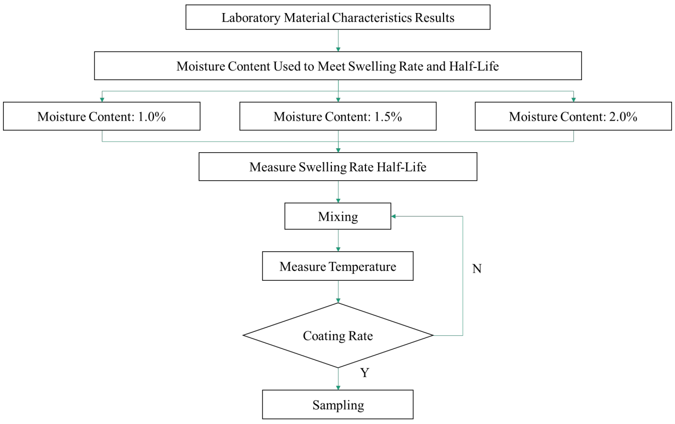

Figure 6: Production Process Flow Diagram.

4.1.2 Field Trial Paving Plan

Following the mixing plant trials, the plan moved on to the WMA field trial paving. The plan included arranging the necessary tests and performance tracking to compare the results of WMA and HMA. The field trials involved milling and repaving the surface layer of an existing pavement, using both HMA and WMA for comparison.

- Trial Paving Location: The trial paving was planned to be conducted on Provincial Highway 2, with the construction scope shown in Figure 7.

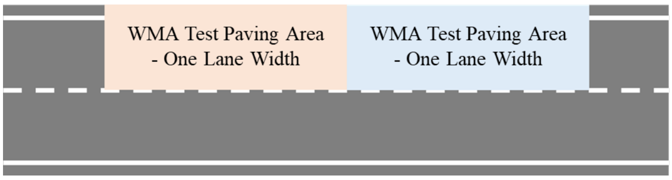

Figure 7: Trial Paving Construction Scope.

- Construction Method: WMA and HMA were constructed per the specifications outlined in Chapter 02742 for asphalt concrete pavement, with the only difference being the working temperature. Based on the findings in Chapter 3, the WMA mixing temperature was set at 140°C.
- Construction Quality Inspection:
  - ➢ During Construction:

    A coating test was conducted before the WMA was dispatched from the plant.

    During the trial paving, accurate temperature measurements were taken at the plant and on-site for both WMA and HMA, along with measurements of natural gas consumption to assess the carbon reduction benefits.
  - ➢ **Post-Construction Inspection:**

    Compaction Inspection: Core samples were taken from the WMA and HMA pavements and subjected to density tests. Additional samples were compacted in the lab using the Marshall method to create three specimens whose average density was used as a benchmark. Compaction was calculated using Formula 3:

$$\text{Compaction}(\%)=\frac{\text{Field core sample density}}{\text{Benchmark density}}\times 100\% \tag{3}$$

    Samples from both WMA and HMA were subjected to Marshall tests, with the results required to meet the specifications outlined in Table 8.

    TSR Testing: Water can cause asphalt binder to lose adhesion to aggregates, accelerating pavement deterioration, a phenomenon known as stripping. Following AASHTO T 283, TSR tests were conducted to determine if the material might strip. Six compacted specimens were prepared; three were tested in dry conditions, and the other three were subjected to freeze-thaw cycles in water-saturated conditions before loading. The results measured the indirect tensile strength of the specimens.

    Samples from the WMA and HMA mixtures were tested for oil content and sieve analysis. The asphalt content and aggregate gradation results were compared with the design mix in Table 6, with allowable deviations specified in Table 16.

Table 16: Asphalt Concrete Gradation and Asphalt Content Tolerances.

Sieve Size (mm)	Allowable Deviation (%)
≧4.75 (No.4)	±7
2.36-0.150 (No.8-No.100)	±4
0.075 (No.200)	±2
Asphalt Content	±0.4

4.2. Performance Tracking Plan

A comprehensive plan has been formulated for subsequent performance evaluations on the completed WMA and HMA pavement surfaces, aiming to assess WMA technology's durability and long-term performance. As the construction phase was only recently completed, the performance tests outlined in the plan have yet to be initiated, and no experimental data are currently available. These evaluations, detailed in Table 17, are intended to provide critical insights through systematic performance tracking in future stages of the study.

Table 17: Performance Tracking Plan.

Performance Tracking Item	Tracking Method	Tracking Frequency
Pavement Damage Investigation	Smart Detection Device	Post-construction, 3 months, 6 months, and 12 months after construction
Rutting Test	3-Meter Straightedge	Post-construction, 3 months, 6 months, and 12 months after construction
Hamburg Wheel-Track Rutting Test	Core Sample Testing	Post-construction, 6 months, and 12 months after construction

4.2.1 Pavement Distress Survey

This study tracked the deterioration durability of WMA and HMA surfaces using an intelligent detection system. The system employed cameras to capture road surface images, measuring the maximum pavement distress area. The images had a resolution of 2048×1536 pixels, and the road surface was photographed at 40 km/h, as illustrated in Figure 8. The system's primary function was to collect road surface images, with AI cloud technology automatically interpreting and detecting deterioration.

The recognition software was based on deep learning, a subset of machine learning, which uses artificial neural networks for data representation learning. The study followed the "Urban Road Maintenance and Technical Specification Manual – Flexible Pavement Distress Survey Manual," published by the Ministry of Interior’s Construction Department in 2002, to design PCI computer calculation diagrams, including the coding principles and processes needed for PCI calculations. PCI ratings were then automatically calculated to evaluate pavement distress.

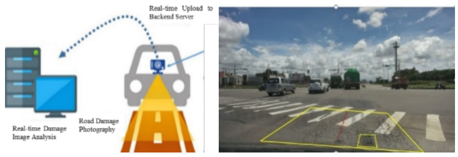

Figure 8: Smart Detection System Diagram.

4.2.2 Field Rutting Test

Pavement rutting occurs due to repeated loading, causing elastic deformation and the permanent deformation of pavement materials or subgrade, leading to rutting failure. Significant rutting can cause structural damage to the pavement, commonly occurring in wheel paths. A 3-meter straightedge combined with a vernier calliper was used to measure rut depth, as shown in Figure 9. Rut depth was then used to evaluate the load-bearing capacity of WMA and HMA, assessing whether the pavement's current load capacity was sufficient.

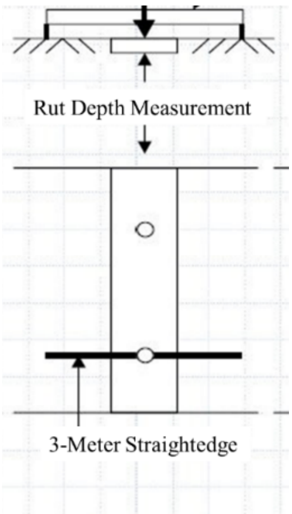

Figure 9: Rutting Test Diagram.

4.2.3 Hamburg Wheel Track Test

The purpose of the Hamburg Wheel Track Test was to evaluate the rutting and moisture susceptibility of asphalt mixtures under repeated loading in a submerged state. The test measured the permanent deformation response of WMA and HMA to concentrated loads and moisture. The test involved loading compacted asphalt pavement specimens submerged in water using a reciprocating wheel tracking device, measuring the asphalt mixture's resistance to moisture damage and rutting. The test report included parameters such as creep slope, stripping slope, and stripping inflection point.

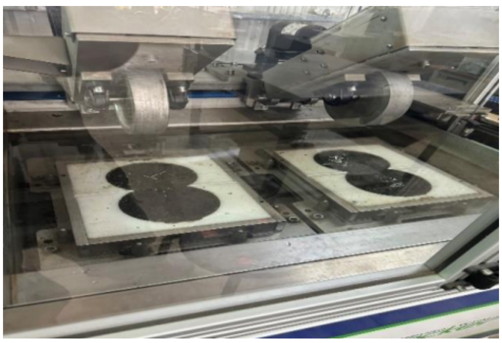

Figure 10: Hamburg Wheel Track Test.

5. Conclusion and Recommendations

5.1. Conclusion

This study systematically evaluated Warm Mix Asphalt (WMA) technology through laboratory tests and mix design phases, confirming its feasibility and compliance with Taiwan's construction standards. The experimental results demonstrated that WMA can significantly enhance the sustainability of road construction by reducing energy consumption and greenhouse gas emissions while maintaining performance comparable to traditional Hot Mix Asphalt (HMA).

The key findings include the following optimal parameters for WMA construction:

- Asphalt Content: The optimal asphalt content is 4.4%.
- Foaming Water Content: The recommended range is between 1.0% and 2.3%.
- Mixing and Compaction Temperatures: Two sets of mixing temperatures (130°C and 140°C) and compaction temperatures (120°C and 130°C) were validated, both meeting coating and compaction standards.

For subsequent plant trial mixing, it is recommended to experiment with water contents of 1.0%, 1.5%, and 2.0%, followed by Marshall, TSR, and Hamburg wheel-track tests to verify the laboratory-established parameters. Field trial paving on Provincial Highway 2 will evaluate performance under real-world conditions. Natural gas consumption should be measured during construction to quantify WMA's carbon reduction effects.

A robust performance tracking plan has been established, encompassing pavement distress surveys, rut depth tests, and Hamburg wheel-track evaluations. These tests will be conducted post-construction and at intervals of 3, 6, and 12 months to systematically assess WMA's durability benefits.

5.2. Practical Insights and Recommendations

This study provides several practical insights and recommendations for the future road engineering industry:

- Adoption of WMA Technology: Given its demonstrated energy-saving and carbon-reduction benefits, WMA technology should be prioritized in both new construction and pavement maintenance projects. The technology is particularly suited for regions with strict environmental standards or sustainability goals.
- Performance Validation: Large-scale field trials should be conducted to validate the long-term performance of WMA under diverse environmental conditions. Future studies could explore integrating digital tools such as AI-based performance monitoring to enhance data accuracy and decision-making efficiency.
- Policy and Standards Development: Policymakers are encouraged to develop and implement specific standards for WMA mix designs, ensuring consistent quality and performance across projects.
- Collaborative Research: Cross-disciplinary collaboration among engineers, environmental scientists, and policymakers is essential to optimize WMA technology and accelerate its adoption.

By addressing these practical aspects, this study lays the foundation for the broader implementation of WMA technology in Taiwan and beyond, contributing to global efforts toward sustainable infrastructure development and net-zero emission targets.

References

National Center for Asphalt Technology. (2005). Asphalt Technology News, 17(2).

Goh, S. W. (2012). Development and improvement of warm-mix asphalt technology (Doctoral dissertation). Michigan Technological University.

Zaumanis, M. (2010). Warm Mix Asphalt Investigation (Master's thesis). Technical University of Denmark.

Polo-Mendoza, R., Peñabaena-Niebles, R., Giustozzi, F., & Martinez-Arguelles, G. (2022). Eco-friendly design of Warm Mix Asphalt (WMA) with recycled concrete aggregate (RCA): A case study from a developing country. Construction and Building Materials, 326, 126890.

Valdés-Vidal, G., Calabi-Floody, A., Sanchez-Alonso, E., Díaz, C., & Fonseca, C. (2020). Highway trial sections: Performance evaluation of warm mix asphalt and recycled warm mix asphalt. Construction and Building Materials, 254, 120069.

Liu, N., Liu, L., Li, M., & Sun, L. (2023). A comprehensive review of warm-mix asphalt mixtures: Mix design, construction temperatures determination, performance, and life-cycle assessment. Road Materials and Pavement Design.

Prakash, G., & Suman, S. K. (2021). An intensive overview of warm mix asphalt (WMA) technologies towards sustainable pavement construction. Innovative Infrastructure Solutions.

Milad, A., Babalghaith, A. M., Al-Sabaeei, A. M., Dulaimi, A., Ali, A., Reddy, S. S., Bilema, M., & Yusoff, N. I. M. (2022). A comparative review of hot and warm mix asphalt technologies from environmental and economic perspectives: Towards a sustainable asphalt pavement. International Journal of Environmental Research and Public Health, 19, 14863.

Caputo, P., Abe, A. A., Loise, V., Porto, M., Calandra, P., Angelico, R., & Rossi, C. O. (2020). The role of additives in warm mix asphalt technology: An insight into their mechanisms of improving an emerging technology. Nanomaterials, 10(6), 1202.

Rahman, T., Dawson, A., & Thom, N. (2020). Warm Mix Asphalt (WMA) for rapid construction in airfield pavement. Construction and Building Materials.

Chiu, C.-M. (2018). The preliminary study of laboratory Warm Mix Asphalt concrete performance \u2013 Take chemical and organic additives as an example (Master's thesis). National Central University, Taiwan.

Qiu, C.-D. (2017). Research on the strategy of introducing warm mix asphalt in Taiwan. Research Report, National Science Council, Executive Yuan, Taiwan.

Chen, X.-Z., Hong, M.-Z., & Su, Y.-M. (2017). Performance study of warm mix asphalt concrete. Taiwan Highway Engineering Journal, 43(5), 2-35.

Huang, M.-Y. (2023). The study on paving performance of warm mixtures using crumb rubber modifier asphalt (Master's thesis). National Central University, Taiwan.

Directorate General of Highways, Ministry of Transportation and Communications. (2022). General requirements for asphalt concrete (02741).

Construction and Planning Agency, Ministry of the Interior. (2021). Cold recycled asphalt concrete (02727).

AASHTO. (2018). Standard Method of Test for Determining Degree of Particle Coating of Asphalt Mixtures (AASHTO T 195). Washington, D.C.: American Association of State Highway and Transportation Officials.

The Asphalt Institute. (2014). Asphalt Mix Design Methods (Manual Series No. 2 (MS-2), 7th ed.).

Journal of Road Engineering Association of Asia and Australasia

Journal homepage: www.reaaa.net

JREAA – 1(1)2025: 14-19

OPEN ACCESS

Ground Investigation and Assessment of Differential Settlement at a Bridge Approach After Rehabilitation Using Polyurethane Foam Grout Injection in Kuala Selangor, Malaysia

Eng Boon Cheng[1], Ismacahyadi Bagus Mohamed Jais[2]*, Sherliza Zaini Sooria[1]

*Corresponding author, e-mail address: ismac821@uitm.edu.my

[1]*Geotechnical Research Laboratory, Center of Excellence in Engineering and Technology JKR (CREaTE), Public Works Department of Malaysia*

[2]*School of Civil Engineering, College of Engineering, Universiti Teknologi MARA, Shah Alam, Malaysia*

ABSTRACT

Differential settlement at transition approaches poses significant challenges, as the resulting unevenness at the approach section can adversely impact rideability and cause discomfort to road users. The primary causes of differential settlement include high dynamic loads from heavy traffic, consolidation of foundation soils, poor compaction, and the migration of earth fill beneath voids underneath the piled embankment or bridge abutment due to global settlement of the surrounding area. This study examines the efficacy of polyurethane (PU) foam/resin injection as a remedial measure for differential settlement at bridge abutment approaches, with a focus on a case study conducted at Section 481.7, Federal Route (FT) 05, Kuala Selangor, Malaysia. A comprehensive geo-forensic investigation, utilizing Mackintosh probes and Electrical Resistivity Tomography (ERT), was conducted to characterize subsurface conditions and identify weak zones. The findings revealed the presence of highly compressible strata and potential voids beneath the piled embankment, contributing to the differential settlement observed. PU foam/resin injection was subsequently applied due to its lightweight capabilities to overcome additional imposed overburden and fill voids. The effectiveness of this ground improvement technique was assessed through a 14-month settlement monitoring program, which demonstrated that the PU foam/resin injection successfully mitigated differential settlement, with deformations remaining within acceptable limits. This case study underscores the versatility and effectiveness of PU foam/resin injection as an alternative solution for addressing differential settlement at bridge approaches while also highlighting the critical role of thorough geotechnical characterization in selecting appropriate ground improvement methodologies for infrastructure projects.

ARTICLE INFO

Article History:
Received 22 August 2024
Received in revised form
10 Dec 2024
Accepted
01 Apr 2025
Available online
01 May 2025

Keywords:
Differential Settlement
Abutment Approach
Ground Improvement
Polyurethane Foam/Resin

1. Introduction

Post-construction settlement has always been a challenge in the construction of road embankments over soft ground. The ground settlement occurs due to the volume change of soft soil as the excess pore water pressure dissipates when the ground is loaded to strengthen the foundation of the building and pavement. In Malaysia, many cases of differential settlement occur at bridge transition zones, especially along the coastal region. The persistent settlement problem, along with the significant differential settlement magnitude at the bridge approach on the viaduct section of Federal Route (FT) 05 right after Sungai Selangor, has caused discomfort for road users and, at times, posed dangers, especially for heavy vehicles. As a result, the Public Works Department in Kuala Selangor, Malaysia, has received numerous complaints regarding this issue. Therefore, an effective solution needs to be proposed to mitigate this differential settlement problem at the abutment approach.

Polyurethane (PU) foam/resin grout injection has been identified as one of the remedial solutions for ground improvement (Mohamed Jais, 2017). Polyurethane (PU) foam/resin is a cellular solid polymer with a honeycomb-like structure. This design is meticulously engineered to achieve specific properties tailored to various applications (Gary & Krishan, 2021). PU foam/resin is a lightweight material that improves the poor foundation (soft soil) without imposing any additional overburden load on the existing foundation and, at the same time, increases the soil-bearing capacity. In addition, PU foam/resin has an expandable property that helps in filling voids within soils to reduce soil compressibility. This method effectively reduces the voids between soils, improves ground conditions, and addresses the differential settlement issue in historic buildings (Mohamed Jais, 2017; José, 2018). Replacing cement with polyurethane resin can reduce settlement as well as the compressibility of weak foundation soil while enhancing its strength (Sidek et al., 2015). Various features of polyurethane behaviour have been widely investigated since the 1960s (Buzzi et al., 2008). Polyurethane foam/resin is a complex and unique polymer material with a wide range of physical and chemical properties, containing urethane links that form a chain of organic units. Polyurethane foam/resin comes in two (2) types, which are hydrophobic and hydrophilic polyurethanes. Mohamed Jais (2017) reported that hydrophobic polyurethane is suitable for ground repair and remediation, with an expansion rate of six to twenty times its liquid volume. Yu et al. (2013) refer to hydrophobic polyurethane as a foam with an accelerator to control the curing time. The advantage of using this foam is that it can expel water during expansion before stabilizing the soil. This study aims to assess the effectiveness of polyurethane foam grout injection in mitigating differential settlement.

In Malaysia, PU foam/resin grout injection has been implemented in several projects, including expressway sections, bridge abutments, and various building structures.

2. Location of Bridge Approach at FT 05 Kuala Selangor

The Federal Route (FT) 05, as shown in Figure 1, is one of the three primary north-south backbone federal roads running along the west coast of Peninsular Malaysia. Spanning 655.85 km, this federal highway stretches from Skudai in Johor to Jelapang in Perak, making it the shortest among the three main backbone of federal highways. Despite the development of the North-South Expressway (E1 and E2), Federal Route FT05 remains heavily utilized by travellers and commuters along the west coast of Peninsular Malaysia. According to the Road Traffic Volume of Malaysia (RTVM) report in 2018, the Level of Service (LOS) for FT05 was rated at D, indicating moderate congestion with unstable traffic flow and restricted driver speed choices. Additionally, vehicle surveys conducted in 2018 revealed that the route handled 3,430 vehicles per hour. The traffic composition included 56% cars and taxis, 13% vans, 8.8% medium lorries, 5.8% heavy lorries, 1.2% buses, and 15.2% motorcycles.

Kuala Selangor Bridge, formally known as Sultan Salahuddin Abdul Aziz Shah Bridge at FT05, is the location of the bridge approach to be investigated in the section right after Sungai Selangor East Bound and West Bound at FT05. The coordinate of the site of study is 03°20'28.3" N, 101°15'17.6" E, along the FT05.

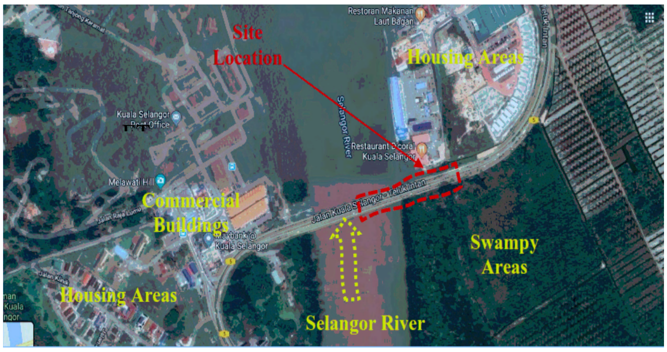

Figure 1: Location of study, Section 487.1 FT05

The bridge approach on the viaduct section of FT05, just beyond Sungai Selangor, has repeatedly experienced settlement and undulating issues. Figure 2 shows the different settlements that occurred at this bridge approach. The traditional solution often used to address this recurring problem is regulating and resurfacing the affected section by adding a premix to realign the bridge approaches with the transition earth vertically filled embankment. However, this will further add the surcharge load to the soft soil, worsening the settlement problem.

Figure 2: Differential settlement occurred at the abutment approach of Section 481.7 FT 05

3. Geo-forensic Investigation

3.1 Site Geomorphology and Geology

The site topography at the Kuala Selangor Bridge is predominantly flat terrain, surrounded by commercial buildings, residential areas, and, notably, swampy regions near the bridge approaches. These swampy areas encircling the bridge significantly contribute to the settlement observed in the viaduct section due to the continuous settlement of the underlying roadbed.

The geological formation in the Kuala Selangor area is primarily dominated by Quaternary deposits, which consist of marine and continental materials such as clay, silt, sand, and minor gravel. As depicted in the geological map shown in Figure 3, the study area is underlain by fine-grained soils, particularly silt and clay, which dominate the subsoil profile at the site. These soil characteristics play a crucial role in the ongoing settlement processes observed at the bridge site.

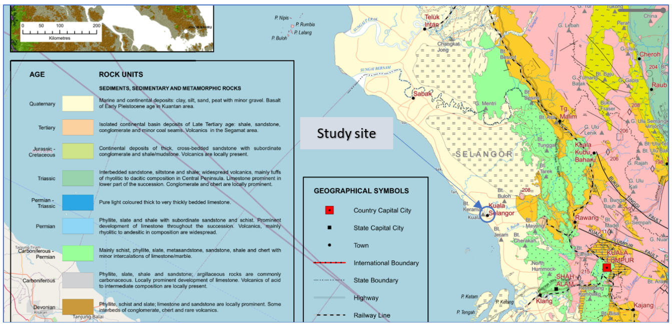

Figure 3: Geological formation of the site location at Kuala Selangor, Selangor (JMG 2014)

3.2 Field Investigation

To investigate the condition of the underlying soil and identify potential weak zones at the study site location, Mackintosh probes and Electrical Resistivity Tomography (ERT) were conducted. ERT effectively predicts the potential settlement in embankment areas during road construction phases (Saha, Kundu and Dey, 2019). Hence, the results of ERT complements with the Mackintosh probe readings and geological information were applied to detect the weak layers within the subsurface profile. Three resistivity lines were proposed, i.e., Line 1 (East Bound, slow lane to Teluk Intan), Line 2 (East Bound, median lane to Teluk Intan), and Line 3 (West Bound, slow lane to Klang). Each line consisted of five Mackintosh probe points, totalling 15 probe points at this site location, as shown in Figure 4. The ERT survey, spanning 180 to 800 meters from the fill embankment to the pile embankment, was conducted using an ABEM Terrameter SAS

4000 Lund Imaging System. The survey employed the Wenner array protocol with 41 electrodes arranged in a straight line. The collected data were processed with RES2DINV software to produce an inverse model that approximates the actual subsurface profile, allowing for the identification of resistivity variations related to factors such as fracturing and moisture content in the ground. This enabled further interpretation of the problematic subsurface layers due to theirtheir different stiffness. The heterogeneity of the subsurface material, presented through an integrated analysis of ERT and MP data, hashas been used to plan sustainable ground improvement strategies on a local scale, offering a fast, low-cost approach with extensive data coverage.

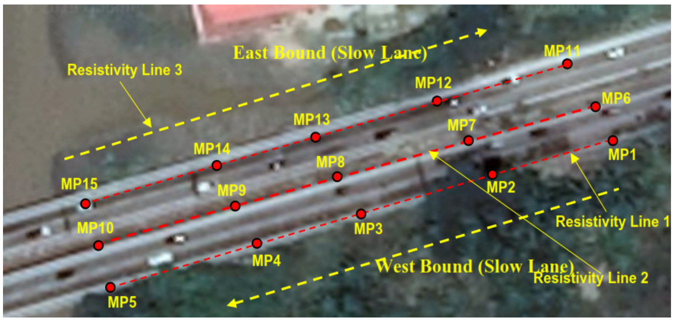

Figure 4: Test location of electrical resistivity survey lines and Mackintosh probes

4 Results and Analysis

4.1 Mackintosh Probes

Based on the probing conducted, the geotechnical subsurface conditions are summarized across three distinct lines:

Line 1: The soil layer is generally well-compacted to specification, with strength correlations ranging from 355 kPa to 475 kPa, making it suitable for load bearing, except at MP3, which is located in the middle of the section. At this point, the soil condition is critically weak due to the presence of voids beneath the embankment, leading to the migration of the compacted earthfill beneath it.

Line 2: The subsurface condition is less favourable compared to Line 1, with weak spots identified at MP8 and MP9, particularly at MP9, which is in the middle of the section. The soil condition at MP9 is more critical than at MP8, as the soil at the centre of the median has migrated beneath the adjacent piled embankment. This migration has weakened the subgrade, resulting in the settlement of the foundation soil beneath the piled embankment. Consequently, the compacted soil has migrated beneath the embankment, further weakening in the middle section of the line. Additionally, the presence of a water table was detected at MP8 and MP9, as indicated by a sudden drop in readings at a depth of 1.2 meters.

Line 3: The earthfill is well-compacted, with most of the soil being dense. The compacted fill material is highly stable, as evidenced by probe readings of 400 blows per 300 mm of penetration. The probing results for the first and third lines indicated that the sand has been compacted to specification and that the presumed clay has undergone approximately 90% consolidation.

While Lines 1 and 3 show adequate compaction and stability, Line 2 exhibits critical weaknesses that require attention, particularly in the middle section, where voids and groundwater table presence have compromised the soil integrity.

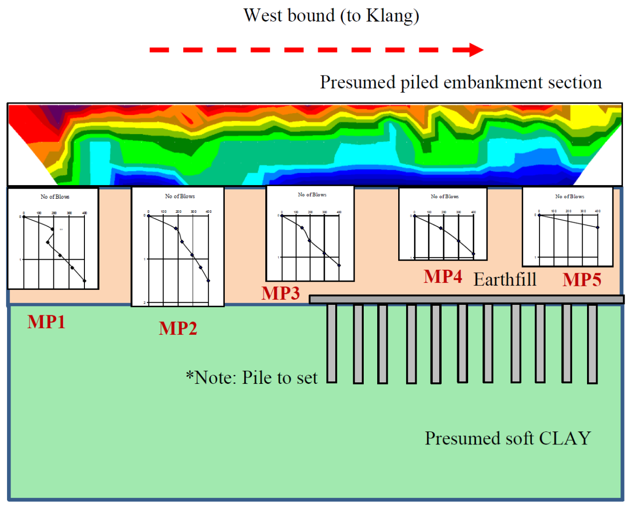

Figure 5: Subsoil profile for Line 1 with results of MP1 to MP5

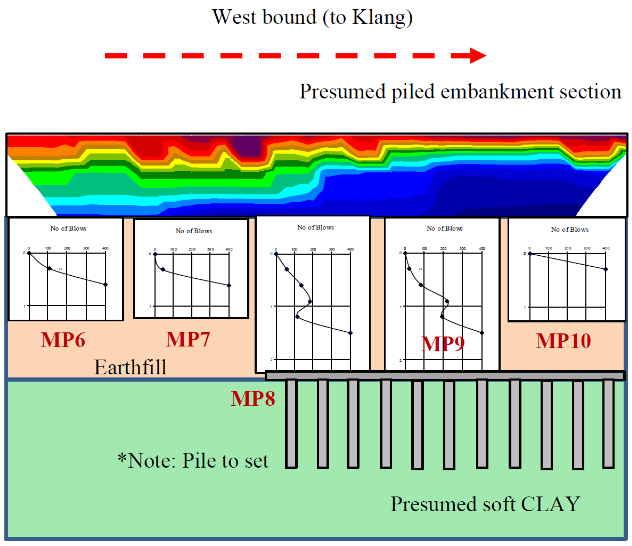

Figure 6: Subsoil profile for Line 2 with results of MP6 to MP10

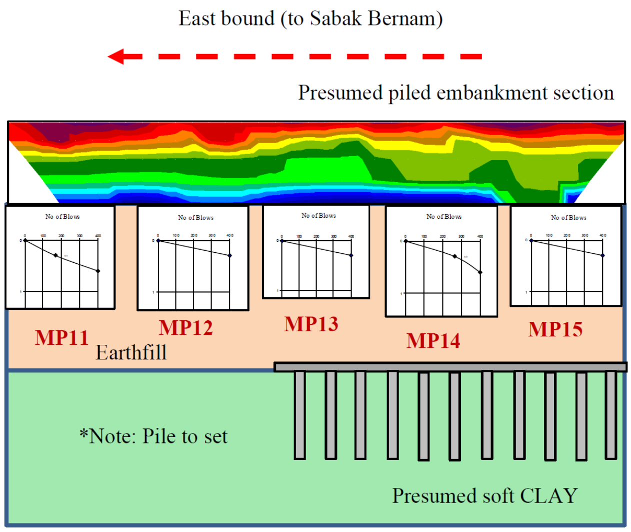

Figure 7: Subsoil profile for Line 3 with results of MP11 to MP15

4.2 Electrical Resistivity Tomography

The subsurface profile was then investigated using electrical resistivity tomography (ERT) to identify the nature of the voids or saturated zone that caused the approach to experience differential settlement. The geometry and electrical resistivity anomaly distribution have been determined by analyzing ERT data obtained along the settlement zones. ERT mapped the ground inconsistencies, which can extend the surface information observed during the physical mapping. The information from the ERT will suggest decision-making regarding the location of the weak layer underneath the pavement structure.

Based on the resistivity profile line 1 shown in Figure 8, below the piled embankment (0 to 50 m), there are potential cavities, weakening, and water pockets. The clay is saturated from 0 to -50 m, and there is a possible aquifer zone below 5 m since the fill area adjacent to the highway was previously a mangrove area. However, at the top layer of this section, the soil layers are in dense and compact condition as indicated by the resistivity readings, which are more than 500 ohms. The profile showed that the depth of the saturated zone (suspected CLAY layer depth) goes down to 19.7 m and that partly the clay has experienced 90 % consolidation.

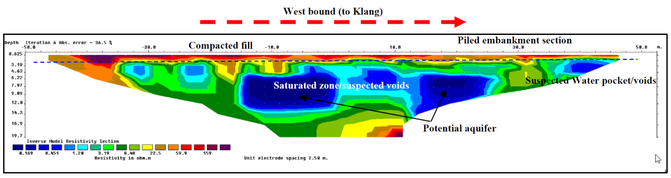

Figure 8: Electrical resistivity profile underneath line 1

Resistivity survey profile line 2 (Figure 9) gives a glimpse of the median section and indicates that the section is rather weak. According to the ERT profile, potential voids are below the piled embankment, with resistivity values below 50 ohms. It is suspected that the voids have existed between the slab soffit and the ground beneath the piled slab soffit due to the previous consolidation settlement and water in the soil. Hence, it has brought the possibility of the earthen material migrating towards the voids underneath the piled embankment. A very low resistivity zone is also observed at sections -5 to -8m and -10m to -30m, which may indicate a possible void or fully saturated highly compressibility zone.

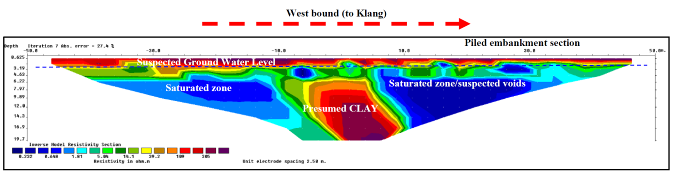

Figure 9: Electrical resistivity profile underneath line 2

Resistivity profile line 3, as in Figure 10, confirms the probe's readings at line 3, with the potential voids and water pockets area being much more prominent in comparison to Lines 1 and 2. Moreover, beneath the compacted fill, the clay is undergoing consolidation since it is still saturated, and the resistivity reading is below 50 ohms. Settlement occurs due to the existing saturated and highly compressible soil, thus the migration of earthen materials towards the voids area underneath the pile embankment slab soffits.

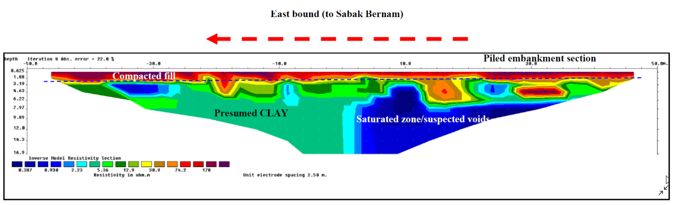

Figure 10: Electrical resistivity profile underneath line 3

As a summary, the ERT profiles have shown critical sections of differential settlement, which is at the transition zone between the piled embankment and the earth-fill embankment where the potential voids/saturated zones are below the piled embankment causing the earth-fill material to migrate towards this zone. Based on the resistivity image, the section, which is assumed to be constructed on piled embankments, does not experience massive settlement. However, beneath the piled embankment, voids start to appear, causing the fill material at the transition zone to migrate into the voids, causing differential settlement and sudden road humps. This transition section underneath the piled embankment will be treated with PU foam/resin injection to plug the voids, introducing a lightweight grout curtain and preventing the soil from migrating underneath the piled embankment.

5. Rehabilitation using Polyurethane Foam/Resin

To address the issue of settlement in the embankment area, PU foam/resin injection was proposed as an alternative solution to reduce the effect of settlement at the transition approach. This method involves injecting PU foam/resin, with the material properties shown in Table 1, into the edges of the embankment slab where cavities have formed beneath the existing ground due to soil migration. The PU foam/resin will fill these cavities, providing essential support without adding weight or pressure to the existing foundation soil. Its lightweight nature ensures that the integrity of the surrounding soil is maintained, preventing further settlement while stabilizing the embankment effectively.

Table 1: Design properties of the polyurethane foam/resin [6].

Description	Value	Unit
Unit weight of the polyurethane foam/resin, γ	3	kN/m^3
Stiffness modulus, E	15,000	kN/m^2
Poisson's ratio, ν	0.3	-
Compressive strength, σ	2.2	MPa
Permeability, k	1 x 10-12	m/s

The implementation of a polyurethane (PU) foam/resin injection system at the bridge approach is illustrated in Figure 11. Injection points were strategically spaced between 1 m and 2 m intervals, resulting in 60 injection points, as detailed in the configuration layout in Figure 12. Each point was drilled using a 32 mm diameter mechanical drill to a minimum depth of 3 m, allowing for the insertion of steel rods and subsequent injection of the PU foam/resin. The injection targeted the edges of the piled embankment, effectively sealing voids and preventing the migration of fill material into cavities formed by global ground settlement. The pressure applied was between 500 - 800 psi to introduce the curtain wall and 800 - 1,200 psi to stabilize and strengthen the weak soil layer. The polyurethane foam/resin expanded and cured approximately 15 minutes after injection. Following the dismantling of the packer, the injection holes were grouted with appropriate materials. Any excess or diffused PU foam/resin was carefully removed. This procedure resulted in the creation of a lightweight curtain wall, which mitigates the migration of compacted soil into void spaces, thereby reducing the rate of differential settlement at the approach section.

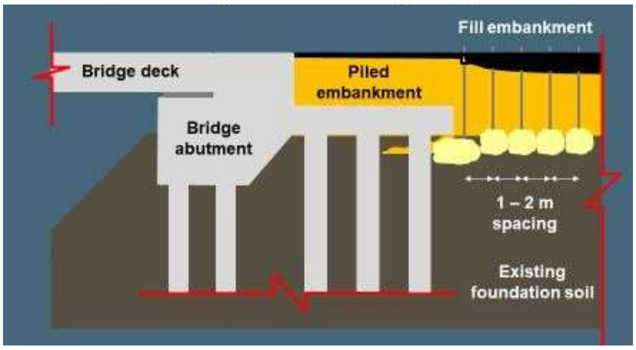

Figure 11: Rehabilitation concept with polyurethane foam/resin at abutment approach (Courtesy of Geocon (M) Sdn. Bhd.)

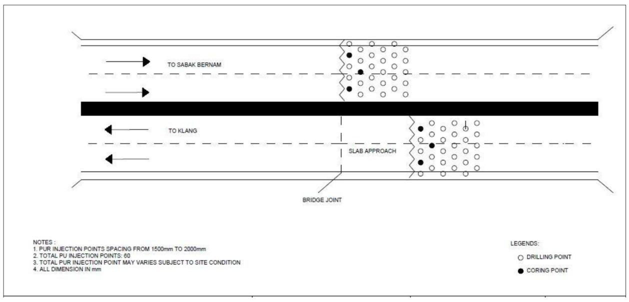

Figure 12: Configuration of injection points using PU foam/resin at the abutment approach

The rehabilitation work using PU foam/resin was conducted during the midnight hours to minimize disruption to traffic and avoid complaints from road users due to the necessary road closures. The quantity of PU foam/resin required to fill the detected cavities was determined through an analysis of data obtained from Electrical Resistivity Tomography (ERT) and Mackintosh probe tests. Approximately 2,605 litres of PU foam/resin were injected beneath the abutment approach to address the settlement issues effectively.

The impact of injection pressure was a critical consideration during the process. When the soil is weak, the pressure exerted during injection causes the liquid PU to expand rapidly, forming a solid, inert PU foam resin at the appropriate pressure. However, if the injection pressure is excessive, it can uplift and bulge the road surface. In such cases, the affected area can be trimmed and the bulged asphalt removed. The surface can then be restored to the required level by resurfacing with cold-mix asphalt, ensuring compatibility with the existing pavement surface.

6. Performance Evaluation

A deformation survey was conducted at the study site to measure displacement using the DL-500 Topcon Digital Level, an automatic electronic digital level. Settlement monitoring was carried out over 14 months to assess the effectiveness of PU foam/resin injection for reducing differential settlement. For this purpose, eight settlement markers were installed. Figure 13 illustrates the arrangement of these markers: SM 1 and SM 6 were installed on the bridge structure, SM 2, SM 3, SM 7, and SM 8 were positioned in the transition zone (just before and after the bridge section), and SM 4 and SM 5 were located on the ground in the median between the two bridges.

Figure 13: Location of settlement markers installed at the study site

Based on the observed data, it can be concluded that the settlement readings for all markers over the 14 months remained within tolerable limits, defined as 250 mm over 5 years for total settlement and 100 mm over 5 years for differential settlement. However, significant settlement was observed at markers SM 2 and SM 3 (located on compacted fill) shortly after the PU foam injection, indicating a substantial drop in the road surface. This drop occurred as the PU foam expanded, sealing the edges of the piled embankment and filling the underlying cavities while simultaneously densifying the soil beneath the structures. In contrast, settlements at SM 4 and SM 5 increased gradually, likely due to the absence of injection points in the median of the approach. The settlement data varied over the 14 weeks, influenced by the pressure of the PU foam's buoyancy and the rearrangement of soil particles to achieve a stable compaction state. As presented in Figure 14, the deformation trends reflected both settlement and uplift phenomena, attributed to the buoyancy effect of the PU foam injected at the abutment approach.

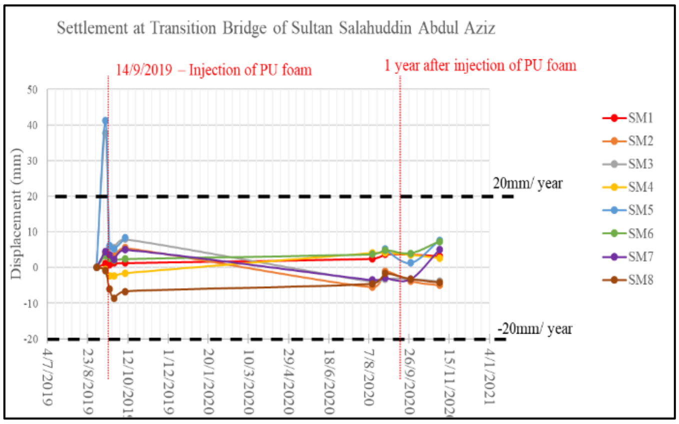

Figure 14: Settlement monitoring data for 14 months at the study site

7. Conclusion

Differential settlement is a prevalent concern in zones where disparate treatment methods are employed during road construction, particularly at the interface of structural and non-structural elements. An investigation conducted at the bridge approach of the Kuala Selangor Bridge revealed multiple weak zones characterized by relatively low Mackintosh probes' blow counts and minimal resistivity readings, indicative of highly compressible strata requiring immediate attention. Polyurethane (PU) foam/resin injection was implemented as a remedial measure to consolidate these weak zones and mitigate settlement. The efficacy of this ground improvement technique was assessed through comprehensive settlement monitoring programs. The case studies presented herein demonstrate that PU foam/resin injection exhibits adaptability in addressing differential settlement at abutment approaches, positioning it as a viable alternative among remedial solutions. There are several documented applications of polyurethane foam grout injection, including at the bridge approaches of the South Klang Valley Expressway (SKVE) at abutments 12A, 12B, 13A, 13B, and 11B; the PLUS Expressway at KM 88.78; Bridge BR1 (abutment A) and Bridge BR2 (abutment B) along Route FT92 towards Pusat Latihan Rekrut (PULAREK), as well as the Selat Lumut Bridge abutments A and B. Additionally, it has been applied at the culvert approaches for Route 1-46 and 1-47, between Simpang Kanowit and Simpang Batu 12 in Sibu, Sarawak.

However, it is imperative to thoroughly evaluate the requisite surcharge to counteract the buoyancy effect inherent to this lightweight material. The selection of an optimal ground improvement methodology is contingent upon the rigorous analysis of field investigation data, emphasizing the critical role of geotechnical characterization in infrastructure development.

Acknowledgements

The author gratefully acknowledges the Center of Excellence in Engineering and Technology (CREaTE), Public Works Department of Malaysia, for providing the research grant that facilitated the investigation and the development of the proposed geo-rehabilitation solution to mitigate settlement effects at bridge and culvert approaches. The author also extends sincere gratitude to Geocon (M) Sdn Bhd for their unwavering commitment and dedication to ensuring the solution is adaptable and applicable for addressing industrial challenges.

References

Buzzi, O., Fityus, S., Sasaki, Y. and Sloan, S. (2008). Structure and properties of expanding polyurethane foam in the context of foundation remediation in expansive soil. Mechanics of Materials, 40, 1012–1021.

Gary M. Gladysz, Krishnan K. Chawla, “Characteristic and Properties of Porous Materials”. Voids in Materials (Second Edition), 2021

Jabatan Mineral dan Geosains Malaysia (JMG). (n.d.). Portal Rasmi Jabatan Mineral dan Geosains Malaysia. https://www.jmg.gov.my/awam/penerbitan/katalog-peta

José, Ramón, Sánchez, Lavín., Félix, Escolano, Sánchez., Alberto, Mazariegos, de, la, Serna. (2018). Chemical Injections Realized with Null Pressure for Underpinning the Foundation of an 18th Century Building Located in the Historical City of Cuenca (Spain). Applied Sciences, 8(7):1117-. doi: 10.3390/APP8071117

Mohamed Jais I. B., Md. Ali, M A and Muhamad, H (2015). Alternative ground improvement solution with polyurethane foam/resin. Proceedings of the 3rd International Civil and Infrastructure Engineering Conference Kuala Lumpur, Malaysia. 425–440

Mohamed Jais, I.B. (2017). Rapid Remediation using Polyurethane Foam/ Resin Grout in Malaysia. Geotechnical Research, Volume 4 GR2, pp. 107-117.

Sidek, N., Mohamed, K., Jais, I. B. M., & Abu Bakar, I. A. “Strength Characteristics of Polyurethane (PU) With Modified Sand”. Applied Mechanics and Materials, 773–774, pp. 1508–1512, 2015.

Saha, A., Kundu, S.K. and Dey, A.K., 2019. Prediction of settlement of road embankment using electrical resistivity tomography (ERT). Conference of Urbanization Challenges in Emerging Economies.

Yu, L., Wang, R., & Skirrow, R. (2013). The Application on Polyurethane Grout in Roadway Settlement Issues. Geo Montreal.

Journal of Road Engineering Association of Asia and Australasia
Journal homepage: www.reaaa.net
JREAAA – 1(1) 2025: 20-24

Advanced Intelligent Heavy Vehicle Management System of National Freeway in Taiwan

LEU, Wen-Yuh[1,*], WU, Yuan-Chan [1], Chang, Tzu-Yun[1] & LIN, Hung-Gee[2]
*Corresponding author: lwy@freeway.gov.tw

[1] *Central Region Branch Office, Freeway Bureau, MOTC., No.55, Ln.5, Sec.4 Taiwan Boulevard, Taichung City 407026, Taiwan*
[2] *Department of Electrical Engineering, CECI Engineering Consultants, Inc., Taiwan. N.323 Yangguang St., Neihu Dist., Taipei City 114710, Taiwan*

ABSTRACT

Pavement damage caused by heavy vehicles in Taiwan's National Freeway system is a serious problem. Therefore, the Taiwan Freeway authorities implemented smart weigh-in-motion (WIM) to manage vehicles in early 2022. This paper presents the WIM system architecture, equipment, function, and communication transmission. Furthermore, integrated image recognition automatic vehicle identification (AVI) technology and electronic toll collection (e-Tag) are presented. The integrated technology application in identifying a vehicle's license number provides a correct message as a judgment of whether or not to weigh. The operation results show that the frequency of major pavement repairs is reduced, and 96.71% of vehicles do not need to enter the static weighbridge station. The operation performance for energy saving and carbon reduction is remarkable. For example, for the Southbound WIM system in Yuanlin of National Freeway, the average monthly savings were estimated at NT$ 1,669,263 in time costs, 127 litters in fuel consumption, and a reduction of 4,111 kilograms in CO_2 emissions in 2023.

ARTICLE INFO

Article History:
Received 1 Sep 2024
Received in revised form
17 Jan 2024
Accepted
01 Apr 2025
Available online
01 May 2025

Keywords:
weigh-in-motion
WIM
the integrated technology of AVI and e-Tag
weighbridge 3

1. Introduction

According to statistics from Taiwan's Ministry of Transportation, heavy vehicles account for approximately 14% of the total traffic on national highways. While these vehicles play a vital role in Taiwan's economic growth, the damage they cause to road surfaces cannot be overlooked. Reducing such damage has become a significant challenge for road management agencies worldwide. Establishing a heavy vehicle management system to control overloading is a viable solution.

Several initiatives are underway to install static weighbridge systems to monitor heavy vehicle loads. There are 44 static weighbridge stations across Taiwan's national highway system. While these stations effectively detect overloaded vehicles, they also contribute to traffic congestion on main lanes. Despite their designed capacity to handle around 200 vehicles per hour, the Ministry of Transportation data shows that nearly 800 heavy vehicles pass through these stations every hour. This high traffic volume decreases the operational efficiency of the weighbridge stations and heightens traffic risks. Studies indicate that although weighbridges are effective in detecting overloading, their efficiency heavily relies on maintaining lower traffic volumes.

Highway management units have introduced an advanced intelligent heavy vehicle management system known as the Weigh-in-Motion (WIM) system to address the issues of low efficiency and long queues at weighbridge stations. This system screens heavy vehicle loads directly on the main lanes. Overloaded vehicles are directed to weighbridge stations for further weighing, while non-overloaded vehicles can pass through without stopping.

The structure of this paper is described as follows: Section 2 presents the literature review. Section 3 introduces the architecture of the Weight-in-Motion system. Section 4 discusses the integration of image recognition technology. Section 5 introduces the practical operational, followed by Section 6 discusses its effectiveness. The final section provides conclusions.

2. Literature Review

The Weight-in-Motion (WIM) system is an advanced technology that measures vehicle weight while in motion. Indeed, the ASTM (E1318 – 09, 2009) describes WIM as measuring a moving vehicle's dynamic tyre forces and estimating the static vehicle's corresponding tyre loads. Unlike traditional static scales, WIM systems can swiftly and accurately measure vehicle weight without requiring vehicles to stop, thus minimizing disruptions to traffic flow. They also enable efficient weighing of vehicles in motion, significantly enhancing traffic operations, as Jacob et al. (2005) noted.

The WIM system can be classified into two types—off-line screening and mainline screening—based on its installation location. Off-line screening WIM systems are typically installed upstream of static weigh stations on highways to filter and screen potentially non-compliant vehicles. When using off-line screening WIM systems for vehicle weight enforcement, all passing vehicles are directed to the off-line lane, where their gross vehicle weight is measured dynamically, and their vehicle type is identified. The measured weight is then compared to the allowable gross weight for the respective vehicle type. If a vehicle is suspected of being overweight, roadside traffic signals direct it to proceed to a static weigh station for further verification. After weighing, the vehicle re-enters the highway via the off-line lane.

In contrast, mainline screening WIM systems are installed directly on highway mainlines. These systems also serve to filter and screen potentially overweight vehicles. WIM technology is also integrated with e-screening systems to filter overweight vehicles. The primary difference is that not all vehicles must enter an off-line lane. Instead, mainline WIM systems identify suspicious vehicles on the mainline and, through guidance systems, direct them to static weigh stations for confirmation. Vehicles not suspected of being overweight are allowed to continue without interruption.

The foundation of the WIM system lies in various sensing technologies, including piezoelectric sensors, fibre optic sensors, capacitive sensors, and strain gauge sensors. Piezoelectric sensors, known for their simple installation and low maintenance costs, are widely used on high-traffic roadways. Furthermore, McCall and Vodrazka (1997) highlight that multi-sensor fusion (MS-WIM) effectively reduces errors by integrating data from multiple sources.

In addition, a crucial factor affecting the WIM system is its accuracy. Current technology has achieved a tolerance of ±5% for gross vehicle weight and ±10% for axle weight, making the WIM system more suitable for law enforcement and traffic management. Jacob and Feypell-de La Beaumelle (2010) stated that WIM systems are superior to traditional static weighing systems because they reduce congestion, minimize manual operations, and provide greater long-term economic benefits. Studies have also shown that using WIM technology to monitor overloaded vehicles can reduce infrastructure damage. For example, real-time monitoring in Abu Dhabi has extended road life by 10% to 15% while reducing maintenance costs.

The WIM system can instantly detect overloaded vehicles and provide suspected violation data to police units for enforcement. The WIM system is then combined with a static scale to verify whether any overloading violations have occurred, greatly improving law enforcement efficiency. Jacob (2005) emphasized that automated WIM systems reduce human intervention and improve the transparency and credibility of law enforcement. In addition to law enforcement, WIM technology supports weight-based tolling systems, ensures fair tolling, and provides valuable data for transportation planning and infrastructure investment.

3. Advanced Intelligent Heavy Vehicle Management System

3.1. System Architecture

The intelligent heavy vehicle management system in Taiwan's National Freeway System includes 10 weighing stations, which WIM technology has adopted to manage heavy vehicles through mainline screening of freeways.

Figure 1 shows the operational process of the WIM system. This system comprises five parts of equipment, including weighing equipment (A), displaying equipment (B and C), checking equipment (D), and confirmation and photography equipment (E). In the initial stage, the weighing equipment not only determines the loading of heavy trucks using a pound bar but also obtains the license plate numbers through automatic vehicle identification (AVI). Subsequently, a logical comparison is used to determine whether the weight exceeds the approved loading. If it does not exceed the limit, the license plate number for exempted weighing will be shown on the display board (in stages B and C). However, if it exceeds the approved loading, the vehicle must undergo a static weighbridge station for further inspection (in stage D). In cases where trucks fail to follow the guidance and forcibly pass through, the photography equipment (in stage E) will be activated to enforce the heavy vehicle evading the weighing station.

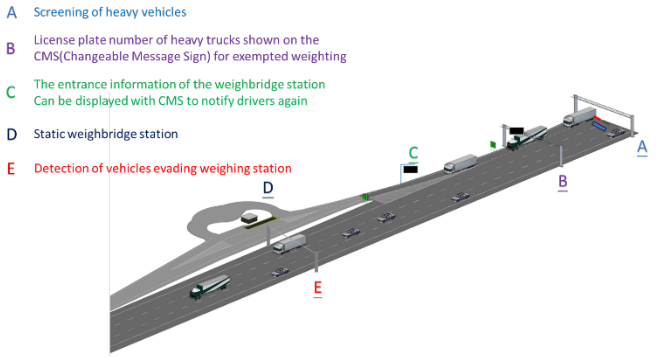

Figure 1: The system architecture of WIM.

3.2 System Equipment

The advanced intelligent heavy vehicle management system is based on Information and Communications Technology (ICT), which includes various information and communication technologies for communication and integration. With the vigorous development of ICT technology, important technological advancements stimulate innovation and practical applications in the ICT industry. Taiwan continuously explores ways to integrate and apply these technologies, especially in traffic management, particularly on freeways. In terms of information technology, the freeway traffic control system has established mature technologies in data collection, processing, storage, and cloud software applications. Communication technology includes self-built transmission networks and other equipment. Moreover, in response to the demands of heavy vehicle management for freeways, Taiwan has created, for the first time, a domestically developed WIM technology for use in the heavy vehicle management system, building upon the foundation of ICT technology on freeways.

The application of ICT technology in each WIM system involves integrating data and image detection, data and image transmission, information dissemination, and backend software operation. Its application is described as follows:

(1) The mainline screening WIM system comprises weighing sensors, automatic
(2) license plate recognition camera (AVI), electronic tag (e-Tag) detectors,
(3) closed-circuit television cameras (CCTV), changeable message signs (CMS), etc. The equipment layout is illustrated in Fig.2.

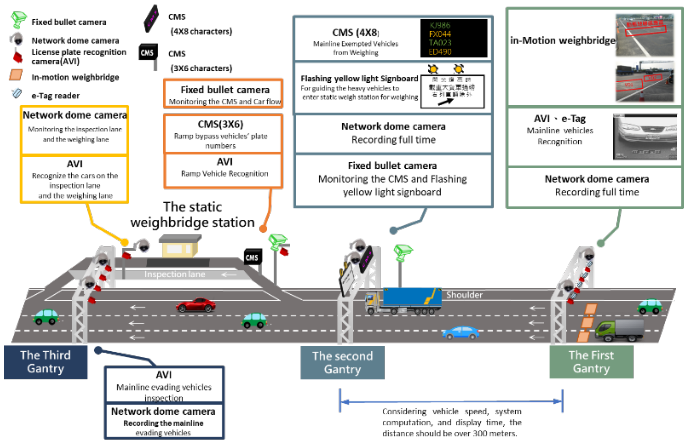

Figure 2: The equipment layout of WIN.

3.3 System Operation and Software of WIM

The operation of the weighing-in-motion system involves automatically screening vehicles suspected of overloading. For vehicles without suspicion of overloading, changeable message signs inform them to bypass the static weighbridge station for weighing. This system improves the efficiency of weighing heavy vehicles, thereby reducing congestion and severe accidents on the mainline of the national freeway caused by heavy vehicle queues over the onramp of the weighing stations.

The WIM system is equipped with three steel structure frames, and the overall operation process is illustrated in Fig. 3. The steps of the process are as follows:

(1) When a vehicle drives through the first gantry on the mainline of the national freeway, it is detected by vehicle detectors (VD), e-Tag detectors, automatic license plate recognition systems (AVI), and CCTV. Vehicle data can be obtained by the smart system, such as vehicle length, speed, lane of passage, e-Tag code, license plate number, and recorded panoramic photos of the front and body of the vehicle. Simultaneously, the in-motion weighing station collects data, such as vehicle type, length, axle weight, wheel weight, wheelbase, number of axles, and total weight. The front-end controller then transmits the data to the intelligent heavy vehicle management system at the weighing station.

(2) After receiving the vehicle information from the first gantry, the intelligent heavy vehicle management system compares the load data with the vehicle registration database. If the vehicle is checked to ensure it is not overloaded, the system transmits the vehicle number to the changeable message sign (CMS) at the second gantry. The CMS displays the vehicle's license plate number, which is exempted from entering the static weighbridge station, to inform the driver that they can bypass without entering the ramp to the static weighbridge station.

(3) At the entrance ramp of the static weighbridge station, an AVI system is installed to capture the license plate numbers of vehicles entering the weighing station. These license plate numbers are then transmitted to the intelligent heavy vehicle management system to double-check whether vehicles are exempted from weighing. Additionally, a 3 × 6-character CMS is installed to display again the license plate numbers of exempted heavy vehicles, informing drivers that they do not need to enter the static weighbridge station for weighing.

(4) The third gantry is equipped with an AVI system and CCTV. Similar to the previous gantries, it transmits data, such as the license plate number and front photos of the passing vehicles. These data are primarily used for the static weighbridge station to check whether the heavy vehicle is exempted from weighing or evading the weighing station.

(5) The inspection lane is equipped with an AVI system and CCTV, which receives data, such as the license plate number and front photos of passing vehicles, being immediately transmitted to the system. These data verify whether heavy vehicles should have entered the static weighbridge station but attempted to evade weighing.

(6) The intelligent heavy vehicle management system conducts enforcement checks on vehicles that attempt to evade weighing. It compares the vehicle data received from the third gantry and the inspection lane with the list of vehicles determined by the system to require weighing at the static weighbridge station. This comparison helps identify vehicles that attempted to evade weighing, enabling authorities to issue tickets and enforce penalties accordingly.

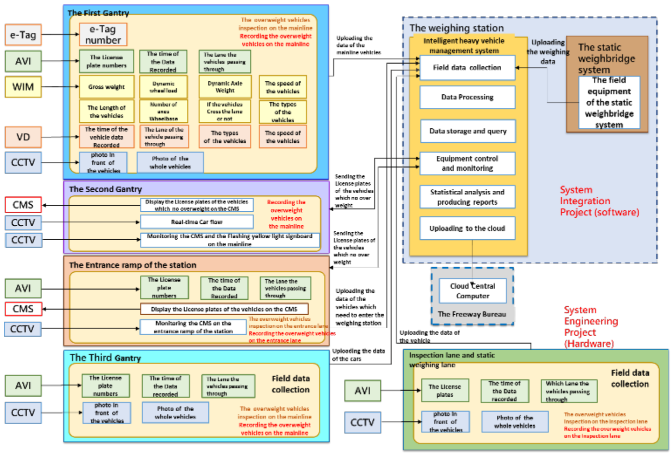

Figure 3: The process flow of WIN.

3.4 System Architecture of Communication Transmission

The weighing station (central end) is equipped with a high-speed Ethernet network switch, which connects to outdoor network switches at the field end via optical fibre cables. This setup enables the transmission of data collected or displayed by various devices at the field end to the intelligent heavy vehicle management platform at the central end.

The WIM system employs a circular redundant transmission architecture, as illustrated in Fig.4. In the event of network disconnection on one side, information can still be transmitted via the other side. Furthermore, the outdoor network switches at the field end feature Power over Ethernet (PoE) functionality, enabling them to provide power to the cameras through the network cables.

4. Integrated Technology of e-screening

In Taiwan, it's the first time an intelligent heavy vehicle management system has been developed. Although WIM systems are not a novel concept, their operation in Taiwan introduces new techniques and solutions, especially by integrating them with e-Tag barcodes installed on each heavy vehicle. This integration enhances the system's accuracy, primarily through the use of the innovative AI technology in license plate recognition equipment and the assistance of e-Tags.

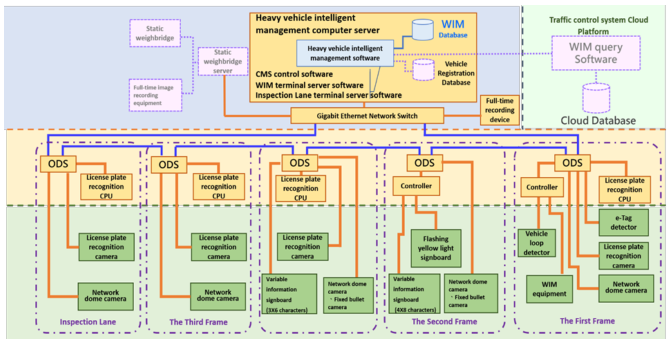

Figure 4: The architecture of communication transmission of WIN.

4.1 AI License Plate Recognition Technology

In the past, license plate recognition technology relied on binary algorithms, which were limited by various factors, such as poor lighting, insufficient illumination, high noise, special lighting conditions, sticker covering, overexposure, plate bending, and blurred images, resulting in poor image capture. However, with the adoption of AI algorithms, license plate recognition technology now leverages AI deep learning for image learning and correction. This advancement enables the system to maintain an accuracy of over 95%, even under adverse environmental conditions. Refer to the next page, Fig.5, for details.

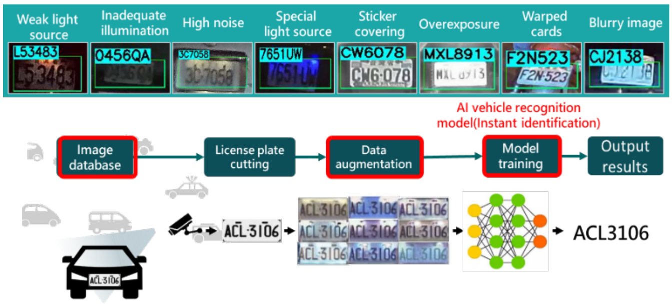

Figure 5: Image recognition of vehicle's license.

4.2 Assisted Recognition Technology of e-Tag

Due to the implementation of the electronic toll collection system (ETC), which enables mainline free-flowing traffic on Taiwan's freeways, every vehicle is equipped with an e-Tag barcode. Through the first gantry, equipped with an e-Tag detector, the e-Tag is matched and learned with the license plate recognition system. After multiple confirmations of matching, the license plate corresponding to the e-Tag is stored in the database.

Taiwan's ETC system has won several international awards from IBTTA, IRF, and ITS, such as IBTTA Toll Excellence Awards in Customer Service & Marketing Outreach category and President's Award, ITS World Congress Industry Award, IRF Global Road Achievement Award, Best PPP Project in Public Sector Category Awarded, and National Cloud Computing Awards in Service Applications Innovation category. Therefore, the ETS's e-Tag represents an innovative product technology.

As e-Tag is a unique code, the database can establish the correspondence between each heavy vehicle's license plate and its e-Tag code. Similar to the backup mechanism of the license plate recognition system, in which factors such as lighting, weather, or imaging failure affect license plate recognition, the system can compare the e-Tag's corresponding vehicle plate database and provide an immediate response. This detailed process is shown in Fig.6.

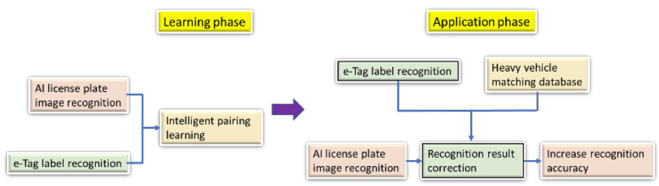

Figure 6: Integrated technology of AVI and e-Tag

5. Practical Operation Performance of WIM

This study sets appropriate threshold values to verify the weighbridge of WIM and AVI. In the part of the weighbridge, it verifies the load weight detection unit and compares the weight to the static weighbridge. Through three types of loaded heavy vehicles, namely U11 (front single axle, rear single axle), S112 (front single axle, rear single axle tractor with rear dual axle semitrailer), and S123 (front single axle, rear dual axle tractor with rear tri-axle semitrailer), are used to verify the load weight detection unit. The results indicate that measurement errors compared with the actual wheel, axle, and axle group load were <5%, <4%, and <0%, respectively. All results are below the specificity value that the measurement error between the total weight detected by the WIM weighbridge and the actual wheel load, axle load, and axle group load should be <5%.

In addition, the load weight detection unit of the vehicle passing through the WIM weighbridge is compared with the weight measured by the same vehicle passing through the static weighbridge station. Among 100 loaded vehicles passing through the static weighbridge station, more than 95 vehicles should have a total weight deviation of ±6%. The verification result is within 4%.

Furthermore, the verification of AVI includes the detected rate, recognition rate, correct recognition rate, and data integration accuracy rate. Its summary is shown in Table 1.

Table 1: The results of AVI verification.

Item	Specification	Results
Rate		
Vehicle Detection Rate	≧95%	98%
License Recognition Rate	≧85%	96% (bright) 92% (dark)
Correct Recognition Rate	≧90%	100% (bright) 98% (dark)
Accuracy Rate	≧90%	100% (bright) 98% (dark)

6. Discussion

Weigh-in-Motion (WIM) systems offer multifaceted advantages, addressing critical transportation infrastructure and safety challenges. Those are the issues of mitigating pavement damage, improving road safety, optimizing enforcement, and promoting energy efficiency. WIM systems are pivotal in managing heavy vehicles. Through real-time data and intelligent monitoring, WIM systems deter overloading, enhance compliance, and reduce maintenance and environmental costs, fostering smarter and more sustainable pavement quality.

Firstly, WIM systems effectively address the issue of overloaded vehicles, significantly reducing pavement and bridge maintenance costs. The design service life of a pavement depends on the accumulated standard single-axle load equivalent. When the actual load exceeds this estimate, the pavement reaches its terminal serviceability index, necessitating major rehabilitation. Severe overloading accelerates pavement deterioration, shortens service life, and increases maintenance expenses. These findings align with Jacob and Feypell-de La Beaumelle (2010).

Secondly, overloaded vehicles significantly affect manoeuvrability, increasing the risk of accidents, particularly rollovers during turns, due to a higher centre of gravity. Accidents involving heavy vehicles cause severe traffic disruptions and debris hazards. By integrating automatic vehicle recognition, WIM systems reduce the frequency of static weighbridge inspections, thereby lowering traffic conflicts. Data from the Northbound WIM system in Houli, Taichung City, show that 96.71% of vehicles bypass static weighbridges. Additionally, the average monthly evasion rate in 2023 was 0.29%, demonstrating improved compliance and enhancing freeway safety.

Thirdly, the adoption of WIM systems on Taiwan's freeways has revolutionized enforcement by combining real-time monitoring with automated detection. These systems function as preventive tools, reducing noncompliance. Monthly data show that over 80,000 vehicles are screened, with evasion rates dropping below 0.5%, compared to over 2% pre-implementation. Repeated violations by freight operators have decreased by 15% annually, reflecting improved compliance. These findings are consistent with Jacob and O'Brien (2005).

Finally, WIM systems contribute to energy savings and carbon reduction by reducing time costs, fuel consumption, and CO2 emissions. For instance, the Southbound WIM system in Yuanlin saved an estimated NT$1,669,263 in time costs, 127 litres of fuel, and 4,111 kilograms of CO2 emissions per month in 2023. Monthly and annual statistical reports (Figures 7 and 8) underscore these benefits. As WIM system implementation expands, further contributions to energy savings and carbon reduction are remarkable.

The WIM at the southbound Yuanlin station on National Freeway No. 1. Annual Benefit Analysis Report												
Year	Month	A. the number of vehicles passing during operational period	F. number of vehicles exempted from entering the static weighbridge station	C. number of vehicles suspected of being overweight requiring to entry into the static weighbridge station(=A-F)	G. actual number of vehicles complying with the exemption from entering the static weighbridge station	H. The compliance rate(G/F)	I. Time cost (hours) *note1	J. Time cost (in NT dollar) *note2	K. Fuel consumption (liters) *note3	L. Fuel cost (in NT dollar) *note4	M. CO2 emissions (kilograms) *note5	N. The proportion of heavy vehicles compliant with exemption from weighing (=G/A)
2022	Total for the entire year	635092	595948	93.84%	540644	90.72%	22226.48	11113237.78	10137.08	244303.51	27370.1	85.13%
2022	Monthly average	70566	66216	93.84%	60072	90.72%	2469.61	1234804.2	125.15	27144.83	3041.12	85.13%
2023	Total for the entire year	1124907	1077610	95.8%	974489	90.43%	40062.33	20031162.78	18271.67	440347.22	49333.51	86.63%
2023	Monthly average	93742	89801	95.8%	81207	90.43%	3338.53	1669263.56	126.89	36695.6	4111.13	86.63%
2024	Total for the entire year	273470	259407	94.86%	236849	91.3%	9737.13	4868562.78	4440.92	107026.14	11990.48	86.61%
2024	Monthly average	91157	86469	94.86%	78950	91.3%	3245.71	1622854.26	493.44	35675.38	3996.83	86.61%

*note：
1.I=G*(256 seconds) - 108 seconds) / 3600 seconds),From the 1st gantry to entering the weighbridge and leaving：256(sec),From the 1st gantry to the 3rd gantry: 108(sec)
2.J=I * 500 in NT dollar/hour, Hourly time cost: 500 yuan/hour
3.K=G * 0.15 kilometers / 8 kilometers per liter, Mileage saved for vehicles exempted from weighing: 0.15 kilometers, Distance traveled per liter: 8 kilometers per liter
4.L=K * 24.1 in NT dollar,Cost per liter of fuel: 24.1 yuan/liter
5.M=K * 2.7 kilograms,CO2 emissions per liter: 2.7 kilograms/liter

Figure 7: Yearly report of energy saving and carbon reduction.

The WIM at the southbound Yuanlin station on National Freeway No. 1. Monthly Benefit Analysis Report												
Year	Month	A. the number of vehicles passing during operational period	F. number of vehicles exempted from entering the static weighbridge station	C. number of vehicles suspected of being overweight requiring to entry into the static weighbridge station(=A-F)	G. actual number of vehicles complying with the exemption from entering the static weighbridge station	H. The compliance rate(G/F)	I.Time cost (hours) *note1	J.Time cost (in NT dollar) *note2	K.Fuel consumption (liters) *note3	L.Fuel cost (in NT dollar) *note4	M.CO2 emissions (kilograms) *note5	N.The proportion of heavy vehicles compliant with exemption from weighing (=G/A)
111	4	67988	60587	89.11%	54096	89.29%	2223.95	1111973.33	1014.3	24444.63	2738.61	79.57%
111	5	122221	114199	93.44%	106247	93.04%	4367.93	2183966.11	1992.13	48010.36	5378.75	86.93%
111	6	24549	23074	93.99%	19928	86.37%	819.26	409631.11	373.65	9004.97	1008.86	81.18%
111	7	512	459	89.65%	459	100%	18.87	9435	8.61	207.41	23.24	89.65%
111	8	90940	84447	92.86%	77157	91.37%	3172.01	1586005	1446.69	34865.32	3906.07	84.84%
111	9	66564	63390	95.23%	57146	90.15%	2349.34	1174667.78	1071.49	25822.85	2893.02	85.85%
111	10	59186	56684	95.77%	50980	89.94%	2095.84	1047922.22	955.88	23036.59	2580.86	86.14%
111	11	103801	99416	95.78%	89831	90.36%	3693.05	1846526.11	1684.33	40592.38	4547.69	86.54%
111	12	99331	93692	94.32%	84800	90.51%	3486.22	1743111.11	1590	38319	4293	85.37%
112	1	76967	72482	94.17%	65627	90.54%	2698	1348999.44	1230.51	29655.2	3322.37	85.27%
112	2	67575	64435	95.35%	58874	91.37%	2420.38	1210187.78	1103.89	26603.69	2980.5	87.12%
112	3	112466	108171	96.18%	98835	91.37%	4063.22	2031608.33	1853.16	44661.07	5003.52	87.88%
112	4	77353	74128	95.83%	67854	91.54%	2789.55	1394776.67	1272.26	30661.53	3435.11	87.72%
112	5	102973	99679	96.8%	90240	90.53%	3709.87	1854933.33	1692	40777.2	4568.4	87.63%
112	6	158498	153339	96.75%	138471	90.3%	5692.7	2846348.33	2596.33	62571.58	7010.09	87.36%
112	7	91433	88279	96.55%	80573	91.27%	3312.45	1656222.78	1510.74	36408.92	4079.01	88.12%
112	8	90220	86254	95.6%	78022	90.46%	3207.57	1603785.56	1462.91	35256.19	3949.86	86.48%
112	9	88936	84994	95.57%	75914	89.32%	3120.91	1560454.44	1423.39	34303.64	3843.15	85.36%
112	10	70457	66980	95.07%	60095	89.72%	2470.57	1235286.11	1126.78	27155.43	3042.31	85.29%
112	11	99678	94825	95.13%	84673	89.29%	3481	1740500.56	1587.62	38261.61	4286.57	84.95%
112	12	88351	84044	95.13%	75311	89.61%	3096.12	1548059.44	1412.08	34031.16	3812.62	85.24%
113	1	94031	87757	93.33%	78993	90.01%	3247.49	1623745	1481.12	35694.96	3999.02	84.01%
113	2	63641	60801	95.54%	56036	92.16%	2303.7	1151851.11	1050.68	25321.27	2836.82	88.05%
113	3	115798	110849	95.73%	101820	91.85%	4185.93	2092966.67	1909.13	46009.91	5154.64	87.93%
總計		2033469	1932965	95.06%	1751982	90.64%	72025.93	36012963.32	32849.68	791676.9	88694.09	86.16%

*note：
1.I=G*(256 seconds) - 108 seconds) / 3600 seconds),From the 1st gantry to entering the weighbridge and leaving：256(sec),From the 1st gantry to the 3rd gantry: 108(sec)
2.J=I * 500 NT dollar/hour, Hourly time cost: 500 yuan/hour
3.K=G * 0.15 kilometers / 8 kilometers per liter, Mileage saved for vehicles exempted from weighing: 0.15 kilometers, Distance traveled per liter: 8 kilometers per liter
4.L=K * 24.1 NT dollar,Cost per liter of fuel: 24.1 yuan/liter
5.M=K * 2.7 kilograms,CO2 emissions per liter: 2.7 kilograms/liter

Figure 8: Monthly report of energy saving and carbon reduction.

7. Conclusions

This paper presents the system architecture, equipment, function of WIM, and communication transmission. Furthermore, the integrated technology of image recognition automatic vehicle identification (AVI) and electronic toll collection (e-Tag) are presented. The integrated technology application in identifying a vehicle's license number provides a correct message as a judgment of whether or not to weigh.

The operation results show that the frequency of major pavement repairs is reduced, and 96.71% of vehicles don't need to enter the static weighbridge station. This indicates an improvement in the behaviour of heavy vehicle drivers and dramatically promotes the safety of the freeway. The operation performance for energy saving and carbon reduction is remarkable. For example, for the Southbound WIM system in Yuanlin, of National Freeway, the average monthly savings were estimated at NT$ 1,669,263 in time costs, 127 litters in fuel consumption, and a reduction of 4,111 kilograms in CO2 emissions in 2023.

However, WIM systems still face some challenges and limitations, so a comprehensive evaluation should be done for further application. WIM systems' accuracy still needs to be confirmed due to dynamic road conditions, environmental factors, and irregular vehicle movement, particularly under adverse climatic or road surface conditions. Additionally, the cost of initial installation and calibration and the durability of sensors under heavy traffic loads pose financial and operational limitations. Regulatory and standardization gaps further complicate consistent enforcement.

To fully realize the benefits of WIM technology, these challenges must be addressed through continuous research and development. Improvements in dynamic algorithms, sensor durability, and calibration techniques, combined with robust standards and regulatory frameworks, are also essential.

Acknowledgements

We sincerely thank Engineer Shih-Wei Hsu of CECI Engineering Consultants, Inc., for his invaluable contributions and dedicated efforts while implementing the weigh-in-motion (WIM) system. We also extend our gratitude to everyone who provided guidance and support throughout this project.

References

ASTM E1318-09. (2009). "Standard Specification for Highway Weigh-in-Motion (WIM) Systems." ASTM International.

Bernard Jacob et al., "Weigh-in-Motion for Direct Enforcement of Overloaded Commercial Vehicles," Transportation Research Procedia, 2016.

Bernard Jacob & Véronique Feypell-de La Beaumelle, "Improving Truck Safety: Potential of Weigh-In-Motion Technology," IATSS Research, 2010.

Caprani, C. C., & González, A. (2010). "Long-Term WIM Data Analysis for Bridge Assessment." Journal of Bridge Engineering.

Jacob, B., & O'Brien, E. J. (2005). "Weight-in-Motion of Road Vehicles: Final Report." Transportation Research Laboratory.

McCall, B., & Vodrazka, W. C. (1997). "WIM Systems and Their Use in Traffic Data Collection and Enforcement." Federal Highway Administration.

Journal of Road Engineering Association of Asia and Australasia

Journal homepage: www.reaaa.net
JREAA – 1/2025: 25-31

OPEN ACCESS

Detecting Lateral Offset Distance on Rural Road in Thailand by Using Point Cloud Data: A Case Study

Nutvara Jantarathaneewat[1], Chenxi Liu[2], Shucheng Zhang[1] & Yinhai Wang[1,*]
*Corresponding author: yinhai@uw.edu

[1]*Department of Civil and Environmental Engineering, University of Washington, Seattle, USA*
[2]*Department of Civil and Environmental Engineering, University of Utah, Utah, USA*

ABSTRACT

The lateral offset distance refers to the horizontal clearance as an essential buffer for vehicle operation. Illegal permanent and temporary obstacles along roadsides, such as privately owned signs or building expansions, can obstruct visibility and increase the risk of collisions. Traditionally, road agencies have relied on manual inspections to estimate these distances, a time-consuming and often inaccurate process. This study introduces an automatic process for determining lateral offset distance using point cloud data to overcome these challenges. Approximately 10 kilometres of point cloud data were collected from rural roadways in Thailand using a Mobile Laser Scanning system. Clustering algorithms, specifically RANSAC and DBSCAN, were employed to identify road lines and walls within the point cloud data and calculate the lateral offset distance. The dataset encompasses a variety of road characteristics, including residential areas, high-traffic volume roads, and roads along rivers. Mean Absolute Error (MAE) was used to measure the accuracy of this algorithm by comparing the automated results to manual detection. The algorithm demonstrated the highest accuracy for high-traffic volume roads, achieving an MAE of 0.343 meters per kilometre. The study also reported average lateral offset distances across the different road classes, with roads along the river having the widest average lateral distance at 10.787 meters and residential roads having the shortest average lateral distance at 4.911 meters. Suggestions for further improvements to the algorithm were also provided based on these findings.

ARTICLE INFO

Article History:
Received 20 Sep 2024
Received in revised form
20 Jan 2025
Accepted
01 Apr 2025
Available online
01 May 2025

Keywords:
Point Cloud Data
LiDAR
Rural Roads

1. Introduction

Roadside features have significant impacts on transportation safety. In 2022, approximately 20% of motor vehicle crash fatalities occurred when vehicles left the roadway and collided with fixed objects on the roadside, such as trees, utility poles, and traffic barriers (Insurance Institute for Highway Safety, 2022). Research (Lee & Mannering, 2002) reveals that the severity of these accidents is significantly impacted by the lateral offset distance (e.g., road shoulder width). The lateral offset distance refers to the horizontal clearance that provides a buffer for vehicle operation. According to the AASHTO Green Book (AASHTO, 2018), a minimum horizontal clearance of 18 inches to objects behind curbs is the standard offset that allows for normal traffic operations. However, it is acknowledged that providing such a clearance may not always be feasible in low-speed curbed areas due to right-of-way constraints and other practical limitations of the built environment (FHWA, 2023).

Many countries and regions like Thailand, mainly rural areas, often suffer from limited horizontal clearance due to illegal permanent and temporary obstacles along roadsides, such as privately owned signs or building expansions (Figure 1). Based on the latest five-year accident records (2019-2023) reported in the Accident Report Management System (ARMS) from the Department of Rural Roads of Thailand, run-off-road (ROR) crashes were the leading type of accident. They resulted in the highest number of fatalities (DRR, 2024). This type of crash accounted for 37% of the collisions (2,291 cases) and caused 632 deaths over the five years. In Thailand, fixed roadside objects such as trees, electrical poles, and kilometre posts were identified as significant roadside hazards (Se et al., 2020; Somchainuck et al., 2013).

Therefore, a 'Forgiving Roadside' concept was introduced over a decade ago to emphasize the importance of designing safer roadsides that allow vehicles to traverse a verge with gentle gradients safely and free of hazardous ground profiles and objects (iRAP, 2022). To mitigate the severity of ROR accidents, Highway setback guidelines set up the minimum lateral clearance distance to provide clear zones free of obstructions and dangerous roadside conditions (Lorenz, 2019). The recent research (Road Safety Thailand Road Safety Policy Foundation, 2018) highlighted the policy's performance in removing or relocating roadside fixed objects to safer roads. However, road agencies still relied on physical inspections to manually estimate this distance, often using public light poles as reference points. This manual measurement is time-consuming with low accuracy, highlighting the demand for technologies for a more efficient, accurate, and economical measurement.

Therefore, since 2014, the Department of Rural Roads (DRR) has developed the Rural Road Network Management (RM) System. The RM system employs Mobile Mapping System (MMS) technology for image processing, capturing detailed images of road assets and locations. The MMS system is equipped with various sensors, including dual antenna GNSS for precise heading determination and wide-angle cameras, aiming to reduce the need for onsite surveying by staff and replace it with high-quality data (Bamrungwong et al., 2017). In 2019, DRR enhanced the RM system by incorporating laser scanning technology to generate 3D point cloud data for high-accuracy object detection. Therefore, this research aims to take advantage of the 3D point cloud data collected in the program and develop an innovative automated processing system for horizontal clearance distance measurement for transportation safety enhancement. This study's contributions are:

- **Automated Calculation of Lateral Offset Distance:** The research introduces lateral offset distance measurement innovation through 3D point cloud data, eliminating manual physical inspections.
- **Comprehensive Dataset:** Approximately 10 kilometres of point cloud data were collected from rural roadways in Thailand, covering residential areas, high-traffic volume roads, and roads along the river.
- **Support for Right-of-Way Inspections:** Offers valuable data for right-of-way inspections and supplementary roadside improvements, helping to address issues with visibility and collision risks due to illegal obstacles along roadsides.

The proposed system is structured into six main steps. Firstly, the point cloud data is preprocessed to remove noise, enhancing subsequent processes' efficiency and accuracy. Next, the point cloud is separated into ground and non-ground points to improve the effectiveness of object detection tasks. Following this, edge line detection and wall detection are performed separately. Clustering algorithms are employed in these tasks: Density-Based Spatial Clustering of Applications with Noise (DBSCAN) is used to fit point cloud data to lines for edge detection, while RANdom Sample Consensus (RANSAC) is applied to fit point cloud data to planes for identifying wall configurations. Once these objects are detected, the system calculates the distance between them. Manual measurements are taken using point cloud processing software to validate the results, and the Mean Absolute Error (MAE) is used as the metric for accuracy assessment. Approximately 10 kilometres of point cloud data were collected from rural roadways in Thailand and used as a dataset for developing and testing the detection algorithm.

Figure 1: Illegal permanent and temporary obstacles along the roadside. (Google Street View, 2024)

2. Literature Review

Object detection using point cloud data has been extensively utilized in various industries, most notably autonomous vehicles. Meanwhile, it also approaches for creating asset inventory. For instance, point cloud data has been primarily employed for automatic traffic sign detection by analyzing parameters such as retro-intensity, elevation, and hit count (Ai & Tsai, 2012). Ai's study concluded that certain constraints, including retro-reflectivity and the height of objects, need to be adjusted to eliminate false negative detections.

Point clouds collected from Mobile Laser Scanning (MLS) have demonstrated their utility in detecting both on-road and off-road objects. On-road objects include road surfaces, road markings, driving lines, and road cracks, while off-road objects encompass pole-like structures such as traffic signs, light poles, trees, and power lines (Ma et al., 2018). Learning-based point cloud processing algorithms, particularly those employing machine learning techniques, have become prevalent in existing studies. For instance, random forests have been utilized for urban road environment classification, demonstrating the capability to extract various objects beyond traditional road assets, including buildings, trash cans, and vegetation (Mohamed et al., 2022). Despite their effectiveness, there is a need for larger-scale studies to thoroughly evaluate the efficiency and scalability of these methods. In addition, these methods often rely on the prior knowledge of human operators, which poses significant challenges, especially in complex urban environments.

In addition to clustering and machine learning techniques, neural networks have been extensively utilized for point cloud object detection. One notable neural network architecture is PointNet, a unified framework designed for various applications, including object classification, part segmentation, and scene semantic parsing (Qi et al., 2016). PointNet++ was developed, enhancing PointNet by incorporating hierarchical feature learning, which allows it to recognize fine-grained details and local patterns more effectively (Qi et al., 2017). Numerous studies have applied PointNet and PointNet++ for object detection in transportation. These techniques have proven effective in detecting various roadside infrastructures such as poles, traffic signs, light poles, trees, and power lines. For instance, Balado et al. (2019) and Wang et al. (2019) demonstrated the successful application of PointNet++ in identifying and classifying roadside objects, thereby contributing to the development of detailed and accurate infrastructure inventories. However, one major challenge is the requirement for extensive annotations to train the neural networks effectively. Annotating large datasets is labour-intensive and time-consuming, posing widespread implementation bottlenecks. Additionally, the high computational resources needed for training and deploying these deep neural networks can be prohibitive, especially for large-scale deployments.

To address the limitations of large annotated datasets and high computational requirements, this study focuses on clustering methods that are efficient and scalable. Techniques such as RANSAC (Random Sample Consensus) and DBSCAN (Density-Based Spatial Clustering of Applications with Noise) have been successfully applied to extract road boundaries and pole-like objects from point cloud data (Yin & Zhu, 2022; Gouda et al., 2022). These methods effectively handle noisy data and identify distinct geometric structures. For example, a previous study utilized DBSCAN to identify bridge structures and determine vertical clearance (Gargoum et al., 2018). However, the focus of that study was vertical clearance, whereas we aim to determine horizontal clearance distances.

A concept of lateral distance calculation was presented in a study on point cloud classification for detecting roadside safety attributes and distances (Zhong et al., 2019). This study utilized a comprehensive approach where roadside objects were first detected and labelled by leveraging both point-wise and grid-wise features. The identified objects were then used to calculate the distance to the attribute centre, providing precise measurements for roadside safety analysis. Another study proposed a voxel-based raycasting method to assess roadside clearance parameters on rural highways (Gouda et al., 2022). While comprehensive, their approach included multiple object types and focused on side clearance distances, unlike our targeted focus on wall detection.

Our study aims to simplify this method by combining RANSAC and DBSCAN clustering methods for detecting walls and road edges, addressing existing research gaps. While DBSCAN is widely recognized for road surface detection, RANSAC has not been extensively applied for wall detection. We employ clustering methods to ensure the object detection process is efficient and scalable. This approach allows us to handle large datasets with minimal computational resources and reduces the reliance on extensive annotations.

3. Methods

Figure 2 shows the workflow for the system. The algorithm was implemented using two different libraries on separate workstations. The environment for working with Point Cloud Library (PCL) (Rusu & Cousins, 2011) was set up on a system equipped with an AMD Ryzen 9 5900HX CPU. The environment for working with python-pcl (Sirokujira, 2018) was set up on a system equipped with an Intel Core i9-7900X CPU running Ubuntu 18.04.

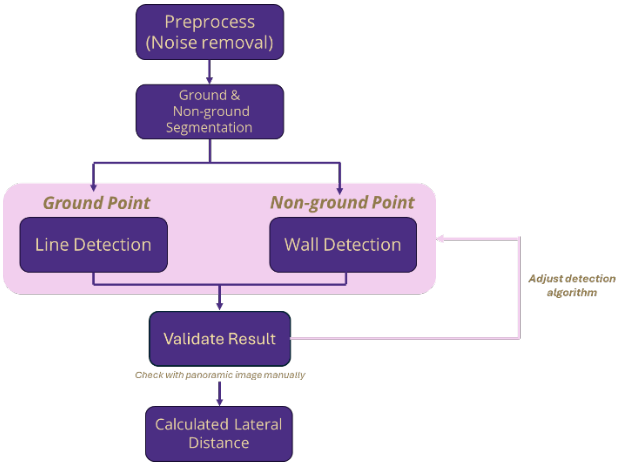

Figure 2: Workflow for a system.

3.1. Preprocessing

Point clouds are considered large datasets that provide accurate and robust information but may contain high-density noise and scattered distributions due to being acquired by scanning equipment. Preprocessing processes can address these issues by reducing noise and the amount of data to process. Techniques for preprocessing point cloud data include point filtering, removing outliers, and holding out some data to decrease the size of raw data (Kharroubi, 2023).

This study employed a downsampling technique to remove noise during preprocessing (Point Cloud Library, 2020). This method not only cleans the data but also reduces the size of the point cloud, resulting in more efficient analysis. Specifically, the VoxelGrid class in Point Cloud Library was used to create a 3D voxel grid over the input point cloud data. Each voxel represents a 3D cube with a fixed size, and all points are reduced (i.e., downsampled) by their centroid. For this study, a voxel grid leaf size of 1 cm was set, which successfully reduced the point cloud size by 50% while retaining the original shape, as shown in Figure 3. This efficient reduction in data size without significant loss of detail is crucial for further processing and analysis.

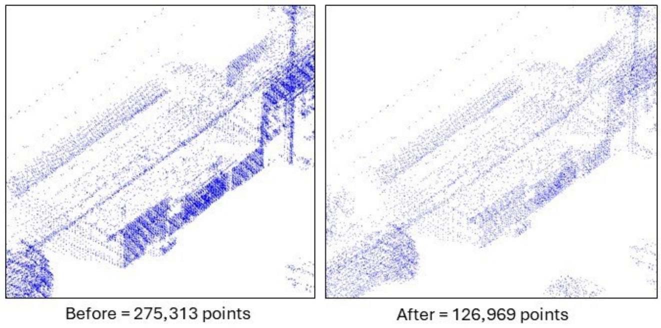

Figure 3: Applying Downsampling Method for Preprocessing. (Leaf Size = 1 cm)

3.2. Ground Separation

To reduce computation time and increase object detection accuracy, it is essential to separate ground and non-ground objects (Figure 4). This study employed a filtering method known as the Cloth Simulation Filter (CSF) for this purpose (Zhang W, 2016). The CSF method simulates cloth using 3D computer graphics algorithms to cover an inverted LiDAR point cloud. The upside-down LiDAR terrain is assumed to be rigid, and the shape of the cloth, which drops due to gravity, forms the digital terrain model (DTM). The cloth's interaction and the corresponding LiDAR points determine the ground surface.

In order to customize this method to the particular data we are working with, the Cloth Simulation Filter (CSF) enables users to adjust parameters based on their own needs. The first parameter is cloth resolution, which determines the grid size of the cloth used to cover the terrain; a larger cloth resolution results in a coarser Digital Terrain Model (DTM). The second parameter is max iteration, which specifies the maximum number of terrain simulation iterations. Lastly, the classification threshold defines the threshold for classifying the original point cloud into ground and non-ground parts based on the distances between the original point cloud and the simulated terrain. This study used the default values for all parameters: 0.5 for cloth resolution, 500 for max iteration, and 0.5 for the classification threshold. These settings were chosen to balance accuracy and efficiency in the ground Separation process.

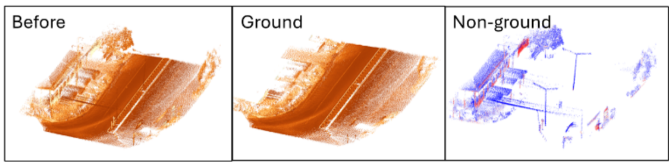

Figure 4: Applying Cloth Simulation Filtering (CSF) for ground and non-ground segmentation

3.3. Line Detection

The road pavement marking contains an outstanding intensity value. Therefore, we will utilize it. To prepare the data for the clustering algorithm, the separated ground point cloud is filtered based on intensity values before proceeding to the next step. In this study, an intensity range of 40 to 999 was set to ensure that the retained point cloud does not include pavement, which comprises most data in the ground point cloud.

Afterwards, this study employed the Density-Based Spatial Clustering of Applications with Noise (DBSCAN) method, which is well-known for its ability to detect clusters of various shapes and sizes, making it suitable for identifying road alignments. Previous studies have utilized DBSCAN to process point cloud data for clustering tasks (Wang, W. and Wang, F., 2018; PointCloud Slam Image Web3, 2024; Peng et al., 2020). Generally, DBSCAN requires two parameters:

- ***eps:*** This is the maximum distance between two points for them to be considered part of the same neighbourhood. In this study, the default value of 0.5 was used.
- ***min_points*:** This is the minimum number of points required to form a dense region, also known as the minimum cluster size. The default value of 5 was used in this study.

This study utilizes the python-pcl library to process the point cloud data and uses the sklearn library, a machine learning library, for applying DBSCAN clustering. Each road segment will be fitted to a line using polynomial regression. Different degrees of polynomials were examined to determine the best match. The equation is illustrated in Eq. 1.

$$y = \beta_0 + \beta_1 x + \beta_2 x^2 + \cdots + \beta_n x^n \quad (1)$$

Where y = Dependent variable
x = Independent variables
n = Degree of a polynomial
β = Coefficient

This study chose a second-degree polynomial as it provided the best fit. To enhance the accuracy of data fitting, the point cloud data were divided into multiple segments, resulting in smaller straight lines (Figure 5).

3.4. Wall Detection

Plane segmentation of a set of points is used for wall detection. Plana surface is estimated using the RANdom Sample Consensus (RANSAC) algorithm to fit the point clouds in the plane model, as shown in Eq. 2.

$$ax + by + cz + d = 0 \quad (2)$$

Where x, y, z = Point cloud coordination
a, b, c = The x, y, z coordinate of the plane's normal (normalized)
d = The fourth Hessian component of the plane's equation

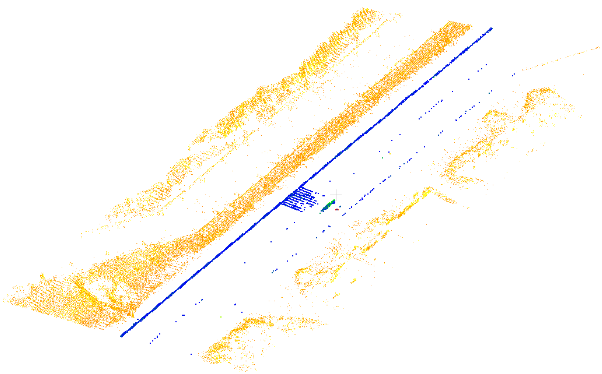

Figure 5: Segmented line detection from point cloud on the ground.

The RANdom Sample Consensus (RANSAC) technique was initially employed to identify the most significant plane, which corresponds to wall object. RANSAC (Random Sample Consensus) is an iterative method used to estimate a model from data that includes outliers (Fischler & Bolles, 1981). It works by repeatedly selecting random subsets of data, fitting linear models to these subsets, and identifying the model that best fits the inliers, thereby excluding outliers. The model with the best fit, based on the inliers, is chosen as the final result.

A distance threshold must determine the maximum distance from the model to a potential inlier point for RANSAC to function effectively. Table 1 presents the various thresholds tested on a point cloud of approximately 120,000 points. We found that a threshold of 0.250 meters is the most suitable for our data, as it yields a reasonable number of clusters that represent planes in the point cloud. The maximum number of iterations was set to 1,000 by default.

After obtaining the plane from the RANSAC algorithm, the next step is determining if the plane represents a wall. A plane that represents a wall should be perpendicular to the x-y plane or parallel with the z-plane. Surface normals are used to determine the plane's configuration. Surface normals are vectors perpendicular to a surface at a given point and are essential properties of a geometric surface.

Table 1: Distance Threshold for RANSAC Algorithm tested on 120k Point Cloud Data

Distance Threshold (m)	Number of Plane Cluster	Details
1.00	2	Too coarse, unable to distinguish wall object
0.50	4	Too coarse, unable to distinguish wall object
0.25	**7**	**Suitable for distinguishing wall object**
0.10	16	Able to detect wall object
0.01	184	Unable to distinguish object shape as it is too small

Determining the normal at a specific point on the surface is approximated by estimating the normal of a plane tangent to the surface. This estimation is typically done using the surrounding point neighbourhood, known as the k-neighbourhood. The correct scale factor (k or radius) for determining the nearest neighbours of a point is crucial for accurate normal estimation. In the point cloud library, selecting the appropriate k or radius (r) values is critical for identifying the nearest neighbours effectively.

The scale for determining a point's neighbourhood should be selected based on the level of detail required by the application. Table 2 presents various search radius tested on a point cloud of approximately 20,000 points, representing the target object of a wall. We found that a radius of 0.30 meters is the most suitable for our data, as it perfectly distinguishes the orientation of the object.

Table 2: Search Radius for Surface Normal Estimation on 20k Point Cloud Data

Search Radius (m)	Details Plane Cluster
3.00	Unable to detect normal on any plane
1.00	Works best with large planes
0.50	No improvement from the previous step
0.30	**Able to capture planes representing walls of any size**
0.20	Unable to compile results, terminated
0.03	Unable to compile results, terminated

In this study, a wall object is identified by high coefficients of the normal vector in the x and y directions, indicating that the segment is perpendicular to the x-y plane and represents a wall configuration (Figure 6). Conversely, if the object has low coefficients in both the x and y directions, it can be concluded that the object is parallel to the x-y plane, meaning it does not represent a wall.

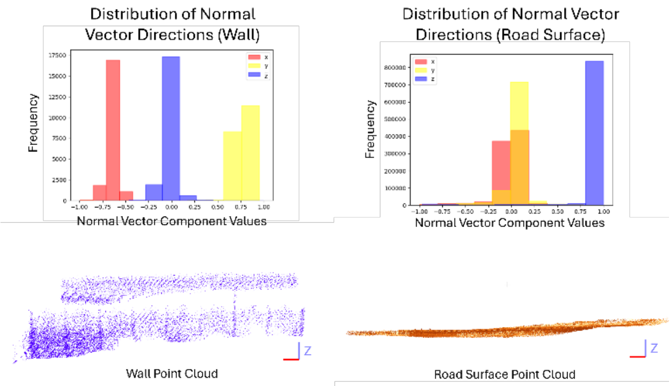

Figure 6: Histogram of surface normal for wall (Left) and road surface (Right).

3.5. Distance Calculation

The distance will be calculated by determining the distance between the borderline and the wall. This study utilized the pcl_sample_consensus library, which includes Sample Consensus (SAC) methods such as RANSAC and models like planes and cylinders. SAC methods like RANSAC help robustly fit models to the point cloud data, even in noise and outliers. The library also provides functions for computing the distance from a point to a plane. The centroid of the segmented road line is used as the reference point for the calculation. This centroid represents the central position of the road line and serves as a critical point for accurate distance measurement. The detected wall is treated as a plane, defined by equation 2 (Figure 7).

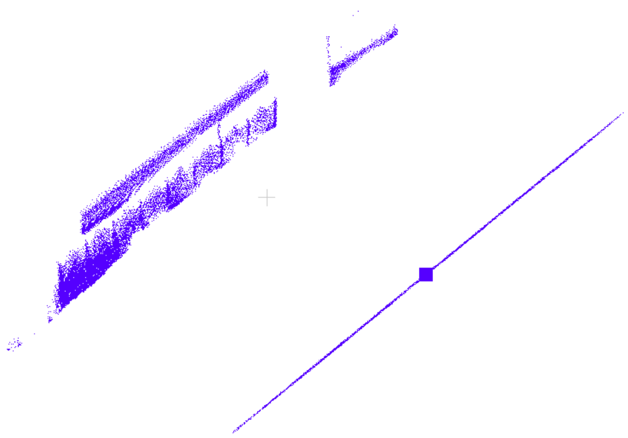

Figure 7: Point to plane distance

Given that the edge line of the road is used as the reference, it is essential to determine which side the wall is located on. To achieve this, the direction of the vehicle's trajectory during the data collection process is utilized. The trajectory provides context about the vehicle's position relative to the road's edge line. It helps identify whether the wall or object is on the same side as the vehicle or on the opposite side. If the wall is located on the opposite side of the road lane from the vehicle's trajectory, the detected distance must be adjusted to account for the lane's width. This adjustment involves subtracting the width of the road lane, which, for a two-lane road, is typically assumed to be 6 meters. This step is crucial to ensure that the calculated distances accurately reflect the spatial relationships between the road and roadside objects.

3.6. Validation

To assess the proposed algorithm's accuracy and effectiveness, we compared the algorithm's detection results and manually detected distances. For the manual detection process, we utilized CloudCompare, an open-source 3D point cloud and mesh processing software (CloudCompare, 2024). CloudCompare provides tools for precise measurement and validation of distances within point cloud data, but it requires manual intervention to identify and specify objects (Figure 8). This approach allowed us to comprehensively evaluate the algorithm's performance and ensure its reliability.

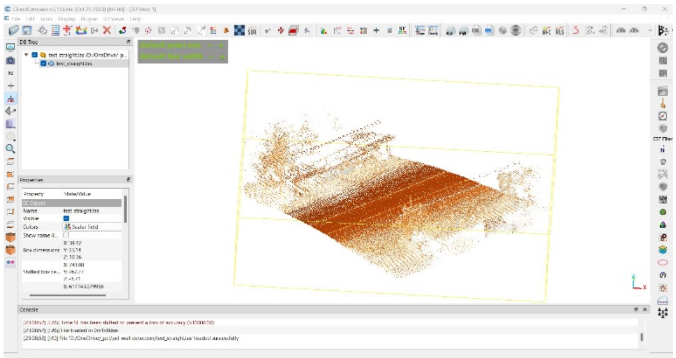

Figure 8: CloudCompare Software

Mean Absolute Error (MAE) is selected as the measurement metric for this study, as it provides a clear and straightforward assessment of the algorithm's prediction accuracy. MAE calculates the average absolute difference between the distances detected by the algorithm and the ground truth values measured manually using CloudCompare. By focusing on absolute differences, MAE ensures that the magnitude of errors is accounted for without considering their direction, whether the detected distance is overestimated or underestimated. The equation for calculating MAE for n instances is in equation 3.

$$MAE = \frac{1}{n}\sum_{i=1}^{n}|distance_i - groundtruth_i| \qquad (3)$$

In this equation, $distance_i$ represents the distance calculated by the algorithm for the i-th instance, and $groundtruth_i$ represents the corresponding ground truth distance measured using CloudCompare. We used MAE for this dataset because the presence of outliers is not particularly significant. The setting of the wall is random and does not correlate with specific road classes, meaning that outliers can appear anywhere without a specific pattern. Therefore, MAE, which provides a straightforward average error without disproportionately penalizing larger deviations, is a more appropriate metric for evaluating the accuracy of our distance calculations.

To conduct a thorough analysis, the point cloud data obtained from mobile laser scanning was divided into subsegments, each with a length of approximately 10 meters. This segmentation approach facilitates a more manageable and detailed examination of the data, ensuring that each segment can be analyzed individually for specific characteristics and anomalies. We specifically tested only those subsegments where walls were identified. This targeted approach ensures that the analysis is relevant and focused on the areas of interest, providing insights into the algorithm's performance in detecting and measuring walls accurately. To ensure a fair comparison of the accuracy of different observations, especially considering the varying lengths of the segments, we normalized the error by computing the Mean Absolute Error (MAE) per kilometre.

4. Results

This study proposes an algorithm for automatically calculating lateral distance using point cloud data obtained from mobile laser scanning. The point cloud data were preprocessed to remove noise and separate ground from non-ground points, enhancing the algorithm's efficiency. The road edge line and wall were detected separately, and the distance between these two objects was then computed. CloudCompare software was used to validate the detected results manually. The generalizability of the algorithm was tested using three distinct scenarios, each representing different road characteristics: a road along the river, a road in a residential area, and a high-volume road. These scenarios were chosen because they present unique features and challenges, offering a diverse basis for evaluating the algorithm's performance.

This study used 10 kilometres of point cloud data collected through mobile laser scanning. The road along the river scenario offers insights into how proximity to natural features affects lateral distance calculations. The residential area scenario highlights the complexities introduced by varying building densities, pedestrian pathways, and local signs. Finally, the high-volume road scenario showcases the algorithm's capability to handle dense traffic conditions and multiple lanes.

Table 3 presents a comprehensive performance analysis of the algorithm across different road environments. Table 4 displays the measured and calculated lateral distances used for validation, with panoramic images included for reference. Each row represents a different test scenario, illustrating the algorithm's performance in various contexts.

Table 3: Performance analysis of the algorithm

Class	Road Name	Total length (km)	MAE (m)	MAE per km (m/km)	Average lateral distance (m)
Residential	CNT1021	2.91	1.635	0.562	4.911
Road along river	AYA2045	1.95	1.301	0.667	10.787
High Traffic Volume	AYA5042	5.12	1.758	0.343	5.406

5. Discussion

Among the three categories analyzed, roads in high-traffic volume areas exhibit the lowest Mean Absolute Error (MAE) per kilometre of 0.343, demonstrating the effectiveness of our method in these environments. In contrast, roads along the river and residential areas have higher MAE per kilometre values of 0.667 and 0.562, respectively. During manual detection, we observed that high-traffic volume areas typically have clearer roadsides to accommodate the heavy traffic. Conversely, our algorithm performed well on straight-road segments but showed weaknesses on curved segments. Some subsegments had road surfaces covered by vegetation or were under maintenance, which impeded our model's ability to detect road lines accurately. Roads with multiple lanes also require human interpretation, as our current algorithm cannot precisely detect outer lines. In terms of wall detection, large flat planes yielded higher accuracy. Walls covered by vegetation or not continuous, such as fences, often resulted in errors. Awnings and roofs, which are commonly found along roads in residential areas, led to shorter lateral distances due to plane fitting during wall detection. Additionally, pruned shrubs often created planar surfaces that the algorithm mistakenly detected as walls.

Another objective of this study is to report the average lateral distance across different road classes. The analysis revealed that roads along the river have the widest average lateral distance at 10.787 meters, while roads in residential areas have the shortest average lateral distance at 4.911 meters. This finding is consistent with expectations for residential areas, where space is often maximized and infrastructure is densely packed. Additionally, temporary roadside structures like curbside stores frequently violate legal limitations and can skew measurements. In contrast, along river roads, natural barriers and the need to mitigate risks like landslides typically result in constructions being placed further from the riverbank, which increases the average lateral distance. However, temporary structures can still be detected along these roads, though they generally do not significantly impact the average distance. This variation in lateral distances highlights the influence of environmental and infrastructural factors on road design and safety considerations.

Table 4: Measured and calculated lateral distances with panoramic images for road in residential area (Top), road along rivers (Middle), and roads with high traffic volume (Bottom)

Measured lateral distances	Panoramic image
Class: Residential 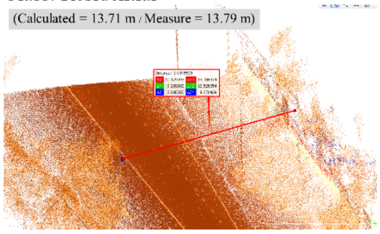	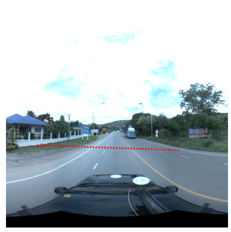
Class: Road along river 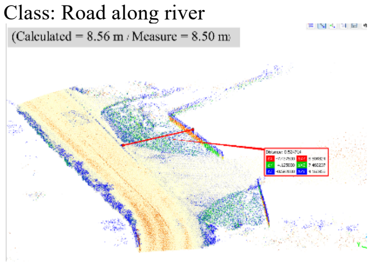	
Class: High Traffic Volume 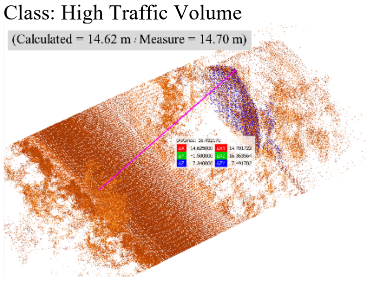	

Comparing our results to previous studies adds context to the findings. For example, Zhong et al. (2019) used object centre approximation techniques to calculate lateral distances, achieving average error distances of 0.10 and 0.50 meters for pole and tree detection, respectively, based on 20 samples per object. Our method achieves comparable MAE values (0.34 to 0.67 meters) while focusing on wall detection across diverse road environments. Furthermore, in comparison to Gouda et al. (2021), who used a ratio-based method to evaluate roadside clearance distances with a detection rate of 97%, our method achieves similar detection accuracy for wall detection and lateral distance calculation. These comparisons illustrate that our approach holds promise and aligns with existing methodologies in terms of performance.

Nevertheless, this study does present some limitations. The total dataset covers only approximately 10 kilometres of roadways. While this provides a starting point, it may not be sufficient to generalize the findings across different road types and conditions. Expanding the dataset to include a broader variety of road types, such as urban roads, highways, and rural roads with different characteristics, would allow for a more comprehensive evaluation. The proposed algorithm also showed limitations in detecting curved lines or fences, indicating areas for further refinement and improvement. These factors suggest that while the study provides valuable insights, additional research with a more diverse dataset and enhanced algorithm capabilities is necessary to fully validate and extend the findings.

6. Conclusion

This study introduces an automated methodology for calculating lateral offset distance using point cloud data. Approximately 10 kilometres of point cloud data were collected from rural roadways in Thailand and used as a dataset for developing a detection algorithm. Three road classifications were selected to analyze different road types comprehensively. Our developed algorithms achieved an MAE per kilometre of 0.343 meters for roads with high traffic volumes, as these roads typically have clear roadsides that align with their intended function. We also found that roads in residential areas have the shortest average lateral distance of 4.911 meters. The calculated lateral distance provides valuable data that road authorities can directly use for safety assessments and infrastructure planning.

Infrastructure along rural roads in Thailand, both temporary and permanent, is often random and challenging to detect through pattern recognition. To improve the algorithm, it is recommended to utilize deep learning techniques for object detection to better obtain semantic descriptions and make accurate classifications. Additionally, as road markings are sometimes missing due to obstructions or maintenance, implementing road marking detection will provide a more accurate and comprehensive assessment of all components on the road surface, reducing many of the assumptions made in this study.

Acknowledgements

The authors thank the Department of Rural Roads of Thailand and the Ministry of Transportation for using their data.

References

Ai, C., and Tsai, Y. J. (2012). Critical Assessment of Automatic Traffic Sign Detection Using Three-Dimensional LiDAR Point Cloud Data. Transportation Research Board 91st Annual Meeting. Volume: 12-3214.

American Association of State Highway and Transportation Officials, AASHTO. (2018). A Policy on Geometric Design of Highways and Streets, 2018. Green book, American Association of State Highway and Transportation Officials.

Balado, J., Martínez-Sánchez, J., Arias, P., & Novo, A. (2019). Road Environment Semantic Segmentation with Deep Learning from MLS Point Cloud Data. Sensors, 19(16). doi:10.3390/s19163466

Bamrungwong, C., P. Soparat, K. Saiprasertkit, and N. Jantarathaneewat. (2017). A Study of Applying Mobile Mapping Result for Road Safety Audit on Rural Roads in Thailand. Transportation Research Circular, , No. E-C220.

CloudCompare. (2024). CloudCompare: 3D point cloud and mesh processing software Open 2 Source Project. https://www.cloudcompare.org/. Accessed 2024.

Department of Rural Roads of Thailand (DRR). (2024). The Accident Report Management System (ARMS). https://arms.drr.go.th/. Accessed 2024.

FHWA Highway Safety Programs (2023). Clear Zones. https://highways.dot.gov/safety/rwd/provide-safe-recovery/clear-zones/clear-zones. Accessed 2023.

Fischler, M. A. and R. C. Bolles. (1981). Random sample consensus: a paradigm for model fitting with applications to image analysis and automated cartography. Vol. 24, No. 6, p.381–395.

Gargoum, S. A., L. Karsten, K. El-Basyouny, and J. C. Koch. (2018). Automated assessment of vertical clearance on highways scanned using mobile LiDAR technology. Automation in Construction, Vol. 95, pp. 260–274.

Gouda, M., Shalkamy, A., Li, X., and El-Basyouny, K. (2022). Fully Automated Algorithm for Light Pole Detection and Mapping in Rural Highway Environment Using Mobile Light Detection and Ranging Point Clouds. Transportation Research Record, 2676(7), 617-629. https://doi.org/10.1177/03611981221082531

Insurance Institute for Highway Safety (IIHS). (2024). Fatality Facts 2022: Collisions with fixed objects and animals. https://www.iihs.org/topics/fatality-statistics/detail/collisions-with-fixed-objects-and-animals. Accessed 2024.

iRAP. (2022). Forgiving Roads Concept. https://toolkit.irap.org/safer-road-treatments/forgiving-roads-concept/. Accessed 2024.

Kharroubi, A. (2023). Introduction to 3D Point Cloud. 3D Point Cloud Masterclass. Udemy.

Lee, J. and F. Mannering. (2002) Impact of roadside features on the frequency and severity of run-off-roadway accidents: an empirical analysis. Accident Analysis Prevention, Vol. 34, No. 2, pp. 149–161.

Lorenz Partners. (2019). Basic Conditions for Building Construction in Thailand. https://www.lorenz-partners.com/wp-content/uploads/2019/01/NL221E-Basic-Conditions-for-Building-Construction-in-Thailand-Jan19. pdf, accessed 2024.

Ma, L., Ying L., Jonathan L., Cheng W., Ruisheng W., and Michael A. C. (2018). Mobile Laser Scanned Point-Clouds for Road Object Detection and Extraction: A Review. Remote Sensing 10, no. 10: 1531. https://doi.org/10.3390/rs10101531

Mohamed, M., Morsy, S., and El-Shazly, A. (2022). Improvement of 3D LiDAR point cloud classification of urban road environment based on random forest classifier. Geocarto International, 37(27), 15604–15626. https://doi.org/10.1080/10106049.2022.2102218

Peng, C. L., Z. and L. Wang. (2020). Point cloud segmentation (clustering). https://yzrobot.github.io/mobile_robotics/P20-UN56-clustering.pdf. Accessed 2024.

Point Cloud Library. (2020). Downsampling a PointCloud using a VoxelGrid filter. https://pcl.readthedocs.io/projects/tutorials/en/latest/voxel_grid.html. Accessed 2024.

Point Cloud Slam Image Web3. (2024). Implementation of DBSCAN clustering algorithm based on PCL. https://medium.com/point-cloud-python-matlab-plus/implementation-of-dbscan-clustering-algorithm. Accessed 2024.

Qi, C. R., Su, H., Mo, K., & Guibas, L. J. (2016). PointNet: Deep Learning on Point Sets for 3D Classification and Segmentation. CoRR, abs/1612.00593. http://arxiv.org/abs/1612.00593

Qi, C. R., Yi, L., Su, H., & Guibas, L. J. (2017). PointNet++: Deep Hierarchical Feature Learning on Point Sets in a Metric Space. CoRR, abs/1706.02413. http://arxiv.org/abs/1706.02413

Road Safety Thailand Road Safety Policy Foundation. (2018). KEY FACTS ON ROAD SAFETY SITUATIONS IN THAILAND 2012-2013. https://www.roadsafetythai.org/edoc/doc_20181208173742.pdf. Accessed 2024.

Rusu, R. B. and S. Cousins. (2011). 3D is here: Point Cloud Library (PCL). In IEEE International Conference on Robotics and Automation (ICRA), Shanghai, China, 2011.

Se, C., T. Champahom, S. Jomnonkwao, and V. Ratanavaraha (2020). Risk factors affecting driver severity of single-vehicle run off road crash for Thailand highway. Engineering Journal,Vol. 24, No. 5, pp. 207–216.

Sirokujira. (2018). python-pcl. https://github.com/Sirokujira/python-pcl?tab=readme-ov-file#readme. Accessed 2023.

Somchainuck, O., P. Taneerananon, and S. Jaritngam. (2013). An in-depth investigation of roadside crashes on Thai National Highways. Engineering Journal, Vol. 17, No. 2, pp.63–74.

Wang, D., Wang, J., Scaioni, M., & Si, Q. (2019). Coarse-to-Fine Classification of Road Infrastructure Elements from Mobile Point Clouds Using Symmetric Ensemble Point Network and Euclidean Cluster Extraction. Sensors (Basel, Switzerland), 20(1), 225. https://doi.org/10.3390/s20010225

Wang, W. and F. Wang. (2018). lane-detection. Retrieved from: https://github.com/willshw/ 37 lane-detection. Accessed 2023.

Yin, S., and Zhu, L. (2022). Country Road Boundaries Detection for Autonomous Driving Based on LiDAR Point Cloud. 2022 IEEE 5th International Conference on Electronics Technology (ICET), Chengdu, China, 2022, pp. 1117-1120, doi: 10.1109/ICET55676.2022.9824682.

Zhang W, Q. J. (2016). An Easy-to-Use Airborne LiDAR Data Filtering Method Based on Cloth Simulation. Remote Sensing, 8(6):501.

Zhong, M., Verma, B., & Affirm, J. (2019). Point Cloud Classification for Detecting Roadside Safety Attributes and Distances. 2019 IEEE Symposium Series on Computational Intelligence (SSCI), 1078–1084. doi:10.1109/SSCI44817.2019.9002813

Journal of Road Engineering Association of Asia and Australasia

Journal homepage: www.reaaa.net

JREAA – 1/2025: 32-37

OPEN ACCESS

Adapting the Macroscopic Fundamental Diagram for Motorcycle-Dependent Cities: A Case Study of Cần Thơ City, Vietnam

Siti Raudhatul Fadilah[1], Hiroaki Nishiuchi[2,*] & An Minh Ngoc[3]

*Corresponding author: nishiuchi.hiroaki@kochi-tech.ac.jp

[1]*Graduate School of Engineering, Kochi University of Technology, Kami City, Kochi 782-8502, Japan*

[2]*School of Systems Engineering, Kochi University of Technology, Kami City, Kochi 782-8502, Japan*

[3]*Research Organization of Science and Technology, Ritsumeikan University, Kusatsu City, Shiga 525-0058, Japan*

ABSTRACT

Motorcycle-dependent regions, such as Cần Thơ City, Vietnam, present unique traffic dynamics that traditional homogeneous vehicle models fail to capture. This study focuses on Ninh Kiều District to explore and adapt traffic flow analysis for such mixed, non-lane-based environments. The primary aim is to refine the Macroscopic Fundamental Diagram (MFD) to better represent motorcycle-dominated traffic by integrating motorcycle equivalent units (MEU) and area occupancy into the standard framework. This adapted MFD provides a more accurate representation of traffic flow and concentration, addressing the challenges of conventional density-based models in mixed traffic conditions. This refined approach not only fills a notable research gap but also enhances the reliability of traffic analysis. By modifying the MFD, the study offers valuable insights into network performance, revealing key operational behaviours and potential bottlenecks in motorcycle-centric traffic networks. The findings underscore the utility of the adapted MFD as a tool for effective congestion management and operational efficiency in motorcycle-heavy regions, highlighting its broader applicability to similar settings.

ARTICLE INFO

Article History:
Received 20 Sep 2024
Received in revised form
20 Jan 2025
Accepted
01 Apr 2025
Available online
01 May 2025

Keywords:
Mixed traffic
Motorcycle-dependent traffic
Macroscopic fundamental diagram

1. Introduction

Traffic analysis traditionally hinges on the homogeneity assumption, expecting predictable movements and similar-sized vehicles adhering to lane discipline. However, this paradigm proves inadequate for motorcycle-dependent regions, such as Vietnam—the focus of this study—where motorcycles make up about 86% of all vehicles, marking the highest rate of motorcycle ownership globally (Tonko & Gidwani, 2018). These challenges to conventional traffic models are set against a backdrop of such regions, characterized by lower income, high-density land use, and a predominance of motorcycles (Minh et al., 2007). As M. and Verma (2016) pointed out, traffic models and theories designed toward homogeneous traffic fall short in these settings, prompting the need for tailored approaches.

Adding to this complexity is the concerning reality of traffic safety in such regions. Reports indicate that motorcycle-related crashes account for a significant share of road traffic accidents (Robbins & Fotios, 2020), exacerbated by the non-lane-based, mixed traffic dynamics. Understanding traffic flow in these environments is a critical step toward improving overall road safety and network efficiency, underscoring the necessity of developing enhanced traffic flow modelling approaches.

Herein lies the significance of the Macroscopic Fundamental Diagram (MFD)—an analytical construct that correlates vehicle volume with the rate of reaching destinations within a network. The MFD serves as a tool to assess traffic conditions and pinpoint areas for improvement. Initially proposed by Daganzo (2007), the MFD is widely recognized for its capability to model traffic on a broad scale. However, its application to mixed traffic remains scarcely examined, particularly in regions dominated by motorcycles.

This study aims to adapt the standard MFD to represent better the unique dynamics of mixed, non-lane-based traffic in motorcycle-heavy environments, such as Cần Thơ, Vietnam, where motorcycles frequently deviate from strict lane adherence, unlike their four-wheeled counterparts. By enhancing the applicability and utility of the MFD framework, the study seeks to improve traffic flow analysis and network-level performance assessments in such environments.

The remainder is organized: Section 2 provides a literature review setting the theoretical framework. Section 3 outlines the methodology, followed by Section 4 on traffic micro-simulation modelling, and Section 5 presents a refinement of the MFD. Finally, the paper concludes in Section 6 with a summary of the findings.

2. Literature Review

2.1. Mixed Traffic

Mixed traffic environments are characterized by the coexistence of multiple vehicle types, creating a complex traffic flow markedly different from homogeneous traffic conditions, where similar vehicles exhibit predictable patterns. M. and Verma (2016) describe these heterogeneous conditions as arising from various vehicle types with differing static and dynamic characteristics sharing the same road space. In such conditions, smaller, more agile vehicles like motorcycles can adeptly manoeuvre through tight spaces and rapidly adjust their trajectories and speeds quickly, often bypassing larger, slower-moving vehicles. This ability to exploit smaller gaps significantly alters vehicle flow dynamics and interaction patterns. Furthermore, the variability in driver behaviour, vehicle size, and the general lack of strict lane discipline, common in many urban areas, especially in developing countries, contribute to the complexity of managing mixed traffic.

2.2. Challenges in Applying Homogeneous Models to Mixed Traffic

In regions where motorcycles dominate the roads, mixed traffic conditions pose some challenges for traffic modelling. The literature underscores the limitations of conventional homogeneous traffic models when applied to such contexts, as highlighted by Khan and Maini (1999). Their review advocated for models tailored to account for the intricate aspects of mixed traffic, such as vehicle interactions, driver behaviours, and road configurations. It also noted the dynamic nature of motorcycles, particularly their ability to navigate congested roads by exploiting gaps and adjusting speeds. It stresses the importance of developing analytical frameworks to accommodate the diverse behaviours in these environments.

The critique extends to the use of Passenger Car Units (PCU) for modelling traffic conditions in India, as discussed by Chandra and Sikdar (2000) and Chandra and Kumar (2003). Their approach, while innovative, has been noted for not fully capturing the complexities of mixed traffic, especially in areas heavily trafficked by motorcycles. As traffic composition fluctuates, the effectiveness of PCUs varies, often failing to represent the distinct mobility characteristics of motorcycles, as observed by Arasan et al. (2008). This issue was further underscored by Kov and Yai (2010) in their study on Phnom Penh traffic, where motorcycles made up 70% of traffic. They noted that PCU metrics lose relevance in areas where light vehicles constitute less than 25% of the traffic mix, as the increase in light vehicles tends to reduce overall speeds and capacity, thereby impacting motorcycles' manoeuvrability and lateral positioning. Tan et al. (2018) observed similar challenges in Vietnam, where the low car-to-motorcycle ratio complicates traffic modelling using PCUs.

Another significant challenge is the measurement of traffic concentration. In mixed traffic systems, traditional density metrics, which count the number of vehicles per unit length per lane, fail to capture the true dynamics of the road. Unlike homogeneous environments with similar vehicle sizes and strict lane discipline, mixed traffic involves more complex spatial dynamics. As Lee (2007) notes, in motorcycle-heavy traffic, interactions are longitudinal and lateral, with motorcycles often filtering, weaving, and maintaining shorter headways. This behaviour, which allows multiple vehicles to occupy the same lane space simultaneously, is not typically observed in car-dominated traffic and complicates traditional traffic analyses by challenging the effectiveness of standard density measurements.

2.3. Macroscopic Fundamental Diagram (MFD)

The MFD marks a significant leap in traffic studies, mapping the relationship between traffic flow and density, to network performance. Initially introduced by Daganzo (2007) and expanded by Geroliminis and Daganzo (2007, 2008), the MFD extends the scope of the fundamental diagram from individual road segments to an aggregated network. A well-defined MFD emerges in contexts with relatively uniform congestion levels (Geroliminis & Daganzo, 2007), showing that average flow increases with rising density up to a critical point, indicative of the peak sustainable flow rate (Knoop et al., 2014). Beyond this threshold, the network experiences congestion, potentially leading to gridlock as density rises.

The shape and stability of the MFD are influenced by a wide array of factors, such as network structure (Ambühl et al., 2018), route preferences (Geroliminis & Daganzo, 2008), inhomogeneity in traffic distribution (Ambühl et al., 2018), traffic management strategies (Ambühl et al., 2018), and periods (Knoop et al., 2014). The MFD quantifies network conditions by correlating trip production—the number of vehicles—with vehicle accumulation—the rate at which vehicles reach destinations (Geroliminis & Daganzo, 2008). The peak of trip production rate (q_{MFD}) signifies the network's capacity, whereas the corresponding accumulation (k_{MFD}) denotes critical. It calculates the parameters by weighing the link flow (q_i) and density (k_i) of each link i by its length (l_i), reflecting aggregate traffic states, as shown in Equations (1) and (2) by Geroliminis and Daganzo (2008).

$$q_{MFD} = \frac{\sum_i q_i \cdot l_i}{\sum_i l_i} \tag{1}$$

$$\mathrm{k_{MFD}} = \frac{\sum_\mathrm{i} \mathrm{k_i} \cdot \mathrm{l_i}}{\sum_\mathrm{i} \mathrm{l_i}} \tag{2}$$

Despite the chaotic traffic conditions prevalent in Southeast Asian countries, there is a notable gap in network performance analyses. A pertinent study by Suwanno et al. (2021) assessed the impact of floods on traffic in Bangkok's Sukhumvit District using the MFD. The study analyzed weekday taxi movements and excluded freeway data using 2019 Thailand open data (i.e., vehicle and mobile probe data). Although it provided insights into how flood levels and network operations shape the MFD, the study did not consider the mixed traffic conditions crucial in Thailand, where motorcycles constitute about 87% of traffic (Tonko & Gidwani, 2018), an oversight that compromises the reliability of the findings.

3. Methodology

3.1. Workflow

To enhance the understanding of mixed traffic in motorcycle-dependent regions, this study follows a systematic flowchart depicted in Figure 1, employing AIMSUN Next 23 software to model and simulate traffic dynamics in Ninh Kiều District.

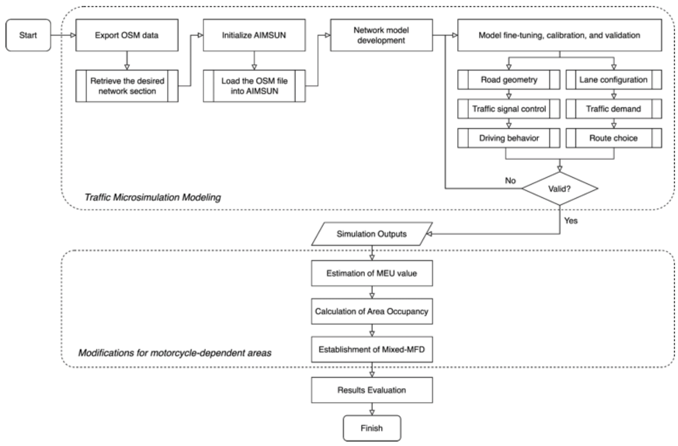

Figure 1: Methodological framework for simulation modelling and analysis.

2.2. Case Study

Cần Thơ City, situated in southern Vietnam, is the third most populous city with approximately 1.25 million residents, spread over an area of 331,212 km² with a density of 870 individuals/km² (Vietnam General Statistics Office, 2022). Motorcycles are the primary mode of transport, comprising 80–85%, with cars and taxis accounting for 7–10%. The study specifically targets Ninh Kiều District due to its high population density and significant traffic volumes among all districts in the city, making it a focal point of the study.

This research leverages secondary and primary data to investigate traffic patterns in the district. Primary data was gathered on March 2, 2024, through field observations that recorded traffic signal timing and phase configurations at 27 intersections in Ninh Kiều District. On March 2, 2024, a survey gathered empirical data on signal cycles and timings at 27 intersections in Ninh Kiều District. Most of these intersections operate with two and four signal phases; the busier ones employ four phases to accommodate extended green times for left turns, per Vietnam's right-hand driving rules. Meanwhile, secondary data encompasses traffic counts from 12 key intersections recorded from February 24–26, 2020, complemented by a seven-day activity diary survey engaging 5,841 participants. The survey documented the purpose of each trip, with details on the mode of transportation, distance, speed, and trip duration. Analysis of these data showed that motorcycles were the primary mode of transportation, accounting for 87.84% of the 11,465 recorded trips. Other modes included cars (1.57%), walking (5.00%), bicycles (5.40%), and other modes (0.19%). For analytical purposes, each journey entry was treated as a separate trip, irrespective of multiple daily trips by individuals. These data sources are integrated to construct calibrated origin-destination matrices, as summarized in Figure 2. The analysis identifies trends in Ninh Kiều District, with Monday emerging as the peak traffic volume day.

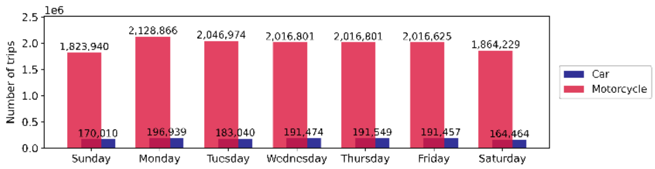

Figure 2: Daily traffic volume comparison by vehicle type.

4. Development of Traffic Microsimulation Model

Figure 3 displays the simulation model for Ninh Kiều District, leveraging geographic configurations from OpenStreetMap. Further adjustments are made to reflect actual geometries, converting the map into a simulated environment where links, nodes, and zones correspond to road segments, intersections, trip origins, and destinations.

Figure 3: AIMSUN traffic simulation model.

Although AIMSUN provides default parameters, customizing these to mirror the specific traits of the case study is essential. This process entails a rigorous calibration, adjusting simulation parameters iteratively to align closely with empirical data. Special emphasis is placed on calibrating behavioural models that account for cognitive processes in route selection, which is especially important in motorcycle-dependent settings. First, the calibration process begins by refining network configurations, modifying road segments and intersections, and integrating traffic signal control schemes. Subsequently, traffic demand calibration utilizes secondary data to form origin-destination matrices, as summarized in Figure 4.

AIMSUN enhances these efforts by incorporating dynamic traffic assignment models, which are crucial for handling time-variant flows and route choices. It integrates stochastic route choice and dynamic user equilibrium algorithms, fine-tuned to reflect the routing decision process and adapt to current traffic conditions. The final phase of the calibration process emphasizes driver behaviour, explicitly targeting the non-lane-based and aggressive driving patterns prevalent among motorcycle riders, as shown in Figure 5. Turn parameters were also modified to describe their gap acceptance behaviour at unsignalized intersections, contrasting with the more cautious driving styles typically observed in developed countries.

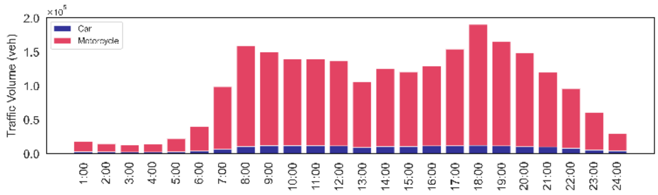

Figure 4: Hourly distribution of traffic demand.

Figure 5: Field observations of traffic conditions.

In essence, the efficacy of a simulation model depends on its capability to replicate observed conditions. Model validation entails a trial-and-error calibration process, comparing simulated outcomes to actual behaviours to identify and rectify discrepancies. This study conducts validation at the network level by examining aggregate flow across different spatial and temporal contexts, quantified using GEH statistics. Detailed in Equation (3), the GEH formula calculates deviations where m represents the model's hourly traffic volume, and o is the real-world count. GEH thresholds classify model accuracy as follows: values below 5 indicate a well-calibrated model; between 5 and 10 suggest potential errors requiring further investigation; and values above 10 necessitate recalibration or model rejection.

$$GEH = \sqrt{\frac{2(m-o)^2}{(m+o)}} \tag{3}$$

Table 1 presents validation indicators, including speed, total traffic volume, relative differences, and GEH values. With all GEH below 5, the model is deemed statistically validated, affirming its reliability in representing traffic in Ninh Kiều District.

Table 1: Validation of the overall network simulation against empirical data.

Indicators	Observed	Simulated	Relative Difference	GEH
Mean speed - cars (km/h)	23.97	25.26	5.38%	0.26
Mean speed - mc (km/h)	24.19	24.39	0.83%	0.04
Throughput - cars (veh)	35,837	36,120	0.79%	1.49
Throughput - mc (veh)	350,415	353,373	0.84%	4.99

5. Macroscopic Evaluation for Mixed Traffic

5.1. Adaptation for Motorcycle-Heavy Traffic: The MEU Approach

The analysis of mixed traffic necessitates a specialized approach, leading to the development of the Motorcycle Equivalent Unit (MEU), an evolution from the PCUs. Using motorcycles as the baseline, it assesses the relative speed and spatial occupancy of different transportation modes. Building upon the PCU calculation method by Chandra and Kumar (2003), further refined by Minh et al. (2005), this study utilizes Equation (4) to compute MEU_{car}, where V_{mc} and V_{pc} represent the mean speeds of motorcycles and cars, respectively, while A_{mc} and A_{pc} denote their projected rectangular areas on the road.

$$MEU_{car} = \frac{V_{mc} \,/\, V_{pc}}{A_{mc} \,/\, A_{pc}} \tag{4}$$

MEU computations consider the mean stream speed crucial in heterogeneous traffic, where speed consistency is absent. Traditional speed measurements like spot speed or space mean speed are unsuitable due to speed disparities between vehicle types. To overcome this, Cao et al. (2009) introduced an adjusted formula that better computes the mean stream speed (V_m), reflecting the collective mobility of mixed traffic flows. This is represented by Equation (5), which calculates a weighted average that accounts for the speed of each vehicle type k (v_k) and the quantity of each type (n_k), across all vehicle categories in the traffic stream (N).

$$V_m = \frac{\sum_{k=1}^{N} n_k \cdot v_k}{\sum_{k=1}^{N} n_k} \tag{5}$$

To further refine the model and represent the variability of speeds, Equation (6) is employed. This Equation calculates the weighted speed for each vehicle type (v_k) across various segments of the road network, where v_{ik} indicates the mean speed of vehicle type k at link i while l_i is the length of that link i.

$$v_k = \frac{\sum_i v_{ik} \cdot l_i}{\sum_i l_i} \tag{6}$$

Furthermore, Chandra and Kumar (2003) provide essential data on the average dimensions and projected areas for each vehicle category, as listed in Table 2.

Table 2: Classification of vehicle types and rectangular area projection size.

Type	Vehicles included	Average dimensions (m)	Rectangular area (m^2)
Motorcycle	Scooter, Motorbike	1.87 x 0.64	1.20
Car	Car, Jeep, Van	3.72 x 1.44	5.36

With motorcycles being predominant, their MEU is standardized at 1 as a baseline for assessing network influence. For cars, MEUs are calculated for each road segment using Equation (4) to determine their relative impact, with the distribution shown in Figure 6. Across 1,533 road segments, car MEUs range from 3.20 to 6.14, with an average of 4.78, indicating that the space occupied by one car is nearly equivalent to five motorcycles. This information is vital in networks where the volume of motorcycles far exceeds that of cars, enabling the development of traffic models and management strategies that account for the unique composition and behaviour in such settings.

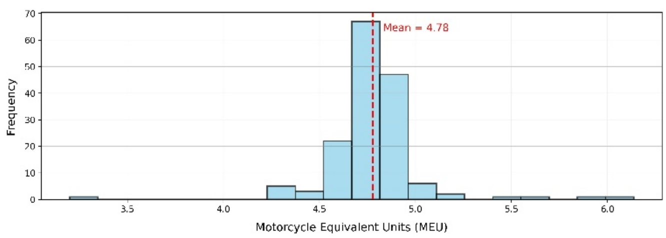

Figure 6: Distribution of MEU values across road sections.

This study further examines the relationship of MEU values with road geometry attributes such as length, width, capacity, and lane count for each link. Figure 7 shows scatter plots illustrating the correlation between MEUs and these geometric factors. The strength and direction of these relationships are then quantified using Pearson's correlation coefficient. It is observed that the low coefficients indicate a weak linear relationship between the MEU values and network attributes such as the number of lanes, link length, lane width, and road capacity within Ninh Kiều District. This suggests a general independence of the MEUs from these geometric characteristics. Further research is necessary to determine if the applicability extends beyond this case study, as local driving behaviours, infrastructure conditions, and regional differences may influence its relevance and utility. In conclusion, the MEU metric is significant for macroscopic traffic analysis of motorcycle-dependent areas.

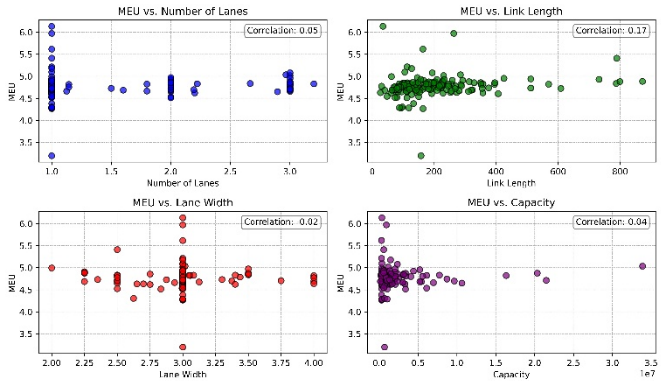

Figure 7: Correlation analysis of MEU values with road geometry attributes.

5.2. Accounting for Spatial Utilization: The Role of Area Occupancy

In contexts where standard density metrics are inadequate, especially in environments with irregular or absent lane discipline, the concept of 'area occupancy' becomes pivotal. It offers a more precise measure of traffic concentration and spatial utilization, accurately reflecting the complex dynamics of mixed traffic by accounting for the actual space occupied by each vehicle type. This metric, introduced by Mallikarjuna and Rao (2006) and built upon observations by Chandra and Sikdar (2000), considers the actual space occupied by vehicles. It offers a comprehensive view of traffic flow in mixed traffic where different vehicle types—from motorcycles to larger vehicles—interact and use road space differently. This shift to area occupancy (ρ_A), as expressed in Equation (7) by Mallikarjuna and Rao (2006), marks a significant shift in traffic analysis. This formula measures how much space each vehicle occupies in the study area over the specified observation period (T).

$$\rho_A = \frac{1}{T \cdot W \cdot L} \cdot \sum_{k=1}^{N} (O_k \cdot w_k \cdot l_k) \tag{7}$$

where,
- W, L: width and length of the study area,
- w_k, l_k: width and length of vehicle type k,
- O_k: occupancy time of vehicle type k (in seconds) and
- N: The set of vehicles.

The above formula helps to ascertain the thorough utilization of road space by different vehicle types in mixed traffic conditions. It takes into account the dimensional and operational characteristics of each vehicle to offer an in-depth perspective of their spatial impact on traffic flows. Introducing area occupancy as a measure marks a paradigm shift in understanding and analyzing heterogeneous traffic dominated by motorcycles. For the specific case of Ninh Kiều District, area occupancy at the link i (ρ_{A_i}) is determined as follows.

$$\rho_{A_i} = \frac{1}{T_i \cdot W_i \cdot L_i} \cdot \sum_t \sum_{k \in N_t} (w_k \cdot l_k) \tag{8}$$

where,

T_i : observation period, and

N_t : index of the vehicles that appeared at the time t.

5.3. Macroscopic Analysis for Motorcycle-Dependent Traffic

Considering the issues highlighted in subsections 5.1 and 5.2, the standard MFD is no longer relevant in scenarios involving mixed traffic with a significant presence of non-lane-based vehicles and requires refinement to analyze such environments. Equations (1) and (2) are then transformed to include MEU-based traffic properties and substitute density metrics with area occupancy. This adaptation adjusts the counts of larger vehicles into motorcycle-equivalent numbers and incorporates spatial utilization measures.

These modifications improve the MFD's utility for delivering a holistic view of network performance and accurately depicting transitions between free-flow and congested states. New equations, presented in Equations (9) and (10), refine the model further. Here, q_{MFD_t} denotes the network-scale traffic flow, weighted by the flow of cars ($q_{pc_{it}}$) and motorcycles ($q_{mc_{it}}$) on the link i during time interval t and adjusted by MEU factors. Similarly, traffic concentration is then measured by area occupancy ($\rho_{A_{MFD_t}}$), which is also weighted across the network to provide a macroscopic perspective on traffic performance.

$$q_{MFD_t} = \frac{\sum_i \left[\left(q_{pc_{it}} \cdot MEU_{car} \right) + q_{mc_{it}} \right] \cdot l_i}{\sum_i l_i} \tag{9}$$

$$\rho_{A_{MFD_t}} = \left(\sum_i \left(\frac{1}{T_i \cdot W_i \cdot L_i} \cdot \sum_t \sum_{k \in N_t} (w_k \cdot l_k) \cdot l_i \right) \right) / \sum_i l_i \tag{10}$$

As a result, Figure 8 contrasts network performance using two metrics for vehicle accumulation: density and area occupancy. The blue data plot, labelled as 'before adjustment' MFDs, utilizes density, which is suitable for homogeneous traffic but less effective in mixed traffic contexts. The orange data plot, labelled 'after adjustment' MFDs, employs area occupancy and is refined to better represent traffic systems predominantly composed of motorcycles.

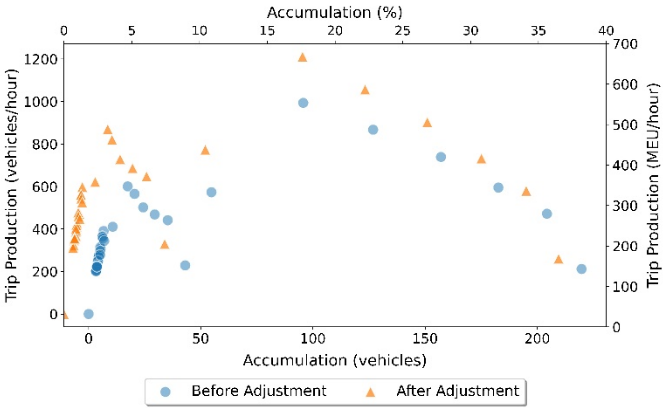

Figure 8: Comparative analysis of MFD using density and area occupancy.

6. Discussion

Network performance in Ninh Kiều District is evaluated with a modified three-dimensional MFD that accounts for the proportion of motorcycles. This MFD, which captures trip production and accumulation tracked at 10-minute intervals over a 10-hour simulation using the AIMSUN simulation model, is illustrated in Figure 9.

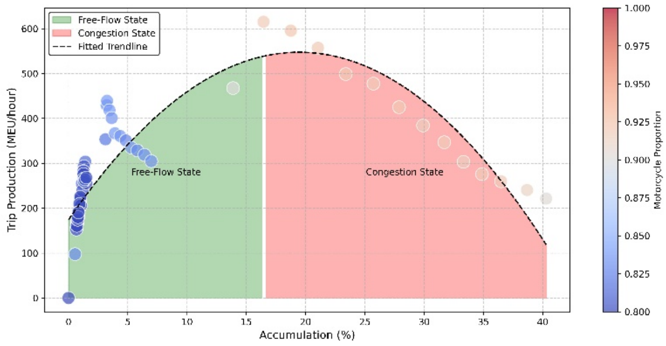

Figure 9: Modified MFD for mixed-motorcycle traffic.

The MFD initially exhibits a positive trend where increased trip production correlates with rising accumulation, signifying efficient network usage, known as the free-flow state. Furthermore, a hysteresis loop phenomenon is observed in the MFD before peak hour, likely caused by several factors. The unbalanced spatial distribution of traffic density within the network plays a significant role—while some areas may function relatively well, others become heavily congested, creating bottlenecks that hinder overall traffic flow. This imbalance causes a delay in returning to normal traffic conditions even as accumulation decreases. High traffic density, limited road capacity, inadequate infrastructure, changes in traffic patterns during peak hours, and driver behaviour exacerbate this effect by slowing recovery times. This phenomenon underscores the need to address spatial density variations and other contributing factors to mitigate congestion. More detailed analysis is needed in future work to understand the hysteresis phenomenon fully.

However, upon reaching a critical point of accumulation, the network hits its capacity limit, and further vehicle presence ceases to aid flow efficiency. The peak of trip production, occurring at 614.99 MEU per hour at 07:10 a.m., marks the maximum volume manageable before the onset of congestion. Secondary data analysis indicates that the network's throughput capacity is reached early due to notable morning commuter trends. Specifically, 61.2% of employed individuals begin work between 3 a.m. and 7 a.m., and 60.6% of students travel to school primarily between 6 a.m. and 7 a.m., making up 85.6% of all school-related trips. This leads to a significant spike in traffic volume, increasing by 146.37% from 6 a.m. to 7 a.m. Consequently, the capacity threshold is reached when 16.39% of the network is occupied by vehicles, leading to a decline in the MFD curve and marking a transition to a congestion state.

Further accumulation then resulted in decreased trip production and potential gridlock. The relatively low accumulation threshold can be attributed to the fact that 74.65% of the roads in Ninh Kiều District are local and residential types. It is also observed that motorcycles enhance trip production at low to moderate accumulation levels due to their compact size and higher manoeuvrability, allowing efficient space utilization. Nonetheless, as vehicle volume approaches and exceeds capacity, the advantageous impact of motorcycles diminishes, signalling a drop in overall traffic system performance.

7. Conclusion

This study investigates mixed traffic dynamics in Ninh Kiều District, highlighting the inadequacy of traditional traffic flow models designed for homogeneous, lane-disciplined settings when applied to areas where motorcycles dominate and frequently disregard lane markings. A recalibrated MFD incorporating MEU metrics and area occupancy has been introduced to address these complexities, moving beyond standard density-based measurements. This MFD offers a refined macroscopic perspective of traffic flow and concentration, better reflecting the spatial patterns in this context. The MEU metric, which acknowledges motorcycles' smaller size and more excellent manoeuvrability than standard PCUs, offers a more appropriate measure for evaluating their impact in motorcycle-dependent settings.

The novelty of this research lies in its significant progress in adapting the MFD for mixed traffic with a high prevalence of motorcycles. This approach introduces a shift from density metrics to area occupancy, addressing a gap in analytical tools and providing a more accurate representation of these systems. Notably, alongside the effort to develop an MFD tailored for such context, the study also marks a seminal contribution to establishing the MFD for traffic patterns in Southeast Asia. The recalibrated MFD, validated against empirical data, effectively highlights key operational patterns and potential bottlenecks in traffic networks.

Despite its contributions, the study scope is inherently limited by focusing exclusively on the Ninh Kiều District. This specific network and the geographical extent may not fully represent other urban or rural settings, which could differ significantly in traffic behaviour, infrastructure, and regulatory frameworks. Consequently, while the findings are relevant to the study area, their generalizability to different contexts may not be straightforward, necessitating prudent consideration and caution when applying them to other regions. Moreover, although the AIMSUN model is useful for detailed simulations, it may include assumptions that do not perfectly capture the complex interactions in highly heterogeneous traffic environments. Future research should address these limitations by extending the study to include diverse locations with varying traffic compositions and infrastructure conditions to test the applicability of the findings. Additionally, comparative studies employing different simulation software or integrating empirical field data could enhance the validity of the modelling approach. Investigating the impacts of different management strategies within these mixed traffic settings would also be valuable.

Acknowledgements

The authors would like to express gratitude to the "*Sustainable Urban Public Transport and Central Area Traffic Management Study for Can Tho City*" project, conducted by Sustainable Urban Development JSC, for their support with secondary data.

References

Ambühl, L., Loder, A., Bliemer, M.C.J., Menendez, M., & Axhausen, K.W. (2018). Introducing a re-sampling methodology for the estimation of empirical macroscopic fundamental diagrams. *Transportation Research Record, 2672*(20), 239–248. doi: 10.1177/0361198118788181

Arasan, T., & Arkatkar, S.S. (2008). Estimating passenger car units for vehicles of heterogeneous traffic using computer simulation. Presented at the Transportation Research Board 87th Annual Meeting, Washington D.C., January 2008.

Cao, N., Sano, K., Minh, C.C., & Matsumoto, S. (2009). *Motorcycle equivalent units at road segments under mixed traffic flow in urban road.* In Proceedings of the Eastern Asia Society for Transportation Studies, 7.

Chandra, S., & Kumar, U. (2003). Effect of lane width on capacity under mixed traffic conditions in India. *Journal of Transportation Engineering, 129*(2), 155–160. doi: 10.1061/(ASCE)0733-947X(2003)129:2(155)

Chandra, S., & Sikdar, P. K. (2000). Factors affecting PCU in mixed traffic situation on urban roads. *Road and Transport Research, 9*(3), 40–50.

Daganzo, C. (2007). Urban gridlock: Macroscopic modeling and mitigation approaches. *Transportation Research Part B: Methodological, 41*(1), 49–62. doi: 10.1016/j.trb.2006.03.001

Geroliminis, N., & Daganzo, C.F. (2007). *Macroscopic modeling of traffic in cities. Technical Report*. The National Academies of Sciences, Engineering, and Medicine: Washington, DC, USA.

Geroliminis, N., & Daganzo, C.F. (2008). Existence of urban-scale macroscopic fundamental diagram: Some experimental findings. *Transportation Research Part B: Methodological, 42*(9), 759–770. doi: 10.1016/j.trb.2008.02.002

Geroliminis, N., Sun, J. (2011). Properties of a well-defined macroscopic fundamental diagram for urban traffic. *Transportation Research Part B: Methodological, 45*(3), 605–617. doi: 10.1016/j.trb.2010.11.004

Khan, S.I., & Maini, P. (1999). Modeling heterogeneous traffic flow. *Transportation Research Record, 1678*(1), 234–241. doi: 10.3141/1678-28

Knoop, V.L., Jong, D., & Hoogendoorn, S.P. (2014). The influence of the road layout on the network fundamental diagram. *Transportation Research Record, 2421*(1), 22–30. doi: 10.3141/2421-03

Kov, M., & Yai, T. (2010). Traffic characteristics of motorcycle-dominated urban street considering the effect of light vehicle. *Journal of the Eastern Asia Society for Transportation Studies, 8,* 1806–1821. doi: 10.11175/eastpro.2009.0.337.0

Lee, T.C. (2007). *An agent-based model to simulate motorcycle behaviour in mixed traffic flow*. Doctoral Dissertation, Imperial College London, London.

M.,S., & Verma, A. (2016). Review of studies on mixed traffic flow: perspective of developing economies. *Transportation in Developing Economies, 2*(5). doi: 10.1007/s40890-016-0010-0

Mallikarjuna, C., & Rao, K. R. (2006). Area occupancy characteristics of heterogeneous traffic. Transportmetrica, 2, 223–236. doi: 10.1080/18128600608685661

Minh, C.C., Sano, K., & Matsumoto, S. (2005). The speed, flow, and headway analyses of motorcycle traffic. *Journal of the Eastern Asia Society for Transportation Studies, 6*, 1496–1508. doi: 10.11175/easts.6.1496

Minh, C.C., Sano, K., & Nguyen, C.Y. (2007). Acceleration and deceleration models of motorcycle at signalized intersections. *Journal of the Eastern Asia Society for Transportation Studies, 7*, 2396–2411. doi: 10.11175/easts.7.2396

Nguyen, D.T., & Kajita, Y. (2018). Traffic congestion and impact on the environment in Vietnam: Development of public transport system - experience from actual operation of bus in Hanoi. *Journal of Civil & Environmental Engineering, 8*(3). doi: 10.4172/2165-784X.1000317

Robbins, C.J., & Fotios, S. (2020). Motorcycle safety after-dark: The factors associated with greater risk of road-traffic collisions. *Accident Analysis & Prevention, 146*. doi: 10.1016/j.aap.2020.105731.

Suwanno, P., Kasemsri, R., Duan, K., & Fukuda, A. (2021). Application of macroscopic fundamental diagram under flooding situation to traffic management measures. *Sustainability, 13*, 11227. doi: 10.3390/su132011227

Tan, D.T., Tu, T.V., & Sano, K. (2018). Estimation of motorcycle equivalent units on urban streets. *Asian Transport Studies, 5*(2), 243–255. doi: 10.11175/eastsats.5.243

Tonko, M., & Gidwani, M. (2018). *Motorcycle growth prospects in Southeast Asia: rise of business use two-wheelers*. Roland Berger GmbH: Munich, Germany.

Vietnam General Statistics Office (2021). Vietnam Statistical Yearbook (Niên giám thống kê Việt Nam). Retrieved from https://www.gso.gov.vn/wp-content/uploads/2022/08/Sach-Nien-giam-TK-2021.pdf. Accessed March 7, 2024.

Journal of Road Engineering Association of Asia and Australasia
Journal homepage: www.reaaa.net
JREAA – 1/2025: 38-44

OPEN ACCESS

Predicting Highway Flood Risk in Thailand Using Machine Learning

Pongsakorn Chullabodhi[1,*], Pichaya Rungruangvirojn[1], Suladda Sapsin[2] , Supakron Meelap[3] & Waritz Rattanasiriphan[4]
*Corresponding author: warit.ra@doh.go.th

[1,*,1,2,3,4] *Department of Highways, 2/486 Si-Ayutthaya Road, Ratchathevi Bangkok 10400*

ABSTRACT

In response to the increasing problem of floods damaging Thailand's highways and causing widespread disruption, this work offers a new tool for assessing the likelihood of highway flooding, leveraging Machine Learning (ML). The core of the analysis is integrating various datasets: historical rainfall data, historical national highways flood level data, and Thailand's weekly rainfall forecasted data. This integration is achieved through Random Forest (RF) and Artificial Neural Network (ANN) models. We aim to significantly improve disaster preparedness and decision-making for highway users and infrastructure managers by predicting the severity of flooding events. This can be achieved by implementing real-time alert systems on highway networks. These systems would utilize flood forecasts to warn commuters about potential dangers and allow them to make informed decisions, such as avoiding flooded routes.
Additionally, highway authorities can take proactive measures such as deploying emergency response teams or closing vulnerable sections in advance. The study recommends systematically establishing a highway network alert system to minimize future disaster risks. This system would disseminate real-time flood warnings to regional authorities through a dedicated Highway Disaster Management System (HDMS) website portal. Both categories of ML algorithms demonstrate strong predictive abilities for anticipating flood levels. The ANN model could be integrated into the existing HDMS of the Department of Highways (DOH).

ARTICLE INFO

Article History:
Received 20 Sep 2024
Received in revised form
21 Jan 2025
Accepted
01 Apr 2025
Available online
01 May 2025

Keywords:
Flood-level forecasting
Machine learning
Big data
Disaster risks
Highway network

1. Introduction

Thailand faces risks from floods and public disasters, which have become more frequent and severe and cause significant damage to lives and property. These disasters result from both natural and anthropogenic causes. At the same time, some parts of the highway network in Thailand's northern and southern regions experience recurring floods, affecting safety and causing property loss for commuters travelling on these routes (Chullabodhi et al., 2024). Recent studies have shown the potential of using ML techniques to forecast flood risk and support infrastructure resilience. (Tachaudomdach et al., 2021). Also, another novel research on flood forecasting systems leverages state-of-the-art learning strategies, and the system demonstrated high accuracy in forecasting flood incidents across specific areas and timeframes (S. Puttinaovarat & P. Horkaew, 2020).

The Bureau of Highways Maintenance Management (BHMM), DOH, has studied and developed an RF model to predict flood levels on Thailand's highway network. Regarding hydrologic applications, an RF-based assessment model for estimating the danger of regional flood hazards (Wang et al., 2015); A RF drought forecast model has been presented to forecast the monthly standardized precipitation index (SPI) time series (Chen et al., 2012); Daily water levels at a station on the Mekong River in Vietnam were forecasted (T. -T. Nguyen et al., 2015).

Compared to conventional statistical models, the ANN technique delivered more accurate predictions (Li et al., 2010). Since its introduction in the 1990s, ANN algorithms have often been used for flood prediction models (Wu & Chau, 2010). ANNs interpret historical data rather than the physical features of a catchment. Therefore, they are regarded as reliable data-driven methods for developing black-box models of intricate and nonlinear interactions between rainfall and flooding (Sulaiman & Wahab, 2018).

The use of ML in systems designed for predicting floods has grown significantly. The RF model has demonstrated high accuracy and robustness, while the ANN model has shown promising results in terms of speed and effectiveness. (Mosavi et al., 2018). Based on the available data, this study will leverage two ML algorithms - RF and ANN - to predict the likelihood and severity of highway flooding. Therefore, both methods are employed to estimate trends for the 7-day upcoming floods, incorporating independent variables to predict flood levels: historical rainfall data, historical national highways flood level data, and Thailand's weekly rainfall forecasted data.

To enhance disaster preparedness, the researcher created a model to estimate floods' potential impact and seriousness on the highway network. Furthermore, the model seeks to assist DOH personnel and other relevant officials in devising strategies or actions to address and prevent future floods.

1.1 Objectives

This research has objectives:

- To predict flood levels on road surfaces in the highway network using ML and evaluate the model's performance.
- To support DOH personnel in preparing machinery and human resources, implementing preventive measures, and managing floods on road surfaces.

1.2 Scope of Research

- The study area covers the highway network throughout Thailand, encompassing 1,530 routes with a total road length of 51,925.81 kilometres, as shown in Figure 1.

Predictions of flood levels on the highway network's road surfaces were determined by examining the correlation between historical rainfall data, historical national highways flood level data, and Thailand's weekly rainfall forecasted data. The analysis did not consider other factors that could result in flooding, such as runoff, human activities, and flash floods.

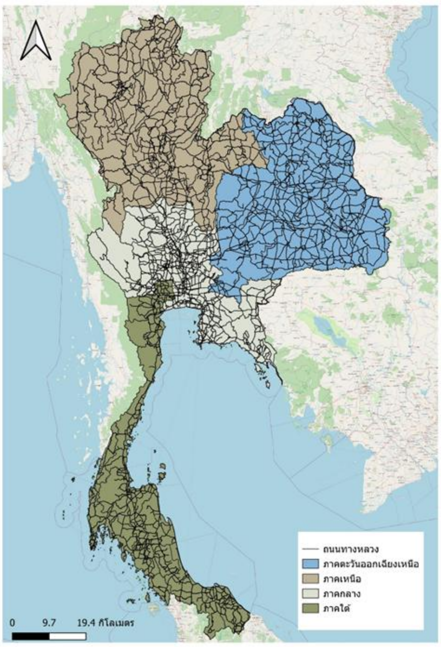

Figure 1. Map of Thailand's road network.

2. Methodology and Data

2.1 Random Forest

Random Forest is an ML algorithm that enables computers to learn autonomously. It is capable of both classification and regression tasks. (Breiman, 2001). In regression, decision trees are employed to predict continuous values, thus enhancing the accuracy of outcome predictions.

In RF, the key concept is to produce a variety of decision trees (ranging from 10 to over 1000 models). While each tree receives distinct training data, their combined predictions should be similar. Subsequently, the algorithm determines the mean or median based on the output of each decision tree for a regression task (Janthongpoon et al., 2022), as depicted in Figure 2. An increase in data is expected to enhance the accuracy of the model's predictions.

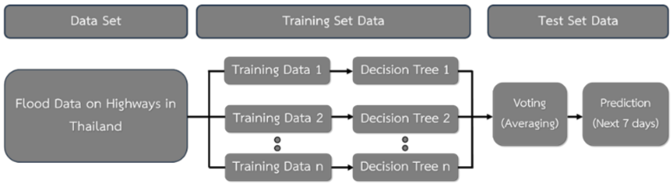

Figure 2. RF process (Chullabodhi et al., 2024).

Nevertheless, being aware of potential pitfalls or limitations in model building is crucial. One of the main concerns is to confirm that the data values show variability in line with the decision tree and avoid outliers that significantly differ from the other values. Such discrepancies could adversely affect the accuracy of predictions. Hence, it is recommended that data preprocessing be implemented prior to training the model.

2.2 Artificial Neural Network

ANNs are proficient mathematical systems that employ parallel processing effectively, enabling them to replicate the structure of biological neural networks with interconnected neuron units. ANNs are esteemed as the most popular learning algorithms within ML. They are acknowledged for their versatility and effectiveness in modelling complex flood processes with a high level of fault tolerance and accurate approximation (Abbot & Marohasy, 2014). ANNs have demonstrated their effectiveness in modelling complex, nonlinear relationships inherent in hydrological and transportation systems. (Chikaraishi et al., 2020).

The architecture of ANN typically consists of an input layer, one or more hidden layers, and an output layer, as depicted in Figure 3. The weighted sum of the inputs at each neuron generates an output signal through an activation function (Xing et al., 2017). The hidden layers extract and learn the features from the input data, while the output layer produces the final predictions. The input layer of the ANN architecture is responsible for receiving data from various sources. Accordingly, the number of neurons in the input layer is determined by the number of input data sources. The data is then actively processed through the hidden and output layers of the network. An experimental, iterative approach frequently establishes the appropriate number of hidden layers and the number of neurons in each hidden layer. The backpropagation (BP) training process in ANN involves adjusting the weights of the connections between neurons to minimize the error between the predicted and actual outputs. (Yeh, 1998).

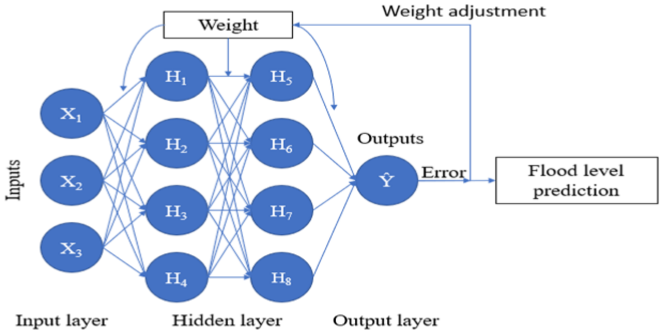

Figure 3. ANN process with BP algorithm.

2.3 Data Set

2.3.1 Historical rainfall data

The historical rainfall data is meteorological information sourced from the Smart Water Operation Center (SWOC), Royal Irrigation Department (RID), and the Ministry of Agriculture and Cooperatives (MAC), which provides rainfall quantities per province in millimetres (mm.).

2.3.2 Historical national highways flood level data

The historical national highways flood level data is information regarding the vertical height of stagnant water on the road surface. This data was obtained from reports by DOH officers who measured water levels at midpoints of the road in centimetres (cm.), as shown in Figure 4. These reports are then collated through the HDMS, DOH.

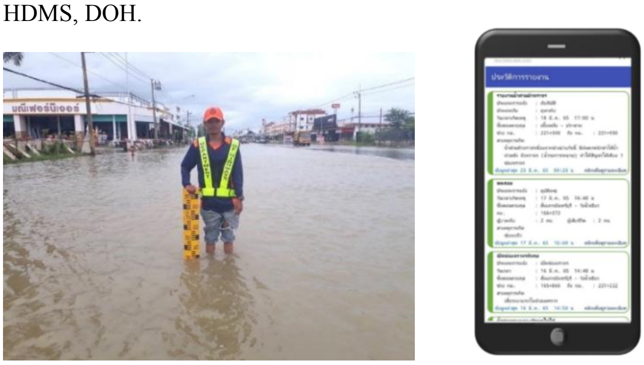

Figure 4. The DOH officer measures the flood level at the road's midpoint (left), and the HDMS page is on a smartphone to record the flood level (right).

2.3.3 Thailand's Weekly Rainfall Forecasted Data

Thailand's weekly rainfall forecasted data was introduced from the Meteorological Information System (MIS) through the Application Programming Interface (API), sourced from the Thai Meteorological Department (TMD), Ministry of Digital Economy and Society (MDES). This data resulted from weather monitoring and forecasting Thailand's weekly rainfall, which accumulated weekly rainfall data in Thailand (forecasted weekly rainfall in mm.). Integrating this data with the QGIS software must be presented in raster format using the Inverse Distance Weighting (IDW) technique. This process involves image processing (Wijithanasarn et al., 2022), as illustrated in Figure 5.

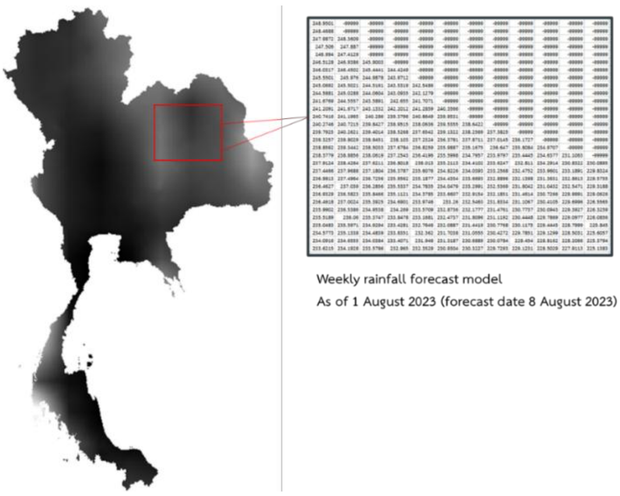

Figure 5. An example of the 7-day forecasted rainfall model.

The researchers reviewed relevant research and literature and developed models to predict flood levels on Thailand's highway network. The models' inputs are presented in Table 1.

Table 1. Sources of data used to develop models.

No.	Data	Source
1	Historical rainfall data	SWOC, RID
2	Historical national highways flood level data	HDMS, DOH
3	Thailand's weekly rainfall forecasted data	MIS, TMD

2.4 The Highways Disaster Management System

BHMM has created the HDMS to enhance disaster management efficiency. This system is used to report incident status or disasters through HDMS' LINE Official Account and the website of the Disaster Management Center, BHMM, DOH. It serves as a tool to support the operations of DOH central and regional officers during emergency or disastrous incidents. Officers can inform about highway incidents, such as floods, storms, landslides, wildfires, and road closures. Additionally, the system can analyze and assess highway disaster risks, providing alerts on the risk of areas with recurring floods, historical peak water levels, and current water levels. This information is summarized and presented through the system's dashboard, which can display overall reporting, incident tracking, and risk information in various types of maps useful for disaster management. The system's display is illustrated in Figure 6.

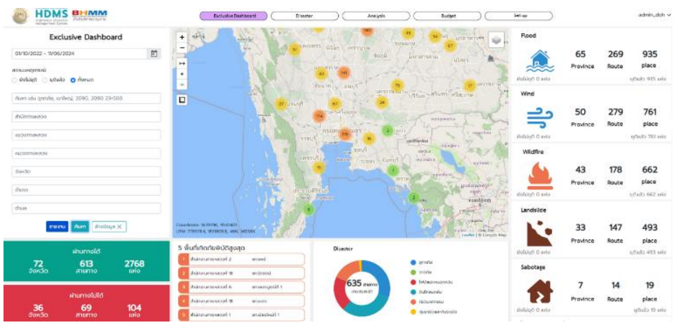

Figure 6. The HDMS dashboard summarizes the current situation on the highway network.

2.5 Flood Level Prediction Process

The process began with collecting independent variables for flood-level prediction, including historical rainfall data, historical flood levels on national highways, and Thailand's weekly rainfall forecasted data. These data were preprocessed before being analyzed, and the RF and ANN were trained to predict the flood levels on the highway networks. Lastly, the predicted data from the model was compared with the actual flooded levels, completing the prediction process illustrated in Figure 7.

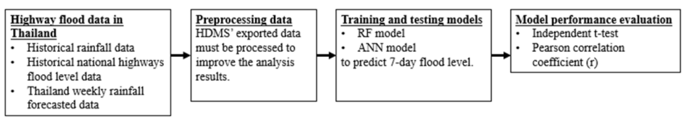

Figure 7. Flood prediction process.

2.5.1 Preprocessing data

Before training the models, researchers reviewed the data exported from the HDMS to enhance the analysis results. Disaster types categorized the data, and correlating water level data were verified with actual images to exclude inaccurate or false reports from the analysis.

2.5.2 Training and testing the models

The models were trained by three independent variables, which were historical rainfall data, historical national highways flood level data, and Thailand's weekly rainfall forecasted data from the MIS, TMD with the details as follows:

- Historical rainfall data: This is the volume of rainfall in millimetres at each route, control section, and kilometre posts on the highway networks. Where the segments are located in a specific province, the rainfall data for that area was used.
- Historical national highways flood level data: The data from October 2022 to July 2023 (9 months) will be used as training data, and additional data will be collected as cumulative data if forecasts are made in subsequent months, as shown in Figure 8.
- Thailand's weekly rainfall forecast data was derived from weather measurements and forecasting from the Thailand Weekly Rainfall System, the MIS, and the DWR, which provide weekly rainfall forecasts.

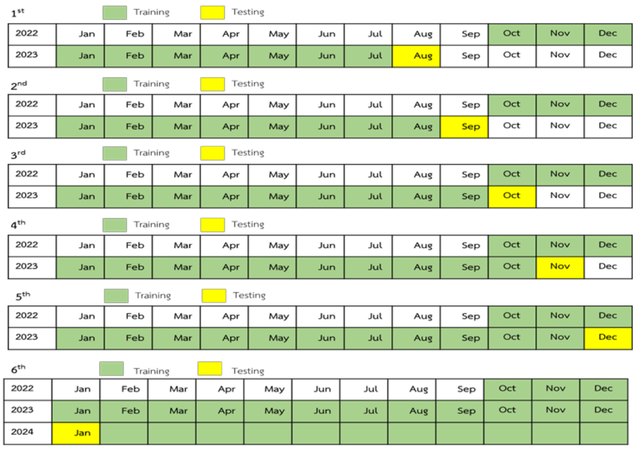

Figure 8. The training and testing data are used to build an ML model to predict highway flood levels.

2.5.3 Training RF model

The initial steps of the RF model involve randomly selecting data from the entire dataset and constructing decision trees to derive predictions. Subsequently, a predetermined number of trees is picked for decision-making, and this random selection process, paired with forming decisions from data samples, is reiterated continuously to train the data. Before predictions can be made, the predicted values are derived from the decisions of each tree. Regression analysis uses the averaging method to forecast highway flood levels by averaging predictions from all trees (BHMM, 2022). The process is illustrated in Figure 9.

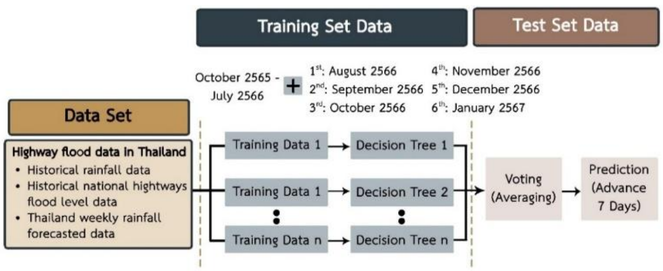

Figure 9. RF process.

2.5.4 Training ANN model

The same independent variables for RF have been utilized to develop the ANN model to predict a 7-day flood level on the highway network. Multiple network structures with distinct hidden neuron quantities undergo training and assessment. The neural network was learned using the BP algorithm, and the rectified linear unit (Relu) was chosen as the transfer function in hidden layers. The best performance network architecture for the ANN model was identified by analyzing the performance measures obtained during testing. Table 2 contains the neural network architecture parameters for the ANN model.

Table 2. ANN architecture parameters for the flood forecasting model.

	ANN
Number of input neurons	3
Number of hidden neurons	8
Number of hidden layers	2
Learning rate	0.01
Transfer function of hidden layer	Relu
Transfer function of output layer	Linear
Training algorithm	BP
Optimizer algorithm	Adam
Batch size	32
Training cycles, epochs(e)	100

2.6 Model Performance Evaluation

After obtaining data from the flood level forecast model and the actual flood occurrence reports through the HDMS, the accuracy of the ML model was assessed using statistical principles. This evaluation involved using the following methods.

2.6.1 The independent t-test method

Statistical testing of two independent groups using the independent t-test method under the hypothesis that the combined variance is equal but unknown. This involves comparing the means of quantitative variables between two independent sample groups and performing a two-tailed test with a confidence level of 95% (alpha value of 0.05) (Phonprasertmanit, 2015). The hypotheses are as follows:

$$H_0\text{: } \mu_{model} = \mu_{actual} \tag{1}$$

$$H_1\text{: } \mu_{model} \neq \mu_{actual} \tag{2}$$

Once the calculation of the aforementioned parameter is completed. If the p-value > α, we accept H_0 or the experimental hypothesis as accurate. However, if the p-value < α, we reject H_0 and accept H_1. A low p-value indicates that the observed data are unlikely under the null hypothesis. In contrast, a high p-value suggests that the observed data are consistent with the null hypothesis.

2.6.2 Pearson Correlation Coefficient (r)

Correlation analysis is a widely used statistical method for assessing the strength and direction of the linear relationship between two variables. (Falk & Well, 1997). The Pearson correlation coefficient, denoted by r, is the most commonly used correlation measure. (Schober et al., 2018). In the context of ML, correlation analysis can be employed to evaluate the accuracy of predictive models by examining the relationship between the predicted values and the actual observed values. (Gupta et al., 2022; Pratama et al., 2021). A value of r close to 1 indicates a strong positive linear relationship, while a value close to -1 suggests a strong negative linear relationship. Equation 3 shows the Pearson correlation coefficient (r) test, and its interpretation is summarized in Table 3.

$$r = \frac{\sum(x_i - \bar{x})(y_i - \bar{y})}{\sqrt{\sum(x_i - \bar{x})^2 x \sum(y_i - \bar{y})^2}} \quad (3)$$

Table 3. A table illustrates the meaning of the parameter values.

Parameter	Value	Interpretation
r	> 0.8	Very high positive correlation
	0.6 - 0.8	High positive correlation
	0.4 - 0.6	Moderate positive correlation
	0.2 - 0.4	Low positive correlation
	< 0.2	Negligible correlation

2.6.3 Model Performance Evaluation

After completing the flood level prediction on highways in Thailand using RF and ANN, the model's performance will be evaluated using two evaluation approaches as follows:

- Independent t-test method
- Pearson correlation coefficient (r)

If the model meets the criteria for all the above parameters, it indicates that the RF and ANN models perform accurate predictions.

3. Results and discussions

3.1 HDMS output page displaying flood level prediction

The system output reveals flood forecast data 7 days in advance, evaluated from the RF and ANN model on highway networks in the HDMS, as illustrated in Figures 10a, 10b, and 11.

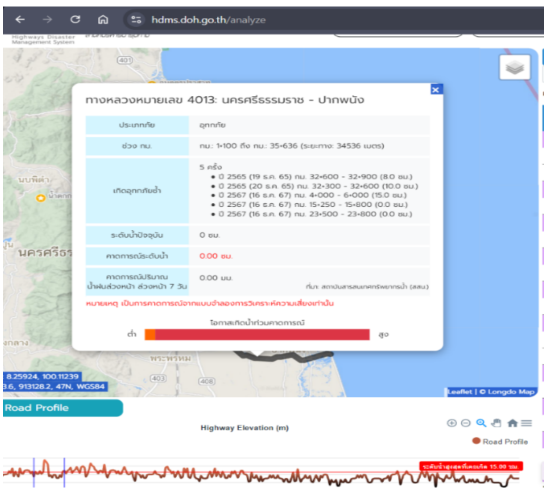

Figure 10a. An example of a flood-level prediction page on 12th November 2024 (predicted on 19th November 2024).

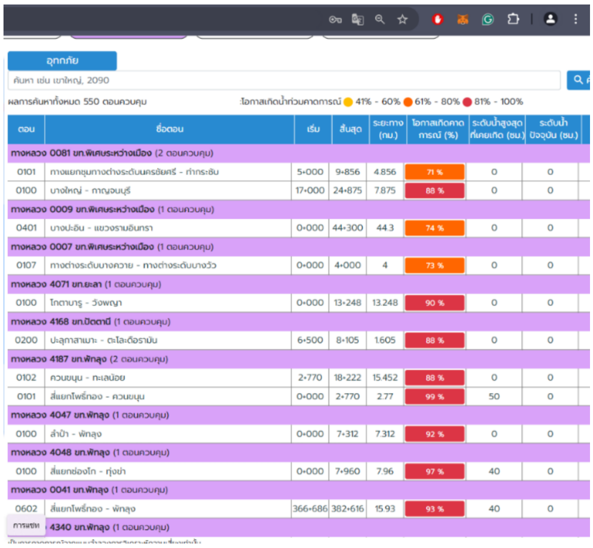

Figure 10b. An example of a flood-level prediction page on 12th November 2024 (predicted on 19th November 2024).

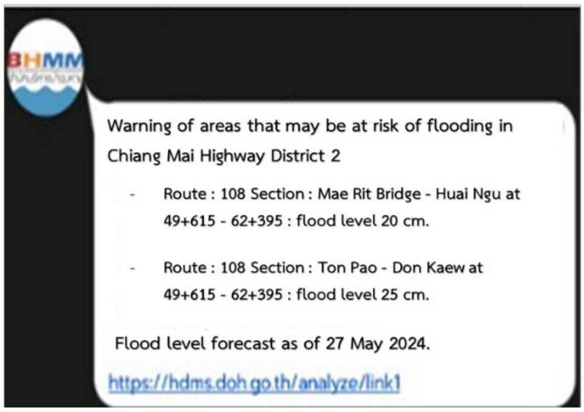

Figure 11. An example of alert officials to watch out for flooding on 12th November 2024 (predicted on 19th November 2024).

3.2 Model Performance Evaluation Results

In this study, basic statistical principles used to evaluate the model's performance include the Pearson correlation coefficient (r) and independent t-test method, then comparing the actual flood location predicted by the model with the floods obtained from the model. Higher accuracy is achieved with more collected data, demonstrating the validity of the study's hypothesis. This means that increasing the amount of training data will result in more accurate model predictions. The ML model RF demonstrated exceptional classification accuracy on the training and testing datasets. Additionally, related studies on flood risk assessment revealed that RF-based ML models were an outstanding choice for flood risk assessment (Khosravi et al., 2018; Wang et al., 2015). To investigate the performance of an ANN model, the predicted flood level was compared with actual readings, presenting the accuracy of the prediction (Elsafi, 2014). Another study on flood forecasting systems demonstrated the ML models' ability to predict flood events accurately. ANN and RF were the ML models with the highest performance (S. Puttinaovarat & P. Horkaew, 2020).

The model's performance evaluation showed that its accuracy score is reasonable, indicating that the prediction results are pretty accurate, as shown in Tables 4 and 5.

Table 4. RF model accuracy validation.

Month, Year	Sample (N)	r	p-value	α	Result
August 2023	1,312	0.89	0.42	0.05	
September 2023	1,364	0.87	0.51	0.05	
October 2023	1,586	0.86	0.08	0.05	Accept H_0
November 2023	1,811	0.89	0.12	0.05	
December 2023	1,915	0.88	0.17	0.05	
January 2024	2,031	0.86	0.09	0.05	

Table 5. ANN model accuracy validation.

Month, Year	Sample (N)	r	p-value	α	Result
August 2023	1,312	0.87	0.61	0.05	
September 2023	1,364	0.89	0.70	0.05	
October 2023	1,586	0.9	0.15	0.05	Accept H_0
November 2023	1,811	0.86	0.26	0.05	
December 2023	1,915	0.91	0.14	0.05	
January 2024	2,031	0.87	0.11	0.05	

3.3 Comparison of actual flooding locations with predicted locations

The predicted flood locations from the RF and ANN models were plotted against the actual flood locations, extracted from HDMS, over six months (from August 2023 to January 2024) to assess the model's performance by comparing the overlapping flood locations. The amount of data for each month is summarized in Tables 4 and 5. These plots suggest that the RF and ANN models adequately predict flood occurrence on highway networks since the predicted locations from the model significantly overlap with the actual flood locations, as exemplified in Figure 12.

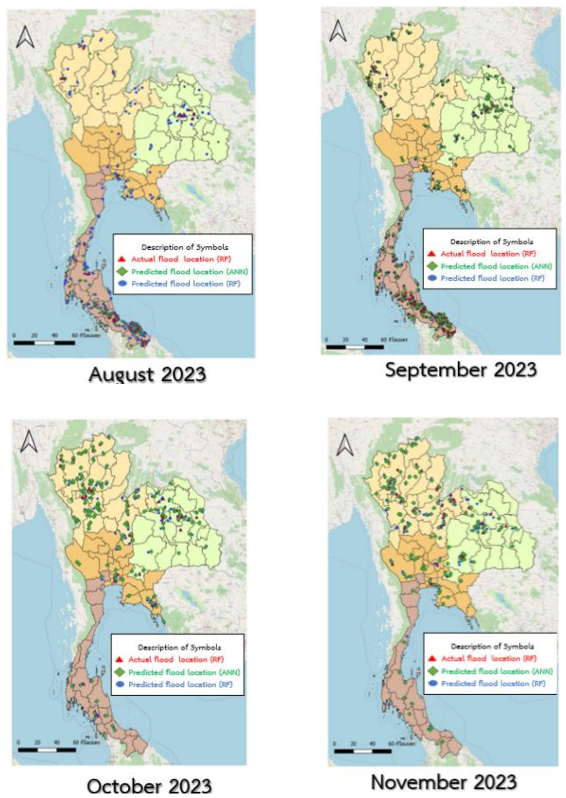

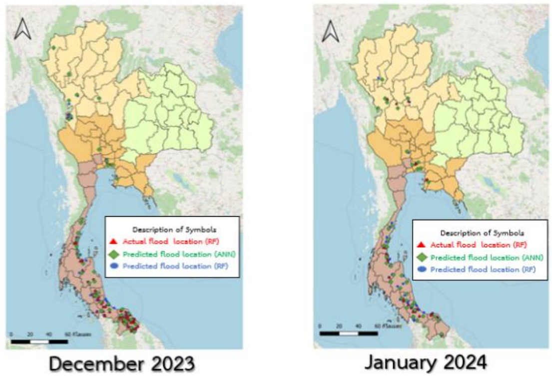

Figure 12. Regions' actual flooding locations with model-predicted locations (RF and ANN) from August 2023 to January 2024.

4. Conclusion and Recommendations

The RF and ANN models can accurately predict flood levels on highway networks for the same input data. The analysis uses three independent variables: historical rainfall data, historical national highways flood level data using data, and Thailand's weekly rainfall forecasted data from October 2022 to July 2023. These data collections were used as the training data for predicting flood levels in six months (from August 2023 to January 2024). Additionally, the performance of the flood prediction model was evaluated using statistical techniques by comparing model-predicted data with the actual flood reports from the HDMS. The results showed that the parameters, including the Pearson correlation coefficient (r) and the independent t-test analysis, passed the criteria each month. This indicates that the flood prediction models for highway networks are accurate and precise, with consistent data. As more data is added cumulatively to train the models, the accuracy of the predicted results can be achieved. The results led to the conclusion that both the RF and ANN models are practical for predicting flood levels on national highways. The ANN model could be integrated into existing HDMS and DOH. When compared to more advanced models, ANN is favoured for its simplicity. Artificial neural networks are the most efficient method for predicting floods in situations with a lack of data.

4.1 Parameter settings

The study's parameters must be selected according to parameter selection techniques, such as using correlation analysis (with correlation coefficient) to identify the parameters most related to the study's outcomes. For instance, it is essential to determine whether to use a classification model when the correlation coefficient is close to zero or a regression model when it is close to one.

4.2 Model accuracy

The research demonstrates the model's performance and accuracy, which can be further developed in the following years. This will aid in analyzing and identifying risk locations or areas prone to flooding on the highway network to prepare for potential floods. The underlying assumption is that increasing the training data will enhance the model's prediction accuracy.

4.3 Limitations and Future Research Direction

The study has some limitations that should be considered. First, the availability and quality of the data used in the analysis may impact the accuracy of the predictions. The rainfall data used may not fully capture the complex hydrological processes that contribute to highway flooding, and more detailed data on factors such as soil moisture, groundwater levels, and land use may be needed to improve the predictive power of the models. Future research should explore ways to address these limitations, such as incorporating additional data sources, improving data collection methods, and exploring more advanced ML techniques. Additionally, the transferability of the models to other regions or contexts should be investigated, as the specific characteristics of Thailand's highway network and climate may limit the generalizability of the findings.

Secondly, the study focuses on a specific geographic region, and the generalizability of the findings to other areas may be limited. Data collection within the Department of Highways' jurisdiction alone might not adequately cover other relevant places. Data from different connected fields should be investigated further and included in the model for more accuracy and comprehensiveness.

Despite these limitations, the promising results of this study provide a strong foundation for further research and development in highway flood risk prediction using ML techniques.

Further studies should expand the study's scope by incorporating additional data sources, such as social media and satellite imaging, to enhance prediction timeliness and accuracy. Assuring scalability and robustness, improving model designs, and assessing the feasibility of deploying real-time flood alarm systems for highway networks. These initiatives seek to provide Thailand and other areas dealing with comparable issues with a comprehensive and flexible highway flood risk control approach.

Acknowledgements

The research team would like to thank the Department of Highways (DOH) and the Ministry of Transport (MOT) for providing data and support for this research endeavour. We also extend our thanks to the Smart Water Operation Center (SWOC), Royal Irrigation Department (RID), and the Ministry of Agriculture and Cooperatives (MAC) for providing rainfall data analysis services. Lastly, we express our appreciation to the Thai Meteorological Department (TMD) and the Ministry of Digital Economy and Society (MDES) for their rainfall prediction models. Without the cooperation and knowledge-sharing from these organizations, this research would not have been possible.

References

Abbot, J., & Marohasy, J. (2014). Input selection and optimization for monthly rainfall forecasting in Queensland, Australia, using artificial neural networks. Atmospheric Research, 138, 166–178. 10.1016/j.atmosres.2013.11.002

BHMM. (2022). Disaster risk analysis and assessment project.Bureau of Highways Maintenance Management.

Breiman, L. (2001). Random Forests. Machine Learning, 45(1), 5–32. 10.1023/A:1010933404324

Chen, J., Li, M., & Wang, W. (2012). Statistical Uncertainty Estimation Using Random Forests and Its Application to Drought Forecast. Mathematical Problems in Engineering, 2012(1), 915053. 10.1155/2012/915053

Chikaraishi, M., Garg, P., Varghese, V., Yoshizoe, K., Urata, J., Shiomi, Y., & Watanabe, R. (2020). On the possibility of short-term traffic prediction during a disaster with machine learning approaches: An exploratory analysis. Transport Policy, 98, 91–104. 10.1016/j.tranpol.2020.05.023

Chullabodhi, P., S. S., & Meelap, S. (2024). Flood-Level Forecast Highways Network by Machine Learning. Paper presented at the The 29th National Convention on Civil Engineer, the Empress Hotel Chiang Mai,

Elsafi, S. H. (2014). Artificial Neural Networks (ANNs) for flood forecasting at Dongola Station in the River Nile, Sudan. Alexandria Engineering Journal, 53(3), 655–662. 10.1016/j.aej.2014.06.010

Falk, R., & Well, A. D. (1997). Many Faces of the Correlation Coefficient. Journal of Statistics Education, 5(3), null. 10.1080/10691898.1997.11910597

Gupta, I., Mittal, H., Rikhari, D., & Singh, A. K. (2022). MLRM: A MULTIPLE LINEAR REGRESSION BASED MODEL FOR AVERAGE TEMPERATURE PREDICTION OF A DAY.

Janthongpoon, Jirawat, P.L., & Bunrasri, P. (2022). A Study of urban expansion with random forest techniques: A case study of Mueang Songkhla District, Songkhla Province. Paper presented at the The 27th National Convention on Civil Engineer, Chiang Rai , Thailand.

Khosravi, K., Pham, B. T., Chapi, K., Shirzadi, A., Shahabi, H., Revhaug, I., Prakash, I., & Tien Bui, D. (2018). A comparative assessment of decision trees algorithms for flash flood susceptibility modeling at Haraz watershed, northern Iran. Science of the Total Environment, 627, 744–755. 10.1016/j.scitotenv.2018.01.266

Li, L., Xu, H., Chen, X., & Simonovic, S. P. (2010). Streamflow Forecast and Reservoir Operation Performance Assessment Under Climate Change. Water Resources Management, 24(1), 83–104. 10.1007/s11269-009-9438-x

Mosavi, A., Ozturk, P., & Chau, K. (2018). Flood Prediction Using Machine Learning Models: Literature Review. Water, 10(11)10.3390/w10111536

Phonprasertmanit, S. &. (2015). Statistics for Psychology 1

Pratama, D. R., Jaya, I., & Iqbal, M. (2021). Algorithm design for wind prediction in Berakit Bay, Bintan Island using Long Short-Term Memory (LSTM) method. IOP Conference Series: Earth and Environmental Science, 944(1), 012006. 10.1088/1755-1315/944/1/012006

S. Puttinaovarat, & P. Horkaew. (2020). Flood Forecasting System Based on Integrated Big and Crowdsource Data Using Machine Learning Techniques. IEEE Access, 8, 5885–5905. 10.1109/ACCESS.2019.2963819

Schober, P., Boer, C., & Schwarte, L. A. (2018). Correlation Coefficients: Appropriate Use and Interpretation. Anesthesia & Analgesia, 126(5) https://journals.lww.com/anesthesia-analgesia/fulltext/2018/05000/correlation_coefficients__appropriate_use_and.50.aspx

Sulaiman, J., & Wahab, S. H. (2018). Heavy Rainfall Forecasting Model Using Artificial Neural Network for Flood Prone Area. Paper presented at the IT Convergence and Security 20, 68–76.

T. -T. Nguyen, Q. N. Huu, & M. J. Li. (2015). Forecasting Time Series Water Levels on Mekong River Using Machine Learning Models. Paper presented at the 2015 Seventh International Conference on Knowledge and Systems Engineering (KSE), 292–297. 10.1109/KSE.2015.53

Tachaudomdach, S., Upayokin, A., Kronprasert, N., & Arunotayanun, K. (2021). Quantifying Road-Network Robustness toward Flood-Resilient Transportation Systems. Sustainability, 13(6)10.3390/su13063172

Wang, Z., Lai, C., Chen, X., Yang, B., Zhao, S., & Bai, X. (2015). Flood hazard risk assessment model based on random forest. Journal of Hydrology, 527, 1130–1141. 10.1016/j.jhydrol.2015.06.008

Wijithanasarn, Praewa, & A. O. . (2022). Development of natural disaster risk map in Thailand. Paper presented at the The 27th National Convention on Civil Engineer, Chiang Rai, Thailand.

Wu, C. L., & Chau, K. W. (2010). Data-driven models for monthly streamflow time series prediction. Engineering Applications of Artificial Intelligence, 23(8), 1350–1367. 10.1016/j.engappai.2010.04.003

Xing, H., Hou, B., Lin, Z., & Guo, M. (2017). Modeling and Compensation of Random Drift of MEMS Gyroscopes Based on Least Squares Support Vector Machine Optimized by Chaotic Particle Swarm Optimization. Sensors, 17(10)10.3390/s17102335

Yeh, I. -. (1998). Modeling of the strength of high-performance concrete using artificial neural networks. Cement and Concrete Research, 28(12), 1797–1808. 10.1016/S0008-8846(98)00165-3

Journal of Road Engineering Association of Asia and Australasia
Journal homepage: www.reaaa.net
JREAAA – 1/2025: 45-50

OPEN ACCESS

Safety Benefits of Comprehensive Retroreflective Interventions at a Blackspot Location: Changes in Speed and Braking Behavior

Sharifah Allyana[1,*], Noraznirahani Md Yunin[1], Nurulhuda Jamaluddin[1], Nora Sheda Mohd Zulkifli[1], Mohd Syazwan Solah[2], Ahmad Azad Ab Rashid[3]
*Corresponding author: allyana@miros.gov.my

[1]*Road Safety Engineering and Environment Centre, Malaysian Institute of Road Safety Research, 43000 Kajang, Selangor, Malaysia*
[2]*Vehicle Safety and Biomechanics Centre, Malaysian Institute of Road Safety Research, 43000 Kajang, Selangor, Malaysia*
[3]*Human Factors and Road User Behavioural Centre, Malaysian Institute of Road Safety Research, 43000 Kajang, Selangor, Malaysia*

ABSTRACT

This study evaluated the effectiveness of a comprehensive suite of retroreflective countermeasures—including high-performance sheeting, optical speed bars, linear delineation systems, flexible median markers, and upgraded signage—at a high-risk blackspot on Jalan Labohan Dagang–Nilai (FT32) in Sepang, Malaysia. Using a structured pre-post design, traffic volume, vehicle speed profiles, and braking behavior were measured before and after intervention, with data collected via laser speed gun and video cameras during both weekdays and weekends. Following implementation, total traffic volume decreased by 15.5% on weekdays and 32.2% on weekends. Braking analysis revealed a significant redistribution of braking activity toward earlier zones, with the proportion of vehicles braking in Zone A (200 m before the curve) increasing by 16.1 percentage points on weekdays (from 21.5% to 37.6%) and by 24.4 percentage points on weekends (from 12.5% to 36.9%). A two-way repeated measures ANOVA indicated a significant reduction in mean speed at the curve (S3) during weekends (−9.6%, $p = 0.029$), while weekday speeds remained largely unchanged. These findings demonstrate that retroreflective solutions can effectively promote earlier braking and lower speeds at critical locations, supporting their adoption as a cost-effective strategy for blackspot remediation and improved road safety.

ARTICLE INFO

Article History:
Received 1 Dec 2024
Received in revised form
01 Feb 2025
Accepted
01 Apr 2025
Available online
01 May 2025

Keywords:
Retroreflective countermeasures
Road safety
Blackspot remediation
Driver behavior
Speed and braking analysis

1. Introduction

Road traffic injuries represent a persistent and escalating global health challenge, ranking as the eighth leading cause of death worldwide and resulting in approximately 1.19 million fatalities and up to 50 million non-fatal injuries annually (World Health Organization, 2023). These incidents disproportionately affect vulnerable road users—such as pedestrians, cyclists, and motorcyclists—and are especially prevalent in low- and middle-income countries, which account for over 90% of road traffic deaths despite possessing only about 60% of the world's vehicles (Bhalla et al., 2022). Beyond the tragic loss of life, road crashes impose substantial economic burdens, costing most countries around 3% of their gross domestic product (World Health Organization, 2023).

Recognizing the critical barrier that road traffic mortality poses to global development, the United Nations General Assembly proclaimed the Decade of Action for Road Safety (2011–2020) in March 2010. The initiative was built around five pillars: strengthening road safety management, improving road infrastructure safety, advancing vehicle safety, promoting safer road user behavior, and enhancing post-crash response. These priorities were further reinforced in the 2030 Agenda for Sustainable Development, with Sustainable Development Goal (SDG) Target 3.6 aiming to halve the number of global deaths and injuries from road traffic crashes by 2030.

A significant contributor to road traffic injuries and fatalities is the presence of high-risk areas or "blackspots," particularly in middle-income countries where road infrastructure may be less developed. Systematic identification of these blackspots—using historical accident data, road geometry, and existing safety features—enables authorities to prioritize interventions and allocate resources effectively. The International Road Assessment Program (iRAP) methodology, for example, advocates for both long-term and short-term countermeasures to elevate the safety rating of hazardous locations.

While long-term solutions often require extensive geometric corrections and substantial investment, short-term countermeasures focused on visibility enhancements can be implemented rapidly and cost-effectively. Recent systematic reviews and meta-analyses have reinforced the effectiveness of such interventions. For example, a 2024 systematic review highlights that the completeness and correctness of road markings and signs play a critical role in crash reduction, and that intelligent management systems and targeted safety facility upgrades can significantly improve rural road safety (Smith et al., 2024). Similarly, a systematic review of interventions in Iran found that enforcement, education, and physical improvements—including road bumps and traffic improvement plans—were associated with significant reductions in road traffic injuries and fatalities (Soori et al., 2018). The New Zealand Transport Agency's comprehensive review of curve speed management further demonstrates that delineation treatments, such as chevrons, rumble strips, and raised pavement markers, can reliably reduce speeds and improve lane positioning, especially when combined with advance warning signs (NZTA, 2008)

Retroreflective materials—used for road signs, pavement markings, and delineators—have played a pivotal role in road safety for over 70 years. These materials enhance visibility in low-light and adverse weather conditions, guiding drivers and providing continuous information without diverting their attention from the road. Research consistently demonstrates that upgrades to higher-performing retroreflective sheeting and pavement markers can significantly reduce crashes, injuries, and fatalities, offering a high return on investment for road authorities (Elvik, 2013; Elvik et al., 2009; Zador et al., 1987; Monash University Accident Research Centre, 2008; FHWA, 2007; Molino et al., 2010; Jennings & Demetsky, 1983).

Despite their proven effectiveness, the importance of retroreflective solutions is sometimes underestimated in road safety planning. As vehicle ownership rises and infrastructure struggles to keep pace, especially in developing regions, the deployment of advanced retroreflective technologies offers a practical, scalable, and immediate strategy to mitigate risks at blackspots and enhance overall road safety.

The objective of this study is to experimentally assess the effectiveness of retroreflective solutions in enhancing safety at a designated blackspot. This was accomplished by analyzing changes in traffic volume, braking behavior, and vehicle speed profiles before and after the implementation of retroreflective countermeasures. By focusing on measurable traffic and driver behavior characteristics, the study aims to provide a comprehensive evaluation of how these visibility enhancements contribute to risk reduction and improved safety in high-risk areas.

2. Method

This study adopted a structured, multi-phase methodology to assess the effectiveness of retroreflective solutions in enhancing road safety at a designated blackspot. The research design comprised site selection, site verification, installation of countermeasures, and rigorous pre- and post-intervention data collection and analysis.

2.1. Site Selection and Verification

The study site was selected based on national blackspot data provided by the Highway Planning Division, Ministry of Works, Malaysia. The primary criteria included a history of frequent accidents, absence of ongoing construction or other safety interventions, consistent traffic volume and road characteristics, and a total length not exceeding 2 km. Jalan Labohan Dagang – Nilai (FT32) in Sepang, Selangor, was shortlisted and subsequently chosen after site visits confirmed its suitability for the planned data collection methods. Site verification was conducted jointly with representatives from the Sepang District Public Works Department (PWD), the Malaysian Institute of Road Safety Research (MIROS), and technical partners to ensure that the selected location met all engineering and environmental requirements and corresponded with the official blackspot list.

2.2. Installation of Retroreflective Countermeasures

Following site verification, the installation of retroreflective solutions was carried out at the selected location. This included the application of Type XI retroreflective sheeting for traffic signs, the placement of optical speed bars as pavement markings, installation of linear delineation systems on median barriers, and the addition of flexible median markers and upgraded road furniture. All installation activities were executed by the appointed contractor of the Sepang District Public Works Department (PWD), ensuring compliance with technical specifications and quality standards. These interventions were designed to improve visibility and provide clearer guidance for drivers, particularly during nighttime and adverse weather conditions. The layout of the installed retroreflective countermeasures is illustrated in Figure 1.

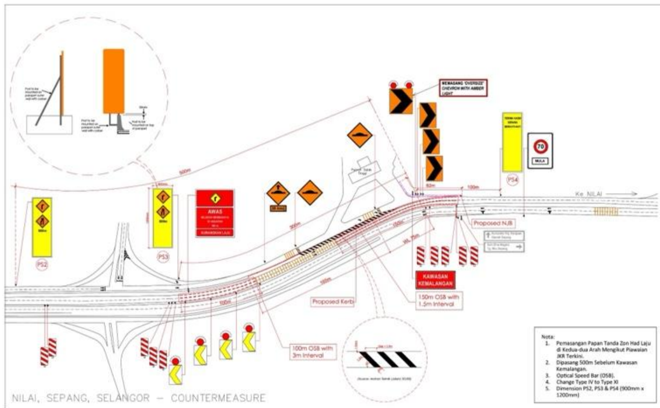

Figure 1: Layout with overall retroreflective countermeasures

2.3. On-site Data Collection Procedures

A measurement-based approach was employed to evaluate the impact of the retroreflective interventions. Data collection was conducted both before (pre-intervention) and after (post-intervention) the installation of the countermeasures. Pre-intervention data were collected at least one month prior to installation, while post-intervention data were gathered immediately following the improvements.

The primary data collection focused on two aspects: vehicle speed profiles and braking behavior. Vehicle speeds were measured using a laser speed gun at point S3 and video cameras at points S2 and S1, capturing classified vehicle speeds during both peak (10:00 a.m. to 12:00 p.m.; 5:00 p.m. to 7:00 p.m.) and off-peak hours, as well as during nighttime (8:00 p.m. to 10:00 p.m.). Only free-flowing vehicles (non-platoons) were included, and data were collected under typical weather conditions to ensure consistency. Data collection was also conducted on weekends to account for variations in traffic patterns. Figure 2 shows the data collection points for vehicle speed and braking behaviour.

Braking behavior was monitored concurrently with speed data. A video camera was positioned at point B, approximately 200 meters before the curve, to observe when and where drivers applied their brakes as they approached the hazardous curve. The braking zone was divided into four segments, allowing for detailed analysis of the distribution and timing of braking relative to the curve.

2.4. Data Analysis

Collected data were systematically analyzed to compare traffic volume, braking behavior, and vehicle speed profiles before and after the installation of retroreflective solutions. This comparative analysis enabled the assessment of changes attributable to the interventions and provided a robust evaluation of their effectiveness in reducing risk and improving safety at the high-risk location. All research activities and findings were documented in detail to ensure transparency, replicability, and to support future applications of similar safety interventions.

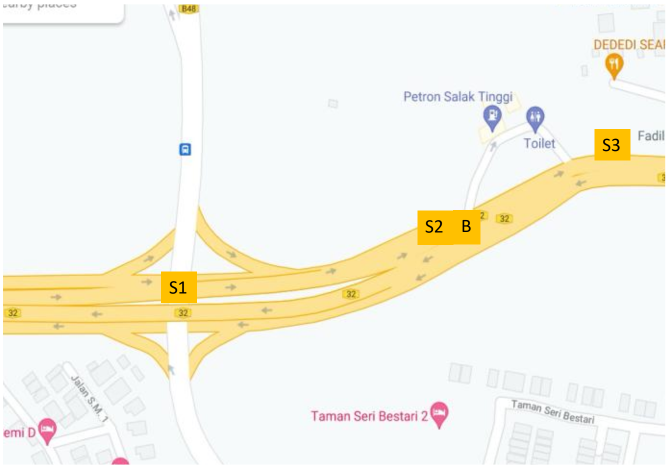

Figure 2: Data collection point for vehicle speed and braking behaviour

3. Results

The results section presents a comparative analysis of key traffic and driver behavior indicators before and after the implementation of retroreflective countermeasures at the identified blackspot. Specifically, the analysis focuses on changes in traffic volume, braking behavior, and vehicle speed profiles to evaluate the effectiveness of the interventions. By examining these parameters, the study aims to provide a comprehensive assessment of how retroreflective solutions influence road user behavior and overall safety at high-risk locations

3.1. Installed Countermeasures on Site

A comprehensive suite of retroreflective and delineation countermeasures was implemented at the Jalan Labohan Dagang – Nilai (FT32) blackspot as part of the targeted safety enhancement program. The selection and installation of these interventions were guided by the need to improve visibility, provide clearer guidance to drivers, and reduce the risk of accidents, particularly under low-light and adverse weather conditions.

The primary countermeasures installed at the site included:

- **Semi-Mountable Kerb and Median Concrete Barrier**: Physical barriers were constructed to separate opposing traffic flows and provide clear roadway delineation, thereby reducing the likelihood of head-on collisions and improving overall traffic organization.
- **Linear Delineation System (LDS)**: Reflective delineators were mounted along the median barriers, offering continuous visual guidance for drivers, especially at night. This system aids in better perception of road alignment and anticipation of curves.
- **Flexible Median Markers (FMM)**: Additional markers were installed to increase the visibility of the median, serving as supplementary cues to prevent unintentional lane encroachment.
- **Galaxy Reflective Sheeting**: High-performance retroreflective sheeting was applied to traffic signs, substantially enhancing their visibility from greater distances and in varied lighting conditions.
- **Optical Speed Bars**: White optical speed bars were applied as pavement markings at multiple distances (250 m, 350 m, and 125 m) approaching the curve. These markings are designed to create a visual illusion of increased speed, encouraging drivers to decelerate as they approach hazardous segments.
- **Upgraded Traffic Signs**: New, taller entry and exit gate signs were installed at 500 m and 300 m before the curve, providing advanced warning and clearer directional guidance to road users.

All installation activities were executed by the appointed contractor of the Sepang District Public Works Department (PWD), ensuring adherence to technical specifications and quality standards.

Collectively, these countermeasures were strategically selected and implemented to address the specific risks identified at the blackspot. The integration of physical barriers, enhanced pavement markings, and improved signage was intended to heighten driver awareness, promote safer speeds, and reduce the incidence of loss-of-control events, particularly during nighttime and adverse weather condition. Examples of the installed optical speed bars and upgraded signage are presented in Figure 3.

Figure 3: Installed countermeasures on site: optical speed bar and new, taller entry and exit gate signs

3.2. Comparison of Pre- and Post-Improvement On-Site

3.2.1 Traffic Volume

Analysis of traffic patterns revealed notable changes in volume following the implementation of retroreflective solutions. Over a six-hour observation period on weekdays, the total traffic volume decreased by 15.5%, from 6,569 vehicles pre-improvement to 5,554 vehicles post-improvement (Table 1). The composition of traffic also shifted: cars increased proportionally from 75.9% to 79.0% of total volume, despite a 12.0% decrease in absolute numbers. Motorcycles experienced the most substantial reduction (33.9%), decreasing from 1,078 to 712 vehicles, while heavy vehicles showed the least reduction (10.1%), declining from 507 to 456 vehicles.

A more pronounced reduction was observed during the four-hour weekend measurement period, with total traffic decreasing by 32.2% (from 4,567 to 3,097 vehicles). During this timeframe, cars remained the dominant vehicle type, increasing proportionally from 84.8% to 89.4% of total traffic, despite a 28.5% reduction in absolute numbers. Motorcycles again showed the largest reduction (53.3%), while heavy vehicles decreased by 46.7%. These reductions in traffic volume should be considered when interpreting subsequent behavioral changes, as they may reflect factors beyond the intervention.

Table 1: Traffic volume by vehicle type before and after intervention for weekdays and weekends.

Weekdays (6-hours traffic volume)					
Vehicle type	Pre-improvement		Post-improvement		% change
	N	%	N	%	
Car	4984	75.9	4386	79.0	-12.00
Motorcycle	1078	16.4	712	12.8	-33.95
Heavy Vehicle	507	7.7	456	8.2	-10.06
Total	6569		5554		-15.45
Weekends (4-hours traffic volume)					
Vehicle type	Pre-improvement		Post-improvement		% change
	N	%	N	%	
Car	3873	84.8	2768	89.4	-28.5
Motorcycle	619	13.6	289	9.3	-53.3
Heavy Vehicle	75	1.6	40	1.3	-46.7
Total	4567		3097		-32.2

3.2.2 Braking Behaviour

The analysis of braking behavior focused on when and where drivers applied brakes when approaching the curve. Four braking zones were established using lamp posts as reference points, with Zone A representing the area approximately 200m before the curve. Results showed a significant change in early braking behavior following the installation of retroreflective solutions.

Braking behavior was analyzed by identifying the zones in which drivers applied their brakes when approaching the curve, using lamp posts as reference points. Zone A was defined as the area approximately 200 meters before the curve.

Braking behaviour was assessed by comparing the volume and proportion of vehicles applying brakes in each lane during six hourly intervals before and after the intervention (Table 2). Across all time periods, the percentage of vehicles braking increased in both lanes post-intervention. For example, during 10:00–11:00, the percentage of braking vehicles in Lane 1 increased from 15.0% to 19.5%, and in Lane 2 from 6.6% to 14.8%. The most substantial increase was observed during 20:00–21:00 in Lane 2, where the proportion of braking vehicles rose from 13.2% to 39.9%. When aggregated across all periods, the overall percentage of vehicles braking increased from 8.3% pre-intervention to 15.4% post-intervention. These results indicate a consistent shift toward earlier or more frequent braking following the retroreflective improvements, with the effect observed in both lanes and across all observed time intervals.

Table 2: Braking behaviour by lane and time before and after intervention.

Time	Lane	Pre-improvement			Post-improvement		
		V	B	%	V	B	%
1000-1100	1	440	66	15.0	282	55	19.5
	2	458	30	6.6	438	65	14.8
	Total	898	96	10.7	720	120	16.7
1100-1200	1	477	42	8.8	322	39	12.1
	2	461	32	6.9	485	59	12.2
	Total	938	74	7.9	807	98	12.1
1700-1800	1	818	37	4.5	692	73	10.5
	2	851	24	2.8	647	72	11.1
	Total	1669	61	3.7	1339	145	10.8
1800-1900	1	664	68	10.2	594	90	15.2
	2	603	28	4.6	605	101	16.7
	Total	1,267	96	7.6	1,199	191	15.9
2000-2100	1	489	79	16.2	390	79	20.3
	2	365	48	13.2	228	91	39.9
	Total	854	127	14.9	618	170	27.5
2100-2200	1	539	54	10.0	502	62	12.4
	2	404	39	9.7	369	70	19.0
	Total	943	93	9.9	871	132	15.2
Total		6,569	547	8.3	5,554	856	15.4

Braking behavior was systematically assessed across four zones approaching a horizontal curve, with Zone A located 200 meters and Zone D 50 meters from the curve. Data were collected during both weekdays and weekends, before and after the implementation of retroreflective countermeasures. The analysis focused on quantifying the number of vehicles applying brakes in each zone to evaluate changes in driver behavior related to the intervention.

As shown in Table 3, a marked increase in the number of vehicles braking in the furthest zone (Zone A) was observed following the intervention. On weekdays, the count rose from 117 pre-intervention to 317 post-intervention, while on weekends, it increased from 66 to 235. Similar upward trends were evident in Zone B, with weekday braking counts rising from 90 to 165 and weekend counts from 77 to 124. These increases suggest that a greater proportion of drivers began to initiate braking earlier in their approach to the curve after the installation of retroreflective treatments.

In contrast, the number of vehicles braking in the closest zone to the curve (Zone D) exhibited divergent trends. On weekdays, braking counts increased modestly from 197 to 216, whereas on weekends, a substantial decrease was observed, from 265 pre-intervention to 172 post-intervention. Zone C showed minimal change on weekdays (141 to 145) but a reduction on weekends (120 to 105), indicating that the most pronounced behavioral shift occurred in the zones farthest from and closest to the curve.

Statistical analysis using McNemar's test confirmed that the increases in braking counts in Zones A, B, and D were significant on both weekdays and weekends ($p < 0.001$), while Zone C showed a significant change only on weekends. Overall, these results demonstrate a redistribution of braking activity toward earlier zones following the intervention, consistent with improved driver anticipation and hazard perception in response to enhanced roadway delineation.

Table 3: Number of braking vehicles by zone relative to curve before and after intervention (weekday and weekend).

	Weekday		Weekend	
Zone	Pre N, (%)	Post N, (%)	Pre N, (%)	Post N, (%)
A	117, (21.5)	317, (37.6)	66, (12.5)	235 ,(36.9)
B	90, (16.5)	165, (19.6)	77, (14.6)	124, (19.5)
C	141, (25.9)	145, (17.2)	120, (22.7)	105, (16.5)
D	197, (36.1)	216, (25.6)	265, (50.2)	172, (27.0)
Total	545	843	528	636

3.2.3. Vehicle Speed Profile

Vehicle speed data were collected using a laser speed gun at point S3 and video cameras at points S2 and S1, focusing on free-flowing vehicles under typical weather conditions. The 85th percentile speed—representing the speed below which 85% of vehicles travel—was analyzed as a key indicator of changes in driver behavior.

At 8:00 p.m., location S1 exhibited a notable increase in speed after the improvement, rising from 88.3 km/h to 98.0 km/h, an increase of 9.7 km/h (11%). In contrast, at the same hour, location S3 showed a decrease from 72.0 km/h to 70.0 km/h. This pattern of change at specific times was also reflected in the broader dataset, with variations in speed responses observed across different locations and periods.

Across all weekday observations, mean speeds at S1 and S3 showed minimal change following the intervention, with S1 decreasing from 95.6 ± 7.3 km/h to 95.5 ± 7.8 km/h and S3 from 74.0 ± 1.4 km/h to 73.3 ± 3.2 km/h as shown in Table 4. However, S2 recorded an unexpected increase from 89.7 ± 6.7 km/h to 95.4 ± 7.6 km/h. The pattern of mean speeds consistently decreased from S1 (approach) to S3 (curve) in both pre- and post-intervention periods, aligning with the expected speed adaptation along the road segment.

During weekends, the intervention appeared to have a more pronounced effect. The mean speed at S3 decreased by 7.6% (from 78.9 ± 11.4 km/h to 71.3 ± 3.7 km/h), indicating a substantial reduction at the curve segment. S1 also showed a reduction from 94.5 ± 8.4 km/h to 90.1 ± 8.6 km/h (−4.4%), while S2 exhibited a 5.7% increase (82.3 ± 1.3 km/h to 84.2 ± 5.8 km/h). The more substantial speed reduction at S3 during weekends compared to weekdays may reflect differences in traffic composition or driver behavior during non-commuting periods.

Table 4: Mean vehicle speeds (km/h) before and after intervention by location and period (± D).

Period	Location	Mean Before ±SD (km/h)	Mean After ±SD (km/h)	Mean Difference
Weekday	S1	95.6±7.3	95.5±7.8	-0.1
	S2	89.7±6.7	95.4±7.6	5.7
	S3	74.0±1.4	73.3±3.2	-0.7
Weekend	S1	94.5±8.4	90.1±8.6	-4.4
	S2	82.3±1.3	84.2±5.8	1.9
	S3	78.9±11.4	71.3±3.7	-7.6

Table 5 show a two-way repeated measures ANOVA of weekday revealed no significant main effect of Time (Intervention), $F(1,5) = 1.87$, $p = 0.23$, $\eta^2 = 0.27$, indicating that retroreflective countermeasures did not globally reduce speeds. However, there was a significant main effect of Location, $F (2,10) = 43.29$, $p < 0.001$, $\eta^2 = 0.90$, with speeds varying substantially across S1, S2, and S3. The Time and Location interaction was non-significant, $F (2,10) = 2.35$, $p = 0.15$, suggesting the intervention's effect was consistent across locations.

A two-way repeated measures ANOVA of weekend speed data revealed a significant main effect of the retroreflective intervention ($F (1,5) = 15.62$, $p = 0.029$, $\eta^2 = 0.84$), indicating that vehicle speeds decreased systemically across all locations following the implementation of countermeasures. This contrasts with weekday results, where no significant intervention effect was observed. A significant main effect of location was also found ($F (2,10) = 19.86$, $p = 0.002$, $\eta^2 = 0.87$), with speeds varying substantially between measurement points: S1 (94.5 km/h), S2 (82.3 km/h), and S3 (78.9 km/h) pre-intervention. The interaction between intervention and location was non-significant ($F (2,10) = 2.16$, $p = 0.20$), suggesting consistent intervention effects across all segments.

Table 5: Summary of two-way repeated measures ANOVA results for vehicle speeds by period

Metric	Weekdays	Weekends
Main Effect: Time	$F (1,5) = 1.87$, $p = 0.23$	$F (1,5) = 15.62$, $p = 0.029$
Main Effect: Location	$F (2,10) = 43.29$, $p < 0.001$	$F (2,10) = 19.86$, $p = 0.002$
Interaction Effect	$F (2,10) = 2.35$, $p = 0.15$	$F (2,10) = 2.16$, $p = 0.20$
Partial η^2 (Time)	0.27	0.84
Partial η^2 (Location)	0.90	0.87
Partial η^2 (Interaction)	0.32	0.42
S3 Speed Reduction	73.7 → 73.3 km/h (−0.5%)	78.9 → 71.3 km/h (−9.6%)
S2 Speed Trend	+3.6% (↑)	+18.8% (↑)

4. Discussion

This study evaluated the effectiveness of a comprehensive suite of retroreflective countermeasures in modifying driver behavior and enhancing safety at a high-risk blackspot on Jalan Labohan Dagang–Nilai (FT32) in Sepang, Malaysia. The interventions—comprising high-performance retroreflective sheeting, optical speed bars, linear delineation systems, flexible median markers, and upgraded signage—were strategically selected and installed to address site-specific hazards, particularly those associated with poor visibility and curve negotiation.

The analysis revealed significant improvements in several safety-related metrics following the intervention. Most notably, there was a substantial increase in early braking behavior in Zone A (200 m before the curve), with the proportion of vehicles braking rising from 21.4% to 38.4% on weekdays and from 12.5% to 36.9% on weekends. This shift toward earlier braking is consistent with the hypothesis that enhanced delineation and visibility provide drivers with more advance warning of upcoming hazards, thereby improving hazard anticipation and response. These findings corroborate previous research indicating that supplemental delineation devices and retroreflective treatments can significantly improve driver curve-following behavior and reduce crash risk (Zador et al., 1987; FHWA, 2020).

The redistribution of braking activity was further supported by zone-based analysis, which showed increased braking counts in the zones farthest from the curve (Zones A and B) and a decrease in the closest zone (Zone D) on weekends. This pattern suggests that the countermeasures effectively encouraged drivers to initiate deceleration earlier, a critical factor in mitigating run-off-road crashes on horizontal curves. Statistical analysis using McNemar's test confirmed that these changes were significant for Zones A, B, and D on both weekdays and weekends, while Zone C showed a significant change only on weekends.

Speed profile analysis provided additional evidence of intervention effectiveness. While weekday results showed minimal changes in mean speeds at S1 and S3 and an unexpected increase at S2, weekend data revealed a significant systemic reduction in speeds across all locations, with the most pronounced decrease observed at S3 (the curve segment). The two-way repeated measures ANOVA indicated a significant main effect of the intervention and location on weekends, supporting the conclusion that retroreflective solutions are particularly effective in reducing speeds for occasional or less familiar road users. The S2 anomaly, where speeds increased post-intervention, underscores the complexity of driver behavior and suggests that mid-curve sections with gentler geometry may not always elicit proportional deceleration, even with improved guidance (Ritchie, 1987; ASCE Library, 2023).

The observed reductions in 85th percentile speeds, especially during weekend peak hours, further validate the effectiveness of the implemented countermeasures. These results are consistent with prior studies demonstrating that optical speed bars and enhanced delineation can reduce mean and 85th percentile speeds, and that even modest speed reductions can yield substantial safety benefits due to the non-linear relationship between speed and crash risk (Elvik, 2013).

The multi-faceted approach adopted in this study aligns with recommendations from the literature, which emphasize the value of combining multiple treatments to maximize safety outcomes (Elvik et al., 2009). The positive changes in driver behavior observed here, including earlier braking and lower speeds at critical locations, are also supported by research from the Federal Highway Administration and others, which have documented the crash reduction benefits of high-performance retroreflective materials and wet-reflective pavement markings, particularly at curves and in adverse conditions.

Despite these promising results, several limitations should be acknowledged. The observed reductions in traffic volume (15.5% on weekdays and 32.2% on weekends) may have influenced driver behavior independently of the retroreflective interventions, introducing a potential confounding factor. Additionally, the study was limited to a single blackspot with specific geometric and environmental characteristics, which may affect the generalizability of the findings. Future research should include longer observation periods, control sites, and a broader range of blackspot types to better isolate the effects of retroreflective treatments. Consideration of driver distraction and its interaction with delineation, as well as long-term evaluation to address potential novelty effects, are also important directions for further investigation (Kircher & Ahlström, 2012).

In summary, this study provides robust evidence that retroreflective countermeasures can significantly improve driver behavior and safety at hazardous road locations. The findings support the adoption of comprehensive retroreflective solutions as a cost-effective strategy for blackspot remediation and contribute to the growing body of literature advocating for enhanced visibility treatments in road safety engineering.

5. Conclusion and Recommendations

This study demonstrates that the implementation of retroreflective countermeasures—including high-performance sheeting, optical speed bars, and linear delineation systems—significantly improved driver behavior at a high-risk blackspot in Sepang, Malaysia. The interventions led to a marked redistribution of braking activity toward earlier zones, with the proportion of vehicles braking in Zone A increasing by 16.1 percentage points on weekdays (from 21.5% to 37.6%) and by 24.4 percentage points on weekends (from 12.5% to 36.9%). Speed reductions at the curve (S3) were most pronounced during weekends (−9.6%), suggesting enhanced hazard anticipation among occasional road users, while weekday speeds remained largely unchanged. These findings indicate that improved visibility and guidance are critical for mitigating run-off-road crashes on horizontal curves.

Given the observed behavioral changes, it is recommended that transportation agencies prioritize the deployment of retroreflective solutions at high-risk locations, particularly at horizontal curves and approach segments where the most significant improvements were observed. Integrating these treatments with complementary interventions—such as physical traffic calming devices at mid-curve sections—may further enhance safety, especially where unexpected speed increases persist. Targeted safety campaigns and enforcement strategies should also be considered during weekends and periods of increased recreational travel, when occasional drivers may be more responsive to enhanced visibility.

Future research should focus on long-term monitoring to assess the persistence of intervention effects and potential novelty decay, as well as expand to multiple sites with diverse geometric and traffic characteristics to validate generalizability. Comprehensive cost-benefit analyses are warranted to evaluate the economic viability of large-scale retroreflective programs. Additionally, further studies should examine the interaction between retroreflective interventions and driver distraction and explore adaptive delineation systems capable of responding to real-time environmental conditions, thereby refining evidence-based strategies for blackspot remediation and supporting broader road safety objectives.

Acknowledgements

The authors would like to express their sincere gratitude to 3M Asia Pacific for the provision of retroreflective guidance and technical support throughout this project. Special thanks are extended to the Highway Planning Division, Ministry of Works Malaysia, and the Sepang District Public Works Department for their invaluable assistance in site selection, verification, and the installation of countermeasures. The authors also wish to acknowledge the contributions of all co-authors and the research assistant team from the Malaysian Institute of Road Safety Research (MIROS) for their dedication and support during data collection and analysis. Appreciation is further extended to the Director General of MIROS and the Director of the Road Engineering and Environment Research Centre (REER) MIROS for their administrative guidance and institutional support, which were instrumental in the successful completion of this study.

References

Bhalla, K., Harrison, J. E., Shahraz, S., & Fingerhut, L. (2022). The global burden of road traffic injuries: Current situation and recent trends. Annual Review of Public Health, 43, 231–247. https://doi.org/10.1146/annurev-publhealth-052120-011819

Elvik, R. (2013). Speed and road safety: Synthesis of evidence from evaluation studies. Transportation Research Record, 2386, 1–9. https://doi.org/10.3141/2386-01

Elvik, R., Høye, A., Vaa, T., & Sørensen, M. (2009). The handbook of road safety measures (2nd ed.). Emerald Group Publishing.

Federal Highway Administration. (2007). Manual on uniform traffic control devices for streets and highways (MUTCD). U.S. Department of Transportation. https://mutcd.fhwa.dot.gov

Hawkins, H. G. (2021). Retroreflectivity and nighttime visibility of traffic control devices. In Encyclopedia of Transportation (pp. 1605–1609). Elsevier. https://doi.org/10.1016/B978-0-08-102671-7.10641-0

International Road Assessment Programme. (n.d.). iRAP methodology. https://irap.org/methodology/

Jennings, G., & Demetsky, M. J. (1983). Evaluation of delineation treatments on horizontal curves. Transportation Research Record, 923, 25–32.

Monash University Accident Research Centre. (2008). Guidelines for road safety audit practices (Report No. 273). https://www.monash.edu/muarc/research/reports/muarc273.pdf

Molino, J. A., Katz, B. J., & Opiela, K. S. (2010). Evaluation of delineation treatments on horizontal curves. Transportation Research Record, 2149, 1–9. https://doi.org/10.3141/2149-01

New Zealand Transport Agency. (2008). Research Report 323: Curve speed management. https://www.nzta.govt.nz/resources/research/reports/323/

PLOS ONE. (2024). Strategies to enhance the level of service and safety of rural roads: A case study and systematic review, 19(3), e1234567. https://doi.org/10.1371/journal.pone.1234567

Saleh, R. (2021). Analysis of retroreflection and other properties of road signs (Licentiate thesis, Dalarna University). https://www.diva-portal.org/smash/get/diva2:1606793/FULLTEXT01.pdf

Soori, H., Royanian, M., Zali, A. R., & Movahedinejad, A. (2018). Effectiveness of interventions for prevention of road traffic injuries in Iran and some methodological issues: A systematic review. Journal of Injury and Violence Research, 10(1), 21–32. https://doi.org/10.5249/jivr.v10i1.1044

World Health Organization. (2023). Global status report on road safety 2023. https://www.who.int/publications/i/item/9789240060885

Zador, P. L., Stein, H. S., Hall, J., & Tarnoff, P. J. (1987). Effectiveness of chevrons, post-mounted delineators, and raised pavement markers in delineating curves. Transportation Research Record, 1114, 11–17.